The Mass-Concentration relation of galaxy clusters as a cosmological probe

Tesi di Laurea Magistrale

Presentata da:
Andrea Silvi

Relatore:
Chiar.mo Prof.
Massimo Meneghetti

Co-relatori:
Dott. Stefano Ettori
Dott. Mauro Sereno

Sessione III
Anno Accademico 2015-2016

Sommario

Il modello cosmologico standard attualmente in vigore è il modello di universo piatto ΛCDM. Questo modello prevede il $\simeq 70\%$ in energia oscura, il $\simeq 25\%$ in materia oscura e il $\simeq 5\%$ in materia barionica. Per studiare osservativamente questo modello cosmologico e comprendere la formazione e l'evoluzione delle strutture cosmiche esistono diversi metodi, e.g., lo studio della radiazione di fondo cosmico, le galassie e gli ammassi di galassie che agiscono come lenti gravitazionali, il *clustering* di galassie, le oscillazioni acustiche barioniche e gli ammassi di galassie. Questi ultimi hanno un ruolo molto importante perché sono le più grandi strutture gravitazionalmente legate approssimativamente in equilibrio viriale, sono le ultime che si sono formate nella storia dell'universo e sono rappresentative della distribuzione di materia oscura e barionica su grande scala.

Gli ammassi di galassie sono stati studiati sia attraverso le osservazioni dirette, che attraverso le simulazioni numeriche N-body. Da esse è emerso che esiste un profilo di densità universale che descrive la distribuzione degli aloni di materia oscura. Questo profilo è chiamato NFW (Navarro, Frenk & White [1997]) ed è caratterizzato da due parametri: il *raggio di scala* e la *concentrazione*. Il raggio di scala r_s è definito come il raggio in cui la derivata del profilo di densità è uguale a -2, mentre la concentrazione c è definita come il rapporto tra il raggio entro il quale la densità dell'ammasso è $\Delta = 200$-volte la densità critica dell'universo, r_Δ, e r_s. La concentrazione di un alone di materia oscura è cosmologicamente molto importante perché essa è legata alla densità media dell'universo al tempo di formazione dell'alone stesso. Siccome la densità media dell'universo diminuisce con il tempo e siccome le strutture si formano in modo gerarchico, ci si aspetta che la concentrazione diminuisca sia all'aumentare della massa degli aloni sia all'aumentare del $redshift$. Per formazione gerarchica si intende che le strut-

ture più grandi nascono attraverso l'accrescimento e *merging* di strutture di massa minore, e quindi si sviluppano per ultime. Inoltre, il tempo di formazione di un alone, chiamato anche redshift di collasso z_{coll}, dipende dai parametri cosmologici Ω_M e σ_8. Il parametro Ω_M è definito come il rapporto tra la densità di materia e la densità critica, mentre il parametro σ_8 è definito come il valore quadratico medio delle fluttuazioni di massa in una sfera di raggio $8h^{-1}$Mpc. Il valore di z_{coll} risulta essere minore per modelli cosmologici con valori più bassi di Ω_M e di σ_8; di conseguenza, i valori della concentrazione c per gli aloni di materia oscura a massa fissata sono minori in questi modelli. Per questi motivi, la relazione c-M misurata negli ammassi di galassie dipende significativamente dalla cosmologia e, in particolare, dai parametri cosmologici Ω_M e σ_8.

Negli anni sono stati proposti diversi modelli semi-analitici per spiegare la dipendenza di c da M e z_{coll} (e.g., Navarro, Frenk & White [1997] e Giocoli et al. [2012]). Inoltre, sono stati proposti anche modelli empirici che cercano di riprodurre le simulazioni cosmologiche (e.g., Bullock et al. [2001] e Diemer & Kravtsov [2015]).

Per il lavoro di Tesi abbiamo studiato l'efficienza della relazione c-M degli ammassi di galassie nel determinare i parametri cosmologici Ω_M e σ_8. A tal scopo abbiamo sviluppato in Python un codice capace di simulare le concentrazioni attese negli ammassi di galassie a dato redshift e, per un'osservata distribuzione di concentrazioni, masse e redshift, determinare i valori di Ω_M e σ_8 che meglio la riproducono. Per fare cio' abbiamo considerato diversi modelli (Bullock et al. [2001], Prada et al. [2012], Bhattacharya et al. [2013] ed il Diemer & Kravtsov [2015]) che relazionano concentrazione e massa in aloni di materia oscura fredda, nella loro implementazione nel software pubblico `Colossus` (Diemer [2015]).

Il lavoro di Tesi si è suddiviso in tre parti. Nella prima parte del lavoro abbiamo testato l'efficienza del nostro codice. Abbiamo simulato diverse osservazioni assumendo un modello cosmologico e un modello della relazione c-M. Successivamente, abbiamo analizzato queste simulazioni, cercando le migliori combinazioni di Ω_M e σ_8 che riproducono i dati, con lo stesso modello della relazione c-M per verificare che i risultati finali fossero in accordo con i dati in input. Inoltre, abbiamo analizzato le simulazioni anche con gli altri modelli per analizzare le differenze sistematiche legate alla modelizzazione. I test hanno confermato il buon funzionamento del codice. Inoltre, abbiamo trovato un risultato già atteso, cioè che il modello di Prada et al. [2011] non riesce a riprodurre i dati in modo efficiente.

Nella seconda parte del lavoro abbiamo misurato i parametri cosmologici utilizzando il campione *Chandra* ad alto redshift, z, di Amodeo et al. [2016]. Utilizzando il modello di Bullock et al. [2001] abbiamo ottenuto $\Omega_M = 0.25^{+0.28}_{-0.15}$ e $\sigma_8 = 1.24^{+0.08}_{-0.42}$, con il modello di Bhattacharya et al. [2013] $\Omega_M = 0.14^{+0.14}_{-0.04}$ e $\sigma_8 = 1.16^{+0.34}_{-0.02}$, infine con il modello di Diemer & Kravtsov [2015] $\Omega_M = 0.10^{+0.30}_{-0.00}$ e

$\sigma_8 = 1.46^{+0.04}_{-0.59}$. Abbiamo verificato che l'accuratezza dei risultati è migliorata utilizzando il campione osservato con $XMM-Newton$ a basso z presentato in Ettori et al. [2010]. Inoltre, Abbiamo verificato come questi risultati siano in accordo con precedenti lavori che misuravano i due parametri cosmologici utilizzando altri metodi.

Nell'ultima parte del lavoro abbiamo indagato come cambia l'accuratezza e la precisione dei parametri cosmologici variando diverse quantità utilizzate per simulare le osservazioni. Queste quantità sono:

- il numero degli ammassi osservati;

- l'incertezza sulle misure di massa e c;

- lo scatter intrinseco della relazione c-M;

- il redshift.

Per tale motivo abbiamo generato diverse osservazioni variando questi parametri. Sia per generare le osservazioni sia per fittare i dati abbiamo utilizzato il modello di Diemer & Kravtsov [2015]. Abbiamo scelto questo modello perché basato sulle simulazioni numeriche più grandi rispetto agli altri modelli della relazione c-M. Abbiamo verificato come la precisione dei parametri cosmologici aumenti sistematicamente con il numero degli oggetti simulati e con il diminuire dell'incertezza delle misure e dello scatter intrinseco. L'accuratezza, invece, evolve molto più debolmente con il numero degli oggetti e ne diventa approssimativamente costante quando si considerano gli ammassi ad alto z. Utilizzando la migliore combinazione dei parametri che abbiamo studiato (numero ammassi osservati, le incertezze sulle misure, lo scatter intrinseco e il redshift) e considerando ammassi a $z = 0$, abbiamo notato che, con l'uso della relazione c-M, si può ottenere una precisione sui parametri cosmologici pari a 6.5% su Ω_M e 2.5% su σ_8 (assumendo che i due parametri abbiano stessa incertezza assoluta e considerando i parametri cosmologici ottenuti da Planck Collaboration [2016]). Infine, considerando gli ammassi a $z = 1$, abbiamo ottenuto una precisione pari a 31% su Ω_M e 12% su σ_8.

Contents

Introduction

The standard cosmological model is called the ΛCDM. This model predicts a universe originated by the *Big-Bang* and which is now growing up with an accelerated expansion. This model of universe is flat and composed of the dark energy, about $\simeq 70\%$ (Λ), Cold Dark Matter, about $\simeq 25\%$ (CDM), and baryonic matter, about $\simeq 5\%$. The structures are formed via gravitational collapse of small perturbations in a quasi-homogeneous universe, where these small perturbations were produced in the inflationary era. The small perturbations grow with time, against the cosmic expansion, until they surpass a threshold value. After this moment, the small perturbations collapse via self-gravity, forming the first small structures. The larger structures are formed through accretion and merger of the small structures. This process is called hierarchical clustering of the cosmic structures, or the *bottom-up* scenario. As a consequence, the clusters of galaxies are the last objects that are formed because they are the most massive objects in the universe. Therefore, they are a powerful tool to understand the formation and the evolution of the cosmic structures.

The galaxies contribute to the total mass of a galaxy cluster only for $\simeq 5\%$. The $\simeq 10\%$ is in hot temperature and low-density gas. The rest $\simeq 85\%$ is the dark matter. Numerical simulations N-body predict that the dark matter haloes have a universal density profile, called NFW profile (Navarro, Frenk & White [1997]). This profile is characterized by two parameters, the *scale radius* and the *concentration*. The scale radius r_s is defined as the radius at which the logarithmic slope of the density profile is equal to -2, while the concentration c is defined as the ratio between the radius at which the density of the cluster is $\Delta = 200$-times the critical density of the universe, r_Δ, and r_s.

The dark matter halo concentration is a cosmological tool because it is linked

to the universe mean density at the time the dark matter halo is formed, called collapse redshift z_{coll}. Therefore, it is expected that the concentration decreases with the cluster mass and the redshift. Moreover, z_{coll} depends on the cosmological model; z_{coll} is lower for cosmologies with lower values of the cosmological parameters Ω_M and σ_8, and, as consequence, c is lower at fixed mass. For these reasons, one can determinate the cosmological parameters Ω_M and σ_8 through the c-M relation.

In this Thesis, we investigate the efficiency of the c-M relation to constrain the cosmological parameters. The Thesis is organized as follows.

- *Chapter 1:* we give a brief review of the cosmological basics essentials to understand the several topics covered. We describe the theoretical basis of the formation and the evolution of the cosmic structures through the gravitational collapse of small perturbations.

- *Chapter 2:* we discuss the theoretical background of the c-M relation. We report some semi-analytic models that describe the connection of the concentration with the collapse redshift. Moreover, we describe the models that we have used in this work.

- *Chapter 3:* we describe our code and how it is built up. Moreover, we report a description of the Colossus tool that we have used to run the cosmological analysis. Finally, we report the several tests that we have performed to understand the efficiency of our code.

- *Chapter 4:* we report our results about the measure of the cosmological parameters, obtained with our code, using a high redshift *Chandra* data. We investigate the results improve using a low redshift $XMM - Newton$ data. Finally, we compare our results with previous works that measure the cosmological parameters with other methods.

- *Chapter 5:* we report our results about the accuracy and the precision to determinate the cosmological parameter using the c-M relation. We show how the accuracy and the precision change with several quantities by generating mock data. Finally, we determine the best observational strategy to determine cosmological parameters.

- *Chapter 6:* we summarize our main results and present our conclusions.

In the *Appendix* we present the most significant parts of the Python code used for this work.

1

Large Scale Structures and Cosmology

In this chapter, we introduce the main cosmological topics covered in this thesis. We present a brief review of the formation and evolution of the cosmic structures and the current favoured cosmological model.

1.1   Introduction

Cosmology is the study of the Universe in its entirety. Several cosmological models have been proposed. The most relevant cosmological models are based on the *Cosmological Principle*, which states that in the Universe neither position nor privileged direction exists; the Universe, on a wide scale, is homogeneous and isotropic. However, it can be supported by considerable independent observations, as the large-scale distribution of galaxies (and clusters of galaxies), or the *Cosmic Microwave Background* (hereafter CMB).

Another principle is the so-called *Perfect Cosmological Principle*, which states the immutability in the time of the homogeneous and isotropic Universe. The Perfect Cosmological Principle is the base of the Steady-State Universe, which was the main competitor of the *Hot Big-Bang* model until the CMB discovery, after which the Perfect Cosmological Principle was abandoned.

As far as Cosmology studies the Universe on the largest scale, gravity is the driving force to be considered. The most successful theory of gravity is the well known Einstein's General Relativity Theory. According to it, gravity is an effect of the space-time curvature determined by the matter (energy) distribution.

The *Einstein's field equations* read:

$$R_{\mu\nu} - \frac{1}{2}g_{\mu\nu}R = \frac{8\pi G}{c^4}T_{\mu\nu}, \tag{1.1}$$

where $R_{\mu\nu}$ is the Ricci curvature tensor, R is the Ricci scalar, $g_{\mu\nu}$ is the space-time metric and $T_{\mu\nu}$ is the relativistic energy-momentum tensor of the energy distribution, G is the universal gravitational costant and the c is the speed of light in vacuum. The $\mu\nu$-indicies are $\mu, \nu = 0, 1, 2, 3$ where 0 refers to the time-coordinate and $1, 2, 3$ to the space-coordinates. The Einstein's static cosmological model requires another term: the *Cosmological Costant* Λ. The field equations become:

$$R_{\mu\nu} - \frac{1}{2}g_{\mu\nu}R - \Lambda g_{\mu\nu} = \frac{8\pi G}{c^4}T_{\mu\nu}. \tag{1.2}$$

To find the solution of the field equations, we can make some assumptions on the metric and the energy-momentum tensor. Considering the isotropy of the Universe, one derives the *Friedmann-Robertson-Walker* metric (hereafter FRW):

$$ds^2 = c^2dt^2 - a^2(t)\left[\frac{dx^2}{1 - kx^2} + x^2(d\theta^2 + sin^2\theta d\varphi^2)\right], \tag{1.3}$$

where ds^2 is the infinitesimal interval between two events in the space-time, dt is the coordinate time interval between these events, dx is the adimensional spatial radial interval and $d\theta^2 + sin^2\theta d\varphi^2$ is the angular interval, $a(t)$ is the *expansion parameter* and k in the *curvature parameter*. The expansion parameter $a(t)$, or *scale factor*, has the dimension of length and acts as a factor for the spatial component of the FRW metric, giving the expansion of the Universe. The curvature parameter k is a constant and it can take the values $k = -1, 0, 1$ for an open, flat or closed geometry, respectively.

For the energy-momentum tensor, the perfect fluid behavior is assumed, and thus it reads:

$$T_{\mu\nu} = (p + \rho c^2)u_\mu u_\nu - pg_{\mu\nu}, \tag{1.4}$$

where p is the pressure, ρc^2 is the energy density and u_μ is the fluid four-velocity.

With these assumptions, the Einstein's field equations can be solved, leading to the so called *Friedmann equations* for the evolution of $a(t)$, which read:

$$\ddot{a} = -\frac{4\pi}{3}G\left(\rho + \frac{3p}{c^2}\right), \tag{1.5}$$

$$\dot{a}^2 + kc^2 = 8\pi G\rho a^2. \tag{1.6}$$

These two equations can be derived from each other through the assumpion of the adiabatic expansion of the Universe with the equation:

$$d(\rho c^2 a^3) = -pda^3. \tag{1.7}$$

CHAPTER 1. LARGE SCALE STRUCTURES AND COSMOLOGY

For a complete description of $a(t)$ we need the equations of state of the components:

$$p = p(\rho) = w\rho c^2, \tag{1.8}$$

where w is the equation of state parameter. The pressure-less matter component has $w = 0$, the radiative component has $w = 1/3$, while the cosmological constant can be interpreted as vacuum energy density with $w = -1$.

The expansion parameter in also linked to two quantities, the *cosmological redshift*, z, and the *Hubble parameter*, H. The redshift z is defined as:

$$z \equiv \frac{\Delta\lambda}{\lambda} = \frac{\lambda_o - \lambda_e}{\lambda_e}, \tag{1.9}$$

where λ_e is the emission wavelength of the source and λ_o is the observed wavelength. It can be shown that the link between the cosmological redshift of a source at time t and the expansion parameter is:

$$1 + z(t) = \frac{a(t_0)}{a(t)}, \tag{1.10}$$

where t_0 is the present time and $a(t_0) = 1$.

The Hubble parameter H is defined as:

$$H \equiv \frac{\dot{a}}{a}, \tag{1.11}$$

and measurements the rate of expansion of the Universe. The dot denotes the derivative with respect to the time coordinate. The Hubble parameter is parametrized, at the present time, as $H_0 = 100h$ km s^{-1} Mpc^{-1}.

The *critical density* is defined as:

$$\rho_{cr} = \frac{3H(z)^2}{8\pi G}. \tag{1.12}$$

It is possible to use the critical density into equation (1.6) obtainig a flat, close or open Universe for $\rho = \rho_{cr}$, $\rho > \rho_{cr}$ or $\rho < \rho_{cr}$ respectively. We can also define the *density parameter* for a component i as:

$$\Omega_i(t) \equiv \frac{\rho_i(t)}{\rho_{cr}(t)}. \tag{1.13}$$

The total density is:

$$\Omega = \sum_i \Omega_i. \tag{1.14}$$

Therefore, if Ω is $> 1, = 1, < 1$ the universe is closed, flat or open, respectively.

Finally, equation (1.5) can be rewritten as:

$$H^2(z) = H_0^2(1+z)^2 \left[1 - \sum_i \Omega_{0,w_i} + \sum_i \Omega_{0,w_i}(1+z)^{1+3w_i} \right], \qquad (1.15)$$

$$= H_0^2(1+z)^2 \left[1 - \Omega_{0,tot} + \Omega_{0,M}(1+z) + \Omega_{0,R}(1+z)^2 + \Omega_{0,\Lambda}(1+z)^{-1} \right],$$

where M denotes the matter, R the radiation and Λ the cosmological constant. The matter component is constituted by the dark matter, Ω_mm and the baryonic matter, Ω_b.

1.2 Formation and Evolution of Cosmic Structures

1.2.1 Jeans Theory in Expanding Universe

The first analytic study relative to the formation and evolution of the cosmic structures was done by Jeans. The Jeans linear theory (Jeans [1902]) studies the cosmic structure formation through the gravitational instability in the linear regime. This process is driven by the *density perturbations*, i.e., the oscillations in the primordial density fluid. The adimensional density perturbation is defined as:

$$\delta \equiv \frac{\delta\rho}{\rho} = \frac{\rho(\vec{x}) - \rho_b}{\rho_b}, \qquad (1.16)$$

where $\rho(\vec{x})$ is the matter density field at $\vec{x}$ and ρ_b is the mean matter density of the background Universe. We can define the *Jeans length* as:

$$\lambda_J = \sqrt{\frac{15 k_B T}{4\pi G \mu \rho_{gas}}}, \qquad (1.17)$$

where k_B is the Boltzmann constant, T is the temperature, μ is the mean molecular weight and ρ_{gas} is the gas mass density. Any δ on scales over λ_J can collapse and form structures. The Jeans linear theory assumes that: (i) the matter component of the Universe is pressureless and self-gravitating, (ii) the perturbation scale is larger than the Jeans length and (iii) $\delta << 1$. With these assumptions, we can write the continuity, the Euler and the Poisson equations as:

$$\left(\frac{\partial \delta\rho}{\partial t} \right)_{\vec{x}} + \frac{\rho_b}{a} \nabla_{\vec{x}} \vec{v} + 3H\delta\rho = 0, \qquad (1.18)$$

$$\left(\frac{\partial \vec{v}}{\partial t} \right)_{\vec{x}} + H\vec{v} = -\frac{c^2}{a} \nabla_{\vec{x}} \delta - \frac{1}{a} \nabla_{\vec{x}} \delta\phi, \qquad (1.19)$$

$$\nabla_{\vec{x}}^2 \delta\phi = 4\pi G a^2 \delta\rho, \qquad (1.20)$$

where the spatial derivates are calculated at the comoving coordinate $\vec{x}$ ($\vec{r} = a(t)\vec{x}$ is the proper distance), $\vec{v}$ is the peculiar velocity, with respect to the Hubble flow ($\dot{\vec{r}} = H(t)\vec{r} + \vec{v}$ is the total velocity of a fluid element) and $\delta\phi$ is the gravitational potential perturbation. In the linear regime, from equations (1.18), (1.19) and (1.20) we can write the *dispersion relation*:

$$\ddot{\delta} + 2H(t)\dot{\delta} = 4\pi G\rho_b\delta. \tag{1.21}$$

The solution is:

$$\delta(\vec{x}, t) = \delta_+(\vec{x}, t_i)D_+(t) + \delta_-(\vec{x}, t_i)D_-(t), \tag{1.22}$$

where $D_+(t)$ is the growth factor and $D_-(t)$ is the decrease factor, whereas $\delta_+(\vec{x}, t_i)$ and $\delta_-(\vec{x}, t_i)$ are two initial spatial distributions of the density field. The density growth factor depends on the component considered and on the cosmology. For a flat, matter-dominated Einstein-de Sitter Universe (hereafter EdS), where $\Omega_M = 1$ and $\Omega_\Lambda = \Omega_R = 0$, $D_+(t) \propto t^{2/3} \propto a$ whereas $D_-(t) \propto t^{-1} \propto a^{-3/2}$. For a closed, matter-dominated Universe, $D_+(t)$ grows faster than in EdS Universe, while in an open, matter-dominated Universe, it grows slower than in the EdS Universe. In a radiation-dominated Universe, the perturbations cannot grow, but they propagate like waves and are dispersed since the sound velocity is strongly relativistic.

For a model with $\Omega_M < 1$ and $\Omega_\Lambda \neq 0$, such as a flat one with $\Omega_M = 0.3$, there is an epoch, before the equivalence of between matter-Λ, where the perturbations can grow; after this epoch, the cosmological constant starts to be significant and the cosmic expansion proceeds faster than the gravitational collapse, causing a freezing of the perturbation growth.

As said before, λ_J is the minimum scale that a density perturbation needs to collapse. We can replace the minimum scale with the lower limit to the mass of perturbations that can grow and evolve. In the linear Jeans Theory, this is called *Jeans Mass*, M_J. M_J depends on the assumed model of the dark matter component. There are many proposals for the dark matter, but, historically, two models have been more important: the *Cold Dark Matter* model (hereafter CDM) and the *Hot Dark Matter* model (hereafter HDM). The CDM is constituted by massive, non-baryonic, collisionless and sub-relativistic particles, while the HDM is constituted by non baryonic, collisionless, massless and relativistic particles. The value of M_J depends on the velocity of the dark matter particles. Inside the particle horizon and at the *equivalence redshift*, z_{eq}, when $\rho_M = \rho_r$, the value of M_J is (for the two models):

$$M_{J,HDM}(z_{eq}) \approx 10^{12} \div 10^{15}M_\odot, \tag{1.23}$$

$$M_{J,CDM}(z_{eq}) \approx 10^5 \div 10^6M_\odot. \tag{1.24}$$

In the HDM paradigm, the first structures to be formed are the most massive and then the smallest structures are formed by fragmentation (*top-down* scenario). On

the contrary, in the CDM model, the first structures to collapse are the low-mass objects, and the more massive objects are formed through aggregation of these low-mass clumps (*bottom-up* scenario). There are many observations that support the CDM scenario, like the formation age of galaxies and galaxy clusters. The Milky Way appears older than the Local Group, and the formation redshift predicted by the CDM model, $z_f > 4$, is much higher than predicted by the HDM model, $z_f < 1$.

1.2.2   The Power Spectrum of the density flucutuations

Generally, $\delta(\vec{c})$ is studied statistically. The statistical analysis of our Universe is hampered because it is the only one. To bypass this problem, we use the *ergodic hypothesis*: an average over the probability ensemble is the same as an average over all spatial positions within a given realization. With this hypothesis, we can consider our universe as if it was composed by a set of many independent, isolated universes.

For the statistical analysis, it is convenient to use the Fourier transform of $\delta(\vec{c})$:

$$\widehat{\delta}(\vec{k}) = \frac{1}{(2\pi)^{3/2}} \int \delta(\vec{x}) \, e^{-i\vec{k}\cdot\vec{x}} d^3\vec{x}. \tag{1.25}$$

Furthermore, we define the *two − point correlation function* as:

$$\xi(r) \equiv \, < \delta(\vec{x}), \delta(\vec{x} + \vec{r}) > . \tag{1.26}$$

ξ describes the probability excess, or deficiency, of the density field with respect to a uniform distribution, and, given isotropy, it depends only on the separation distance $\|\vec{r}\|$. The correlation function is linked to another function, the *power spectrum*, $P(k)$, through the Fourier transform of $\xi(r)$:

$$\xi(r) = \frac{1}{(2\pi)^3} \int d^3\vec{k} \, P(k) \, e^{i\vec{k}\cdot\vec{x}}. \tag{1.27}$$

Similarly to $\xi(r)$, $P(k)$ depends only on $|\vec{k}|$. Futhermore:

$$P(k) = \, < |\widehat{\delta}(\vec{k})^2| > . \tag{1.28}$$

The power spectrum measures the amplitude squared mean of a mode with wave vector $\vec{k}$. For the inflationary models, since there is not a favoured scale for the perturbations, the primordial power spectrum is a power-law function $P(k) = Ak^n$, where n is the spectral index and A is the amplitude; according to the same models, n should be near the unity.

Since we cannot study any spatial point in the Universe, we have to use a window function, $W(\vec{x}, R)$, which filters the scales smaller than R. The density field and the variace of the perturbation field at the scale R can be written as:

$$\delta(\vec{x})_R = \delta(\vec{x}) \otimes W(\vec{x}, R) = \int \delta(\vec{y}) \, W(|\vec{x} - \vec{y}|, R) \, d\vec{y}, \tag{1.29}$$

$$\sigma_R^2 = < \delta_R^2 > = \frac{1}{(2\pi)^3} \int d^3\vec{k} \, k^2 \, P(k) \, \widehat{W}^2(\vec{k}, R). \tag{1.30}$$

From the form of the power spectrum, we can measure many cosmological parameters, as Ω_M, Ω_b, H_0, z_{eq} and n, whereas A can be measured by the analysis of the cosmic large scale structure (hereafter LSS) or the CMB anisotropies. Usually, the normalization is parametrized as σ_8, which is the variance within a comoving sphere of radius $R = 8h^{-1}\text{Mpc}$.

1.2.3 Nonlinear Evolution

When a perturbation is larger than the Jeans mass scale, it can grow up beyond the linear regime, and the Jeans theory is no longer valid. To study the formation and the evolution of the cosmic structures, a theory for the nonlinear evolution is necessary. In general, we must use numerical simulations. But there is one case where the analytic solution exists: the *spherical top-hat* collapse model (Gunn & Gott [1972]). This model assumes that the perturbations are spherical and the initial comovent velocity is null. The study of the perturbations is mathematically equivalent to a universe with density perturbation parameter $\Omega_p > 1$ in a EdS background universe ($\Omega_M = \Omega = 1$). Initially, the perturbation is in the linear regime, and its evolution can be written as:

$$\delta(t) = \delta_+(t_i) \left(\frac{t}{t_i}\right)^{2/3} + \delta_-(t_i) \left(\frac{t}{t_i}\right)^{-1}. \tag{1.31}$$

Futhermore, under these assumptions, given the initial density perturbation $\delta_i = \delta(t_i)$, only $3/5\delta_i$ can grow up with time, and the density perturbation parameter can be written as:

$$\Omega_p(t_i) = \Omega(t_i)(1 + \delta_i). \tag{1.32}$$

Since $\Omega_p(t_i) > 1$, $\Omega(t_i)(1 + \delta_i) > 1$. If $\Omega(t_i) \geq 1$, any perturbation can grow, but if $\Omega(t_i) \leq 1$, a threshold value exists and only perturbations beyond this threshold can grow with time. This value can be written as:

$$\delta_+ > \frac{3}{5} \frac{1 - \Omega_i}{\Omega_i(1 + z_i)}. \tag{1.33}$$

Given that the density perturbation is treated as a close universe, its evolution can be studied through the second Friedmann equation, written as:

$$\left(\frac{\dot{a}}{a_i}\right)^2 = H_i^2 \left[\Omega_p(t_i)\left(\frac{a_i}{a}\right) + 1 - \Omega_p(t_i)\right]. \tag{1.34}$$

The perturbation grows like the scale factor, until it reaches the maximum expansion at the *turn-around time*, t_m. At this point, the perturbation begins to collapse until it reaches a balance state at the time t_{vir} ($t_{vir} \approx 2t_m$). At t_{vir}, the virial condition is satisfied, $U = -2K$, where U is the potential energy and K is the kinetic energy. The perturbation over-density at t_m is $\delta(t_m) \approx 4.6$, whereas $\delta(t_{vir}) \approx 180$. In the Jeans linear theory, the perturbation over-density at t_m and t_{vir} are $\delta(t_m) \approx 1.07$ and $\delta(t_{vir}) \approx 1.686$, respectively.

1.2.4 The Press-Schechter Mass Function

The *Halo Mass Function* (HMF) measures the number density of the collapsed object in a given comoving volume, at redshift z and with mass between M and $M + dM$. The *Press-Schechter* Function (Press & Schechter [1974], PS) is a powerful tool to model the HMF and the cosmic structures evolution. The function was found through the following assumptions: (i) a Gaussian density perturbation distribution, as supported by inflationary models; (ii) the spherical top-hat collapse model with threshold value from the linear theory, $\delta_c = 1.686$; (iii) the Jeans linear theory for the perturbation evolution, and (iv) the EdS Universe. The PS function can be written as follows:

$$n(M,z)dM = \sqrt{\frac{2}{\pi}}\frac{\delta_c}{\sigma_M(z)}\frac{\bar{\rho}_M(z)}{M^2}\left|\frac{d\ln\sigma_M}{d\ln M}\right|\exp\left(-\frac{\delta_c^2}{2\sigma_M^2(z)}\right)dM. \tag{1.35}$$

This function depends only on the *peak height*, defined as:

$$\nu \equiv \delta_c(z)/\sigma_M(z). \tag{1.36}$$

The cosmology dependence is in σ_M which barely depends on the power spectrum form, but that depends strongly the amplitude.

1.3 The Current Cosmological Model

The current favoured cosmological model is called the "*Lambda Cold Dark Matter*" (hereafter ΛCDM). It is a flat universe, dominated by the cosmological constant and a smaller fraction of cold dark matter; the baryonic matter component is only a small percentage. This model is supported by many observations which enable us

Parameter	68% limits	Definition
H_0	67.74 ± 0.45	Current expansion rate in km s^{-1} Mpc^{-1}
Ω_Λ	0.6911 ± 0.0061	Dark energy density divided by the critical density today
Ω_m	0.3089 ± 0.0062	Matter density today divided by the critical density
σ_8	0.8158 ± 0.0086	RMS matter fluctuations today in linear theory
$\Omega_b h^2$	0.02230 ± 0.00014	Baryon density today
$\Omega_m h^2$	0.14170 ± 0.00097	Total matter density today
n	0.9667 ± 0.0040	Scalar spectrum power-law index

Table 1.1: Cosmological parameters from Planck Collaboration [2016].

to precisely estimate the cosmological parameters. The most precise measurements of the cosmological parameters are given by the ESA *Planck* (Planck Collaboration [2016], Planck15 hereafter) mission through measurements of the CMB temperature and polarization anisotropies. The most recent estimates are summarized in table 1.1.

2

The Mass-Concentration Relation

The galaxy clusters are the largest nearly virialized collapsed objects in the observable Universe and they are the last to form. Therefore, they can be used to understand the formation and evolution of cosmic structures. There are several ways to do this. In this Thesis, we are interested to use the Mass-Concentration relation (c-M hereafter). In this chapter, we describe the theoretical background of the c-M relation, section 2.1, and some semi-analytic models that try to explain its dependence on cluster mass and redshift, section 2.2. Moreover, we present the models that we have used for our work, section 2.3.

Let us briefly review some definitions that we use in this thesis. We define M_Δ as the mass enclosed within a sphere with radius r_Δ which encloses the region where the mean density is Δ times the critical density ρ_{cr} at the cluster redshift. M_{vir} is the virial mass enclosed in a spherical volume with radius r_{vir} within which the mean density is Δ_{vir} times the ρ_{cr} at that redshift, where the value of Δ_{vir} is an over-density that varies with redshift. It can be approximated as $\Delta_{vir}(z) = 18\pi^2 + 82x + 39x^2$, where $x = \Omega(z) - 1$ (Bryan & Norman [1997]).

2.1 Theoretical background

The structure formation paradigm is based on the gravity instability for dark and baryonic matter. To study the formation of the structures, we can exploit N-body simulations. Some of the first results came from Navarro, Frenk & White [1997] (hereafter NFW [1997]). They used several N-body simulations with different cosmological models to study the equilibrium density profiles of dark matter halos (see section 2.2.1 for details). They found that all the profiles have the same shape, independent of the halo mass, the initial density fluctuation spectrum and the values of the cosmological parameters. They proposed a simple formula to
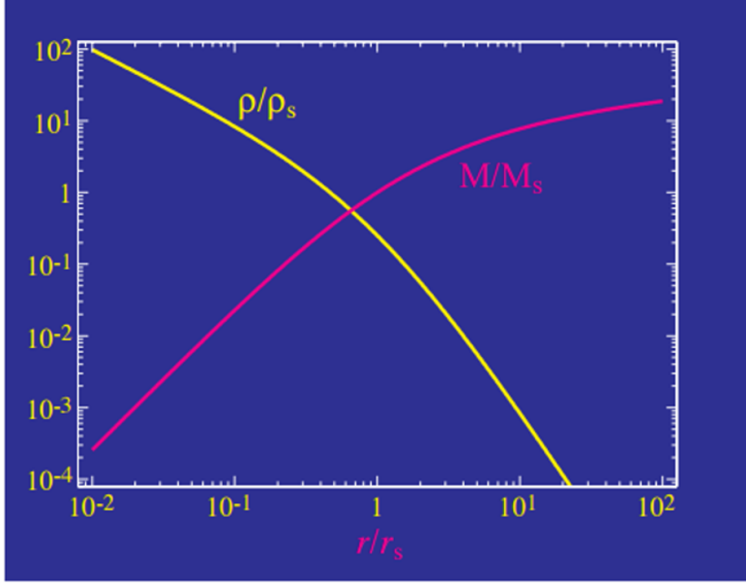
Figure 2.1: The yellow line is the NFW density profile scaled to ρ_s. The magenta line is the cumulative mass enclosed within the radius r/r_s.

accurately fit the density profile as function of the radius, the NFW profile:

$$\frac{\rho(r)}{\rho_{cr}} = \frac{\delta_s}{(r/r_s)\left(1 + r/r_s\right)^2},$$

(2.1)

where r_s is the scale radius, defined as the raidius where the logarithmic density slope is -2, and δ_s is a characteristic dimensionless density.

This profile has an asymptotic behavior that tends to r^{-1} and r^{-3} for $r \ll r_s$ and $r \gg r_s$, respectively. Figure 2.1 shows the NFW density profile scaled, yellow line, and the cumulative mass enclosed within the radius r/r_s for a NFW profile, magenta line. They also introduced the *concentration* parameter of a halo, c, defined as:

$$c_\Delta \equiv \frac{r_\Delta}{r_s},$$

(2.2)

where $\Delta = 200$. It can be also defined as $c_{vir} = r_{vir}/r_s$. In the following, by c we mean the c_{200}. The concentration parameter c and the characteristic density δ_s are linked by the relation:

$$\delta_s = \frac{200}{3} \frac{c^3}{\ln(1 + c) - c/(1 + c)}.$$

(2.3)

Given a halo with a NFW density profile, the total mass $M_{tot}(< r)$ enclosed in an

arbitrary radius r is:

$$M_{tot}(< r) = 4\pi r_s^3 \rho_s f(x), \qquad (2.4)$$

$$f(x) = \ln(1 + x) + \frac{x}{1 + x}, \qquad (2.5)$$

where $\rho_s = \rho_{cr}\delta_s$ and $x = r/r_s$. If $r = r_\Delta = r_{200}$, and then $c_\Delta = c_{200}$, the mass enclosed in this radius is $M_{200} = 200\rho_{cr}4/3\pi r_{200}^3$, where $r_{200} = r_s c_{200}$. For a given halo mass, there are two free parameter in equation (2.1), that are r_s and ρ_s. Alternatively, we can use M_{200} and c_{200}.

Several authors studied and modelled the concentration parameter, its cosmological implication and its relation with the cluster mass or redshift (NFW [1997], Giocoli et al. [2012], Muñoz-Cuartas et al. [2011]). Many authors found a common behaviour with the cluster mass, that is the concentration is larger for lower mass clusters, and it is smaller for large mass clusters (NFW [1997]). This outcome is interpreted as a signature of the dark matter, that is the dark matter halos are able to keep the memory of the density of the universe at the epoch of collapse. Moreover, the redshift at which a halo was formed depends on the cosmological parameters Ω_M and σ_8. This means that lower values of collapse redshift are expected for cosmologies with lower values of Ω_M and σ_8. Consequently, the concentration results to be smaller. For this reason, the c-M relation is connected to and provides information on the cosmological model within which halos form. Another common behaviour is that the concentration is larger when the relaxed halos are considered, than the unrelaxed halos (Neto et al. [2007], Prada et al. [2012] and Bhattacharya et al. [2013]). This behaviour is due to the rapidly evolving mass distribution that accompanies an accretion event.

2.2 Semi-analytic models

In this section, we present different semi-analytic models which describe the evolution of the c-M relation.

2.2.1 The Collapse Redshift

NFW [1997] analyzed different cosmologies, i.e., the Einstein-de Sitter cosmology, with $\Omega_M = 1$ and different power spectra index n, a open universe with $\Omega_M = 0.1$, and a flat ΛCDM cosmology, with $\Omega_M = 0.25$ and $\Omega_\Lambda = 0.75$. They ran different cosmological simulations, from 64^3 to 10^6 particles in a periodic cube with size from 15h^{-1}Mpc to 46.67h^{-1}Mpc .

NFW [1997] studied the mass dependence of δ_c, or c. They found that there is a correlation: the characteristic density of a halo increases toward lower masses in all the cosmological models. Given that the structures at lower mass collapse
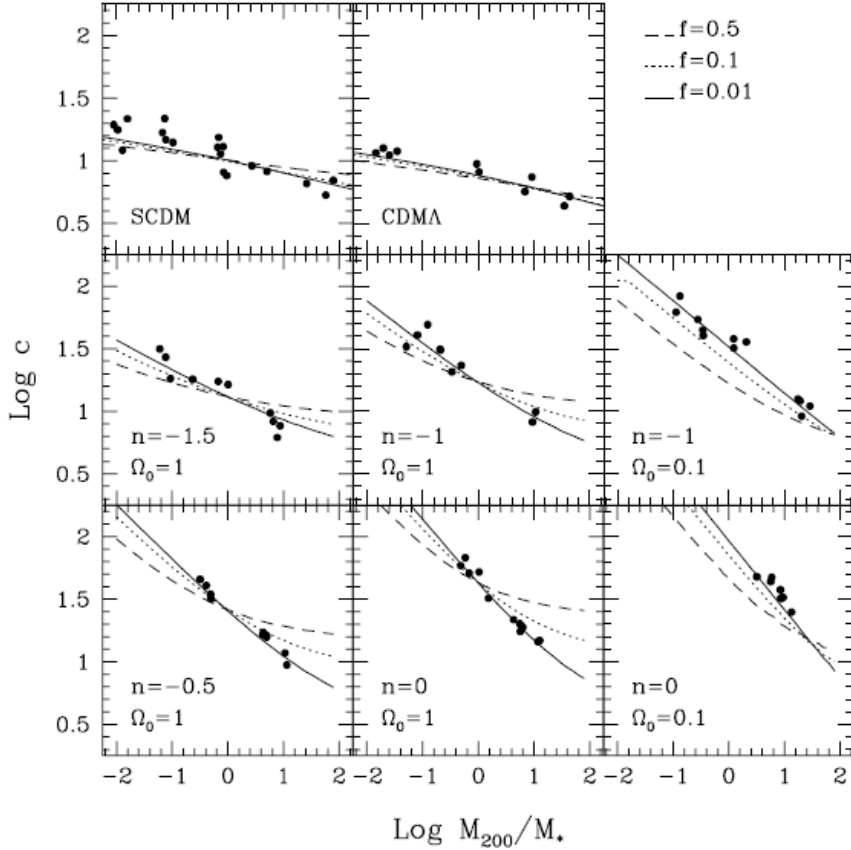
Figure 2.2: Correlation between the mass of a halo and its concentration, Navarro, Frenk & White [1997]. The dashed, dotted and full lines correspond to the parameter $f = 0.5$, 0.1 and 0.01, respectively. The dots are the results from several N-body simulations implemented. The parameter M_* is the "non-linear" mass defined as $\Delta_0^2[M_*(z)] = \delta_{cr}^2(z, \Omega_0, \Lambda)$ and it is used to scale the scale-free simulations to physical units and to compare different cosmological models.

first, in the hierarchically clustering universe, their result supports the idea that the δ_c-M and the c-M relations are a result of this effect. NFW [1997] proposed a simple model to describe this relation.

The model assigns to each halo of mass M, identified at $z = 0$, a collapse redshift, $z_{coll}(M, f)$, defined as the time at which half mass of the halo was first contained in several progenitors more massive than a fraction f of the final mass. The z_{coll} can be computed by using the Press-Schechter formalism,

$$\text{erfc}\left\{w_f\right\} = \frac{1}{2}, \tag{2.6}$$

$$w_f = \frac{\delta_t(z_{coll}) - \delta_t(z_0)}{\sqrt{2[\Delta_0^2(fM) - \Delta_0^2(M)]}}, \tag{2.7}$$

where $\Delta_0^2(M)$ is the linear variance of the power spectrum at $z = 0$ smoothed with a top-hat filter of mass M and $\delta_t(z)$ is the density threshold for spherical collapse at redshift z, which evolves as δ_+. If $f \ll 1$, $\Delta_0^2(fM) \gg \Delta_0^2(M)$ and $\delta_t(z_{coll}) \gg \delta_t(z_0)$. In this limit, equation (2.7) reduces to $\delta_t(z_{coll}) \propto \Delta_0(fM)$ and the characteristic density of a halo, as well as the concentration c, is proportional to the mean matter density of the universe at the time z_{coll}:

$$\delta_c(M|f) = C\Omega_M[1 + z_{coll}(M, f)]^3, \tag{2.8}$$

where C is a constant that depends on f and on the power spectrum. From equation (2.8), we can see the strong dependence of the concentration to the cosmological parameter Ω_M. Figure 2.2 shows the results for the concentration parameter c as obtained from the N-body simulations for several cosmologies implemented by NFW [1997]. The lines shows the results of equation (2.8) for different values of f. In all simulations, the model $f = 0.01$ provides a good fit.

2.2.2 The Assembly History

As shown by NFW [1997], the concentration can be the consequence of the mass assembly history of halo, because the structure of a halo depends on it. The concentration is related to the ratio of the background density at z_{coll}, at fixed f, to that at which the halo was identified. The exact dependence is a function of the expansion history of the background cosmology. Zhao et al. [2009] provided a prescription to relate the halo concentration, c_{vir}, to its mass assembly history using the time at which the halo had assembled 4 per cent of its mass:

$$c_{vir} = 4\left[1 + \left(\frac{t_1}{3.75t_{0.04}}\right)^{8.4}\right]^{1/8}, \tag{2.9}$$

with a scatter in the log-space equal to 0.12. This relation implies that the c-M relation, and its dependence on cosmology, comes from the fact that t_f/t_1 has a distribution that depends on halo mass. The mass and cosmology dependence of t_f/t_1 is not straightforward.

Giocoli et al. [2012] studied the mass growth histories for the dark matter halos. Their numerical simulation was run in a flat ΛCDM universe with parameters $(\Omega_M, \sigma_8, h, \Omega_b h^2) = (0.3, 0.9, 0.7, 0.0196)$. They followed the evolution of 400^3 particles in a periodic box of size $110h^{-1}$Mpc and the individual particle mass was $1.73 \times 10^9 h^{-1}M_\odot$. From this simulation, they built up the merger history tree for each halo more massive than $10^{11.5}h^{-1}M_\odot$. They retraced the mass growth history

of the "main progenitor", $m_{MP}(z)$, defined as the one halo at $z+dz$ which provides the most mass to the halo at z.

They developed a model to estimate $m_{MP}(z)$ fitting the formation time distribution, $p_f(> z_f|M_0, z_0)$, defined as the earliest time that the main branch of the merger tree contains a fraction f of the final mass, that is $m_{MP}(z) > fM_0$ (z_f is equal to z_{coll}). They defined the $p_{MP}(m, z|M_0, z_0)$ as the probability that $m_{MP}(z) = m$. With this definition, their formation time distribution results to be $p_f(> z_f|M_0, z_0) = p_{MP}(fM_0, z_f|M_0, z_0)$. For $f > 1/2$, the analytic formula for p_f as a function of the scaled variable can be written as w_f, defined in equation (2.7). Their model can fit the formation time distribution for each value of f, and it is:

$$p(w_f) = A_0 w_f^{0.63 f^{-2/3}} e^{-\gamma_f w_f^{\beta_f}}.$$ (2.10)

With this model, they found that there is a weak correlation between the formation time with $f = 1/2$ and $f = 0.04$. They provided a formula for the concentration using the information about $t_{0.04}$ and $t_{0.5}$ to remove some scatter in c_{vir}. That formula reads:

$$\log_{10} c_{vir} = \log_{10} 0.45 \left[4.23 + \left(\frac{t_1}{t_{0.04}} \right)^{1.15} + \left(\frac{t_1}{t_{0.5}} \right)^{2.3} \right].$$ (2.11)

This equation has a scatter of 0.10 and can be reduced using complementary information, i.e., about other formation time distributions.

2.2.3 The Redshift Evolution

The evolution of the concentration can also be expressed in terms of the redshift. Muñoz-Cuartas et al. [2011] studied the redshift evolution of dark matter halo structural parameters, as concentration, shape, and spin. They ran simulations for different box sizes and number of particles to examine the halo masses in the range $10^{10}h^{-1}M_\odot < M < 10^{15}h^{-1}M_\odot$, up to redshift 2. They set the cosmological parameters to the 5-years results of the $WMAP$ mission, Hinshaw et al. [2008], namely $(\Omega_M, \Omega_\Lambda, \sigma_8, h, n) = (0.258, 0.742, 0.796, 0.72, 0.963)$.

To compute the concentration of a halo, they first determined its density profile by fitting the NFW profile. With the scale radius r_s, obtained from the fitting procedure, and the virial radius, obtained from a spherical over-density algorithm, they measured the concentration c_{vir}.

They studied the redshift evolution of the c-M relation for the relaxed halos only. A halo is identified as relaxed when the rms of the NFW fit to the density profile is lower than 0.5 and when the distance between the most bound particle, used as the centre of the density profile, and the centre of mass of the halo in lower than 0.07, in unit of the virial radius.
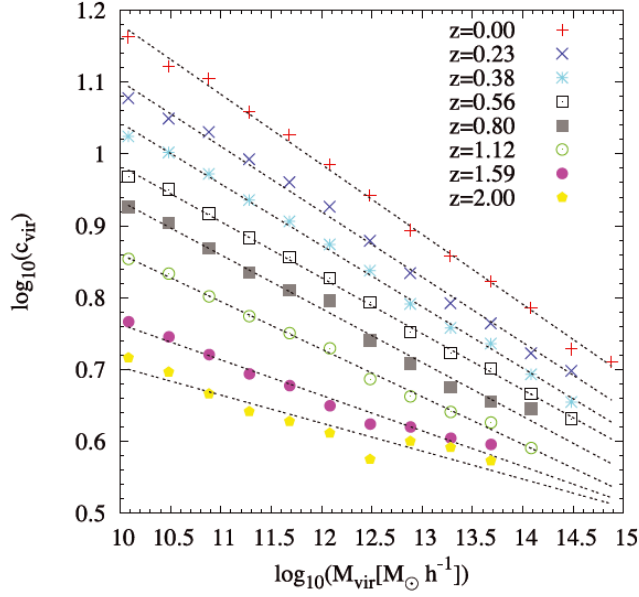
Figure 2.3: Mass and redshift dependence of the concentration parameter, Muñoz-Cuartas et al. [2011]. The points indicate the median concentration in a given mass bin at fixed redshift. Lines show the linear fit of the points at fixed redshift.

Figure 2.3 shows their results for the median c_{vir}-M_{vir} relation for the relaxed halos at different redshifts. Dots represent the concentration computed from the simulations. The lines represent their linear fit, written as $\log(c) = a(z)\log(M_{vir}) + b(z)$, where $a(z)$ and $b(z)$ depends on the redshift. They also measured how the concentration evolves as a function of redshift at fixed halo mass. They observed that the lower halo mass has a faster concentration evolution. This effect produces a change in the slope of the c-M relation with redshift, the relation flattens. Their fitting formulae are able to recover this trend.

To understand the concentration evolution, since c_{vir} is defined as the ratio of r_{vir} and r_s, they looked the time evolution of this two radii to extract some physical insights into the evolution of c_{vir}. At first, they studied the average mass accretion history for the dark matter halos, $M_{vir}(z)$, and they proposed a two-parameters function to fit their data.

Subsequently, they studied the redshift evolution of the virial radius. For all mass scales, they found that the virial radius increases with decreasing redshift, reaching a maximum, that depends on the mass of the halo, and then starts a slow decrease. This behavior can be seen from the virial radius definition:

$$r_{vir}(z) = \left[\frac{3M_{vir}(z)}{4\pi\Delta_{vir}(z)\rho_{cr}(z)} \right]^{1/3}. \tag{2.12}$$

The growth of the virial radius depends on the factors $M_{vir}(z)$ at the numerator and $[\Delta_{vir}(z)\rho_{cr}(z)]^{-1/3}$ at the denominator. At high redshift the growth of $M_{vir}(z)$ dominates, and therefore r_{vir} also grows. Vice versa, at low redshift, the growth rate becomes weaker compared to the decrease of the factor $[\Delta_{vir}(z)\rho_{cr}(z)]^{-1/3}$, slowing the growth of r_{vir}. The redshift at which r_{vir} begins to decrease, i.e. the growth rate becomes weaker, depends on the mass of the halo. The redshift evolution of r_s is very similar of the evolution of r_{vir}. It grows with the time, reaches a maximum and then starts to decrease, and, once again, the redshift at which this maximum is achieved depends on the halo mass.

The behaviour of r_s and r_{vir} are reminiscent of the time evolution of a perturbation in the spherical collapse model, section (1.2.1). The inner region of a halo, within r_s, evolves in a decoupled way compared to the global perturbation, within r_{vir}. For this reason, the inner region can be studied as a perturbation of density ρ_s that evolves within the background density $\rho_{vir}(z) = \Delta_{vir}(z)\rho_c(z)$. In analogy with the spherical collapse model, they found a fitting formula to describe the evolution of the density contrast $\Delta_s(z) = \rho_s(z)/\rho_{vir}(z)$:

$$\Delta_s(z) = \frac{A}{z + \epsilon(M)}, \tag{2.13}$$

where A is a constant and $\epsilon(M)$ is a function of the final halo mass, $M_{vir}(z=0)$. This equation implies that $\rho_s > \rho_{vir}$ at all redshifts, $\Delta_s(z)$ is a growing function of the redshift, implying a faster growth of the inner density with respect to the mean density of the halo, and, finally, $\Delta_s(z)$ depends on the final halo mass.

Based on the above considerations, they interpreted the flattening of the c_{vir}-M_{vir} relation as follows: at early times r_s grows simultaneously with r_{vir}, therefore the concentration of the halo stays approximately constant or it slightly increases. When r_s decreases its growth rate and start to decrease, the concentration grows rapidly. For high-mass halos, the decoupling of the inner region from the outermost part happens at later times compared to low-mass halos. As a consequence, more massive halos have a more extended period in which the concentration is a slowly growing function of time. The moment when the inner part of the halo decouples from the outer one is strongly mass dependent. Smaller structures decouple earlier than more massive structures. This effect explains the change in the slope in the c_{vir}-M_{vir}, as described by the evolution of $a(z)$.

2.3 Models adopted

Many authors proposed several models for the c-M relation fitting several cosmological simulations. In this section, we present the models we have used for our work.

2.3.1 Bullock et al. [2001]

Bullock et al. [2001] (B01 hereafter) modelled the c-M relation as follows: they defined the collapse redshift, z_c, as the redshift at which the collapsing mass, $M_*(z_c)$, is equal to a fraction f of the halo mass at the observation redshift, z, as follows:

$$M_*(z_c) = f M_{vir}(z). \tag{2.14}$$

They defined a general characteristic density $\widetilde{\rho}_s$ as follows:

$$M_{vir} = \frac{4\pi}{3} r_s^3 \widetilde{\rho}_s. \tag{2.15}$$

Furthermore, they measured the halo mass in units of the typical halo mass at the same epoch as $\mu = M_{vir}(z)/M_*(z)$. B01 identified the characteristic density of the halo at the observation redshift with the mean density of the universe, ρ_u, at the collapse redshift, $\widetilde{\rho}_s(z) = K^3 \Delta_{vir}(z)\rho_u(z_c)$, where K is a constant to be determined by calibration against numerical simulations and represents the concentration of the halo at the collapse redshift. Finally, they found a simple expression for c_{vir} as follows:

$$c_{vir}(\mu, z) = K \left(\frac{1 + z_c}{1 + z} \right). \tag{2.16}$$

The model is fully determined by eqs. (2.14) and (2.16), given the values of the two parameters f and K. They predicted a power-law relation for the c-M relation, and that for halos of the same mass the concentration is proportional to $(1+z)^{-1}$.

The B01 model has an improved version powered by Macció et al. [2008] (M08 hereafter). M08 assumed, differently from the B01 model, that the characteistic density of the halo $\widetilde{\rho}_s(z)$ is independent of redshift, i.e. $\widetilde{\rho}_s(z) = \widetilde{\rho}_s(z_c)$. Under these hypotheses, the c_{vir} relation appears to be:

$$c_{vir}(M_{vir}, z) = K \left[\frac{\Delta_{vir}(z_c)}{\Delta_{vir}(z)} \frac{\rho_u(z_c)}{\rho_u(z)} \right]^3. \tag{2.17}$$

In case of the $\Delta = 200$ halo definition, the relation become:

$$c_{200}(z) = K_{200} \left[\frac{\rho_{cr}(z_c)}{\rho_{cr}(z_c)} \right]^3 = K_{200} \left[\frac{H(z_c)}{H(z)} \right]^{2/3}, \tag{2.18}$$

so that the evolution in c_{200} is given by the evolution of the Hubble parameter. They modified the B01 model by taking into account the redshift dependence of the halo density contrast. In an EdS universe, $\Omega_M(z) = 1.0$ and the M08 model predicted the same relation $c_{vir}(z)$ as for the B01 model. For a ΛCDM universe, Ω_M is a function on redshift and the differences between $\Omega_M(z_c)$ and $\Omega_M(z)$ can

Name	Ω_m	h	σ_8	n	Ω_b
$WMAP1$	0.268	0.71	0.900	1.000	0.044
$WMAP3$	0.238	0.73	0.750	0.950	0.044
$WMAP5$	0.258	0.72	0.796	0.963	0.044

Table 2.1: The values of the cosmological parameters for the $WMAP1$, $WMAP3$ and $WMAP5$ cosmologies.

be significant, and thus there are difference between the $c_{vir}(z)$ calculated via the B01 and M08 models.

M08 fitted their model with a large suite of N-body simulations, in which they let K as a free parameter. They used the $WMAP1$, $WMAP3$ and $WMAP5$ flat cosmologies, and the value of the cosmological parameters are listed in table 2.1. For each cosmology they ran the simulations for several box size, 20, 40, 90, 180, 300, 360h^{-1}Mpc, with 250^3, 300^3, 400^3, 600^3 dark matter particles, and the particle mass varies between 1.37×10^7h^{-1}M$_\odot$ and 1.87×10^{10}h^{-1}M$_\odot$. They could cover the entire halo mass range from 10^{10}h^{-1}M$_\odot$ halos, that host dwarf galaxies, to 10^{15}h^{-1}M$_\odot$ massive clusters. All simulations were performed with the `PKDGRAV` tree code.

In all simulations, dark matter halos are identified using a spherical overdensity algorithm. They fit their halos with a NFW profile, and define the rms of the fit as:

$$\rho_{rms} = \frac{1}{N} \sum_i^N (\ln \rho_i - \ln \rho_t)^2, \tag{2.19}$$

where ρ_i is the density of the i-shell of the simulated halo and ρ_t is the fitted NFW density distribution. Finally, they define the concentration of the halo, $c_{vir} \equiv r_{vir}/r_s$, using the virial radius obtained from the spherical over-density algorithm.

They used two different samples of halos: "all", which includes all halos with at least 500 particles within the virial radius, N_{vir}, and "$relaxed$", which includes halos with $N_{vir} > 500$, $\rho_{rms} < 0.5$ and the distance between the most bound particle $x_{off} < 0.07$ in units of the r_{vir}.

Figure 2.4 shows the c-M relation obtained from their simulations for all three cosmologies, separately for all halos, left panel, and for the sub-sample of relaxed halos, right panel. The solid lines correspond to the best-fitting c-M relations
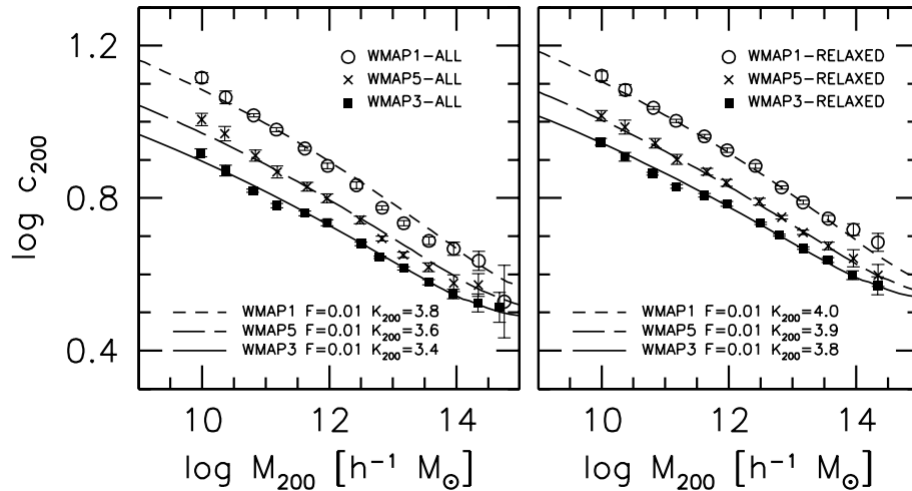
Figure 2.4: The c_{200}-M_{200} relation from Macció et al. [2008] for the three cosmologies. The points show their results from the simulation. The solid line show the revisited B01 model. The left panel refers to the all halo sample, while the right panel to the relaxed halo sub-sample.

obtained using the revisited B01 model. The best-fitting values of K are indicated in the figure. The M08 model can fit the simulation data remarkably well over the entire range of halo masses probed, and for all three cosmologies. The three different cosmologies require a different normalization parameter K. The best-fitting value of K has to be determined empirically using high-resolution numerical simulations.

For the rest of this thesis, we will refer to the M08 model as B01. `Colossus`, see section 3.1, adopted $f = 0.01$ and $K = 3.85$. In this case, the value of K is a constant and it is not determined using high-resolution numerical simulations. `Colossus` adopted this value because Buote et al. [2007] showed that cosmology dependence of the parameter K is small.

2.3.2 Prada et al. [2012]

The study of Prada et al. [2012] (P12 hereafter) was based on four N-body simulations, the Millenium-I and II, the Bolshoi and the Multidark simulation, see table 2.2.

They covered a large range of scales, going from halos hosting dwarf galaxies to massive galaxy clusters. This corresponds to six orders of magnitude in mass. The MS-I and MS-II simulations were run with the `GADGET-2` and `GADGET-3` tree-PM codes, respectively. The Bolshoi and Multidark simulations were run with the `ART`

Name	L_{box} [h^{-1}Mpc]	N_p	M_p [h^{-1}M$_\odot$]	Ω_M	Ω_b	n	h	σ_8
MS-I	500	2160^3	8.61×10^8	0.25	0.0450	1.00	0.73	0.90
MS-II	100	2160^3	6.89×10^6	0.25	0.0450	1.00	0.73	0.90
Bolshoi	250	2148^3	1.35×10^8	0.27	0.0469	0.95	0.70	0.82
MultiDark	1000	2148^3	8.63×10^9	0.27	0.0469	0.95	0.70	0.82

Table 2.2: Characteristics of the N-body simulations considered by Prada et al 2012. L_{box} is the side length of the simulation box, N_p is the number of particles, M_p is the mass particle.

code, an adaptive mesh refinement type code.

They studied only the distinct halos containing more than 500 particles. A halo is called distinct if its center is not inside the virial radius of another halo. Their over-density threshold is $\Delta = 200$. They defined an offset parameter x_{off} as the distance between the center of the halo and the center of mass of halo in units of the virial radius. To define the relaxed halos, they also considered the spin parameter λ and the virial ratio $2K/|U| - 1$, where K and U are the total kinetic and potential energies respectively. A halo is called relaxed if it has $x_{off} < 0.1$, $\lambda < 0.1$ and $2K/|U| - 1 < 0.5$.

To estimate the halo concentration, they used two methods. The first one fits the density profiles as NFW halos, while the other one is a method proposed by Klypin et al. [2011], based on the relation between the maximum circular velocity V_{max}, the virial velocity V_{200} and the halo concentration. Assuming an NFW halo density profile, the V_{max}/V_{200} ratio is given by:

$$\frac{V_{max}}{V_{200}} = \left(\frac{0.216c}{f(c)} \right)^{1/2}, \tag{2.20}$$

where $f(c)$ is:

$$f(c) = \ln(1 + c) - \frac{c}{1 + c}. \tag{2.21}$$

They measured the V_{max}/V_{200} ratio for each halo and found the concentration by solving numerically equations (2.20) and (2.21). They demonstrated that the two methods give similar concentrations, with a deviation less than 15%, therefore they used the concentration based on the V_{max}/V_{200} method.

Their V_{max}/V_{200}-M_{200} results are reported in figure 2.5. In all of their simulations, they found an upturn of the velocity ratio, and, hence, the halo concentration
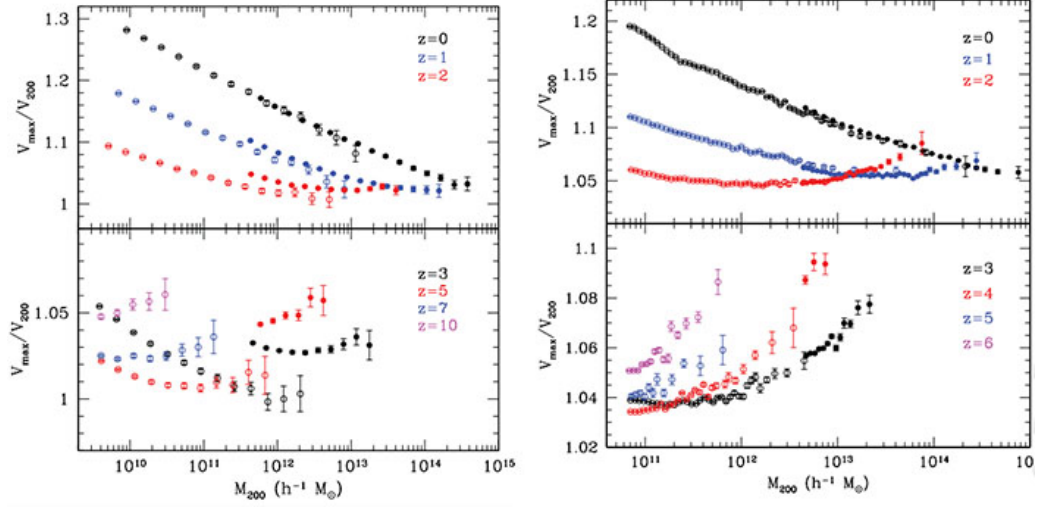
Figure 2.5: The ratio V_{max}/V_{200} from Prada et al. [2012], as a function of M_{200} for distinct halos at different redshifts. In the left panel, filled and open symbols are for the MS-I and MS-II simulation respectively. In the right panel, filled and open symbols are for the Bolshoi and MultiDark simulation respectively.

increases with the halo mass at higher redshift. Moreover, they found the difference between the several simulations, but this is due to the different cosmological parameters used.

They also studied the c-$\log \sigma^{-1}$ relation. The parametrization in terms on σ embodies most of the evolution of the concentration with redshift, helps to understand the differences due to the cosmological parameters, and allows for clearer comparison between different simulations. They found that the relation shows a U-shape with a minimum at a well-defined scale $\log \sigma^{-1} \simeq 0.15$. At low $\log \sigma^{-1}$, the concentration decrease with $\log \sigma^{-1}$, and increase at larger $\log \sigma^{-1}$. The time evolution of the concentration can be described as a decrease of the minimum value of the U-shaped concentration curves with increasing redshift and a slight shift of the position of the minimum to smaller values of $\log \sigma^{-1}$. They proposed some simple hypotheses to understand the nature of the upturn. A non-equilibrium effect cannot explain the upturn because when they select relaxed halo only, the magnitude of the upturn increase. They studied how the dynamical state of the halos is related to the average radial velocity profile, $\langle V_r \rangle$, and the velocity anisotropy parameter, β. At large masses, they found a signature of in-fall given by large negative $\langle V_r \rangle$ and larger β. These results indicated that the orbits are preferentially radial for halos in the upturned part of the c-M relation. At low $\log \sigma^{-1}$ they did not show an in-fall pattern and β is significantly smaller.
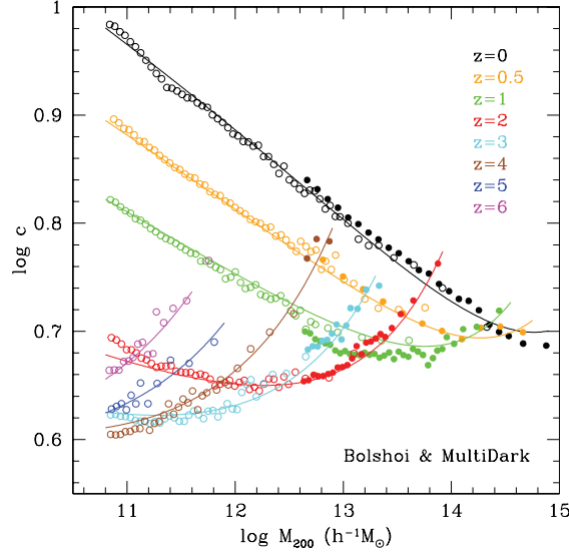
Figure 2.6: The c-M relation for distinct halos at different redshift in the Bolshoi (open symbols) and MultiDark (filled symbols). The solid line is the analytic relation proposed by Prada et al. [2012].

They also proposed an analytic model for the c-σ relation, as follows:

$$c(M, z) = B_0(x)C(\sigma'), \tag{2.22}$$

$$\sigma' = B_1(x)\sigma(M, x), \tag{2.23}$$

$$C(\sigma') = A\left[\left(\frac{\sigma'}{b}\right)^c + 1\right]\exp\left(\frac{d}{\sigma'^2}\right), \tag{2.24}$$

where A, b, c and d are constant, $x \equiv (\Omega_{\Lambda,0}/\Omega_{m,0})^{1/3}$ and B_0 and B_1 are functions of the minimum of the c-σ relation. Fig. 2.6 shows the c-M relation for the Bolshoi (open symbol) and Multidark (filled symbol) simulations at different redshift. Their model (lines) is able to reproduce all the features that they obtained, namely the decline of concentration with mass, its flattening and the upturn at high redshift/mass.

2.3.3 Bhattacharya et al. [2013]

The study of Battacarya 2013 (B13 hereafter) was based on tree N-body simulations. For the three simulations, they used the WMAP7 cosmoloy, where $\Omega_m = 0.25$, $\Omega_b = 0.043$, $n = 0.97$, $\sigma_8 = 0.8$ and $h = 0.72$. The largest simulation was implemented with the `HACC` code (Hardware/Hybrid Accelerated Cosmology).

Code	L_{box} [h^{-1}Mpc]	N_p	M_p [h^{-1}M$_\odot$]
HACC (HACC)	2000	2048^3	6.5×10^{10}
GADGET-2 (G)	512	1024^3	5.3×10^{10}
GADGET-2 (GS)	128	513^3	1.1×10^9

Table 2.3: N-body simulations carried out by Batthacarya et al 2013. L_{box} is the side length of the simulation box, N_p is the number of particles, M_p is the mass for each particle.

The smaller simulation was carried out with `GADGET-2`. The characteristics of their simulations are listed in table 2.3. They could study the mass range from 2×10^{12} to 2×10^{15}h^{-1}M$_\odot$. They selected halos using a friend-of-friends (FOF) finder with linking length b = 0.2 and with more than 2000 particles. This is the "*all*" sample. From this sample, they selected a sub-sample, the "*relaxed*" halos where the difference between the location of the center of mass and the center of the density maximum is $< 0.07 r_{vir}$.

They modelled each halo with a NFW profile and computed the concentrations at two radii corresponding to $\Delta = 200$ and Δ_{vir}. Halo profiles were fitted in the radial range $\sim (0.1-1)r_{vir}$. They excluded the central core because the real clusters are sensitive to the effects of baryonic physics, and in the numerical simulations there are several errors due to the limitation in resolution. They calculated the c-M relation by weighting the individual concentration by the mass,

$$c(M) = \frac{\sum_i c_i M_i}{\sum_i M_i}, \tag{2.25}$$

where the sum is over the number of the halos in a mass bin, N_i. The mass of the bin is given by $M = \sum_i M_i / N_i$. Their c-M relation becomes flatter at z>0, with the full sample relation flattening more at higher redshift. The relation for the relaxed sample has a 10% higher amplitude than the full sample, while the relation in the Δ_{vir} case has about a 30% higher normalization.

They tried to explain the flattening of their c-M relation. For this reason, they parametrized the halo mass functions as a function of the peak height parameter ν, equation (1.36). The shape of the c-ν relation is approximately constant over the redshift range z = 0-2. Figure 2.7 shows their results for the c-ν relation. The evolution of $c_{200}(\nu)$ follow the linear growth factor as $D_+(z)^{0.5}$; of the $c_{vir}(\nu)$, the evolution is larger and goes as $D_+(z)$. The amplitude of the relation is a
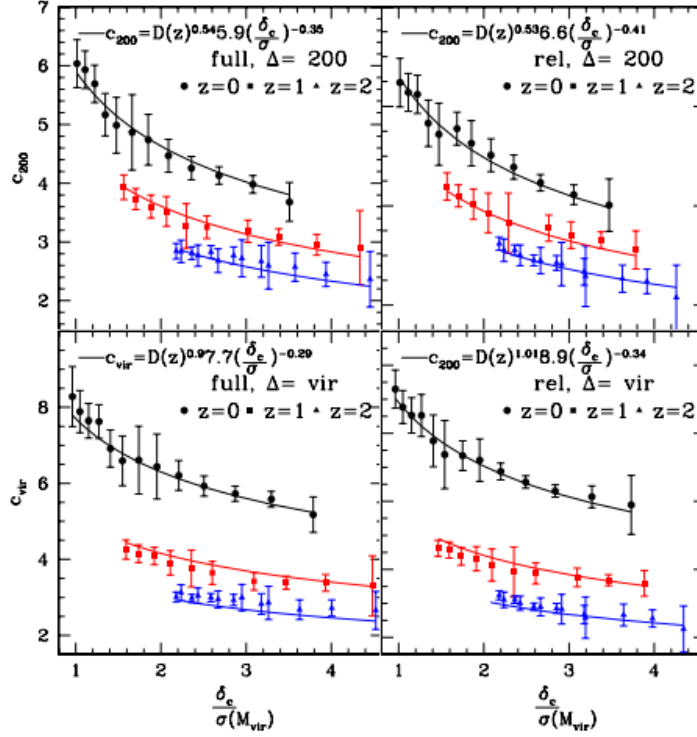
Figure 2.7: c-ν relation obtained from Bhattacharya et al. [2013]. The dots are the results of their simulation. The lines are global fits to the data point.

	$\Delta = 200$	Δ_{vir}
Full	$D_+(z)^{0.54}5.9\nu^{-0.35}$	$D_+(z)^{0.9}7.7\nu^{-0.29}$
Relaxed	$D_+(z)^{0.53}6.6\nu^{-0.41}$	$D_+(z)^{1.01}8,9\nu^{-0.34}$

Table 2.4: Fitting formula for the c-ν relation obtained from Bhattacharya et al. [2013]

little larger for the relaxed sample than for the full sample by 10%. The lines in figure 2.7 are given by the fitting formulae as derived from their simulation for the reference ΛCDM cosmology. The fitting formulae are shows in table 2.4.

They also proposed an approximate fitting formula relating ν and M which can be used to convert the relation from c-ν to c-M.

Figure 2.8: Comparison between the model (lines) and the simulation data (dashed lines) from Diemer & Kravtsov [2015]. The dashed lines show the median c-ν (left) and c-M (right) relations predicted by their model, whereas the solid lines and shaded areas show the median concentrations of simulated halos and the 68% scatter.

2.3.4   Diemer & Kravtsov [2015]

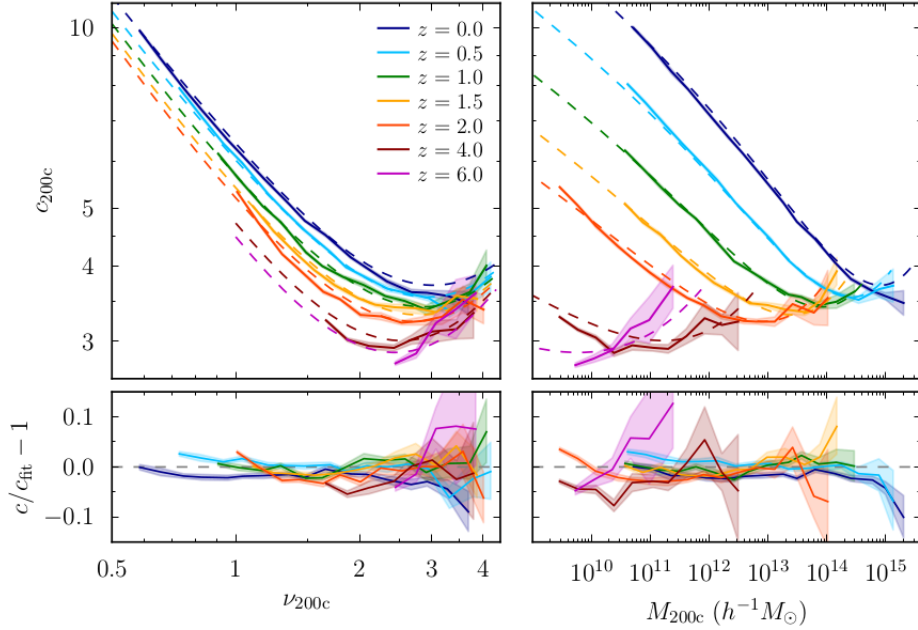Diemer & Kratov [2015] (hereafter D15) used a suite of dissipation-less ΛCDM simulations of different box size, resolution and cosmological parameters to cover a large mass range. Their fiducial cosmology was the WMAP7 cosmology. They performed several simulations with a cosmological model consistent with the constraints from Planck satellite, and other simulations based on self-similar models, where $\Omega_M = 1$, with power-law matter power spectra of different slopes. All their simulations were run using the `GADGET-2` code. They used the phase-space halo finder `ROCKSTAR` to extract all isolated halos and sub-halos. They only considered the concentration of the isolated halos, and the contribution of the sub-halos to the density profile of the same isolated halo. A halo is deemed to be isolated if its center does not lie inside r_{vir} of another halo. Only isolated halos with at least 1000 particles inside r_{200}, 200 particles inside r_s and with r_s at least six time the force softening length were accepted. They studied the concentration estimated by `ROCKSTAR`. This code finds the scale radius of halo by fitting the NFW profile, using only the particles inside r_{vir}.

	ϕ_0	ϕ_1	η_0	η_1	$-\alpha$	β
Median	6.58	1.37	6.82	1.42	-1.12	1.69
Mean	7.14	1.60	4.10	0.75	-1.40	0.67

Table 2.5: Best-fit parameters for the Diemer & Kravtsov [2015] model.

Instead of studying the concentration in function of the mass, they studied the relation with the peak height, ν. In addition, they studied the concentration at the radius r_{200} because they found, from their results, that the relation at $\Delta = 200$ is universal.

However, a residual of non-universality for the c-ν relation still persists. This suggests that there is at least one additional parameter besides the peak height that influences the concentration. For their analytic model, they proposed as additional parameter the local slope of the power spectrum, defined as:

$$n \equiv \frac{d \ln P(k)}{d \ln k}. \tag{2.26}$$

From the self-similar simulations, they found that overall c-ν relation depend strongly on n at fixed ν. To quantify this dipendence, they fitted the c-ν relation of the self-similar models with the double power-law function, written as:

$$c_{200} = \frac{c_{min}}{2} \left[\left(\frac{\nu}{\nu_{min}} \right)^{-\alpha} + \left(\frac{\nu}{\nu_{min}} \right)^{\beta} \right], \tag{2.27}$$

where the slopes α and β are fixed and the concentration floor, c_{min}, and its location, ν_{min}, are assumed to depend linearly on the power spectrum slope

$$c_{min} = \phi_0 + \phi_1 n, \tag{2.28}$$

$$\nu_{min} = \eta_0 + \eta_1 n. \tag{2.29}$$

They also fitted this model for all of their simulations. They estimated the best-fit parameters for the mean and median relation by performing a global least-square fit over the simulations for all cosmologies, masses and redshifts. These best fits are listed in table 2.5.

Figure 2.8 compares the model with the simulation data for the fiducial ΛCDM cosmology and its redshift evolution. The dashed lines show the median c-ν and c-M relations obtained from model. The solid lines and the shaded areas show the median concentrations of simulated halos and the 68% scatter. This model fits the concentration measured in the fiducial cosmology to $< 5\%$ accuracy.

2.4   Differences and similarities between models

The main differences between the models discussed above is due to the improved computational capabilities. Over the years, the technological progress has made it possible to run larger and more precise simulations. For example, the B01's simulations were run with a maximum box size of $600h^{-1}$Mpc, whereas the D15 simulations were build up with $2000h^{-1}$Mpc. The larger box size makes predictions at high masses and high redshift much more accurate, i.e., they enable us to better study the flattening of the c-M relation.

Another important difference is how the authors selected the halos, and, therefore, how they measured the concentration. In this regard, the B01, B13, and D15 models are similar because they fitted their simulations with the NFW profile and got the concentration via the fit. The P12 model selected the halos according to the V_{max}/V_{200} ratio and measured the concentration with eqs. (2.20) and (2.21).

Moreover, the B01 and B13 models showed the results for their all and relaxed sample, while P12 referred only to relaxed halo and D15 to isolated halos. All models considered the over-density $\Delta = 200$.

The B01 model proposed a model in which they related the concentration to the density at the collapse redshift, and they used the simulations to calibrate this model with one free parameter, K. The others authors proposed different formulas to fit their simulation results, and they tried to find a universal function to remove the redshift dependence, but they used different parametrization. The P12 model expressed the combined time and mass dependence in terms of σ and considered the $\Omega_{\Lambda,0}/\Omega_{m,0}$ parameter; B13 used D_+, see eq. (1.22), and ν; D15 used ν and n, see section 1.2.2.

2.5   The instrinsic scatter

A common result obtained from all numerical simulations is the spread in c values at fixed M. The intrinsic scatter in the halo concentrations has a log-normal distribution for relaxed halos, see Jing [2000].

The scatter in the c-M relation is related to several processes. E.g., the physical processes at the base of the halo assembling or to the resolution limit of the simulations. Bullock et al. [2001] described the scatter in halo concentration through two sources of scattering. The first one is the Poisson noise due to the sampling of a finite number of halos in each mass bin, especially in the case of large-mass halos. Moreover, the small halos are abundant, but the relatively small number of particles in each halo make the measurement of the M_{200} and c_{200} harder: this is the second source of the scatter. From their numerical simulations, Bullock et al. [2001] found that the scatter is roughly constant as a function of

mass with $\delta(\log_{10} c_{vir}) \sim 0.18$ for halos, and $\delta(\log_{10} c_{vir}) \sim 0.24$ for sub-halos, if they defined sub-halo when the centre of the halo is located within the virial radius of a larger "host" halo. Bullock et al. [2001] interpreted the larger scatter evaluated for sub-halos is the result of their more complicated formation histories, with more interactions and stripping.

Neto et al [2007] found that $\delta(\log_{10} c_{200}) \sim 0.14$ for the full-sample and $\delta(\log_{10} c_{200}) \sim 0.11$ for the relaxed sample. Moreover, they found a weak but systematic trend, that the scatter in the concentration decreases monotonically as a function of the mass. They interpreted this result as more massive halos being a more homogeneous population than lower massive halos. This can reflect the fact that massive halos are rare objects that have collapsed recently, whereas less massive systems have a much wider distribution of assembly redshifts.

Bhattacharya et al. [2013] found a scatter 10% higher than the results of Neto et al [2007], that is $\delta(\log_{10} c_{200}) \sim 0.16$ for the full-sample and $\delta(\log_{10} c_{vir}) \sim 0.12$ for the relaxed sample. Bhattacharya et al. [2013] explained this result in terms of differences in the fitting procedure. Bhattacharya et al. [2013] fitted the halo profile over the range $(0.1\text{-}1)r_{vir}$, while Neto et al [2007] over the range $(0.05\text{-}1)r_{vir}$.

The semi-analytic model of Zhao et al. [2009] predicted the halo concentration using the formation time $t_{0.04}$ with a scatter $\delta(\log_{10} c_{vir}) \sim 0.12$. Giocoli et al [2012] was able to reduce the scatter in the semi-analytic model of Zhao et al. [2009] to $\delta(\log_{10} c_{vir}) \sim 0.10$, adding information about the formation time $t_{0.5}$ (section 2.2.2).

In the following chapters, we have considered an intrinsic scatter of 0.11 as measured by Neto et al [2007].

3

Code and testing

In this chapter, we describe firstly the `Colossus` *tool, a Python software that we have used compute the c-M relation, and our developed code that we have used for the cosmological analysis. Subsequently, we report the several tests that we have done to assess the* `Colossus` *and code efficiency.*

3.1 Colossus tools

`Colossus` (COsmology haLO and large-Scale StrUcture toolS[1]) is a Python software developed by Diemer [2015]. `Colossus` is constituted by a collection of modules pertaining to cosmology and dark matter halos. It is able to run cosmological calculations with an emphasis on structure formation applications, e.g., the power spectrum, the variance and the correlation function. Several halo density profiles are included, like the NFW profile. `Colossus` is able to calculate the spherical overdensity halo masses, make conversions between mass definitions, e.g. the mass within the radius r_{200}, r_{500} or r_{vir}, and study the pseudo-evolution of the spherical overdensity. `Colossus` includes several models for the c-M relation.

3.2 Code developed

In this section, we describe the code developed for this Thesis, how it works and which assumptions we have done. The code is able to create a mock observation (section 3.2.1), to compare either mock or real data to several c-M relation (section 3.2.2) and to find the best value of Ω_M and σ_8 to describe the data via the χ^2 test

---

[1]http://www.benediktdiemer.com/code/
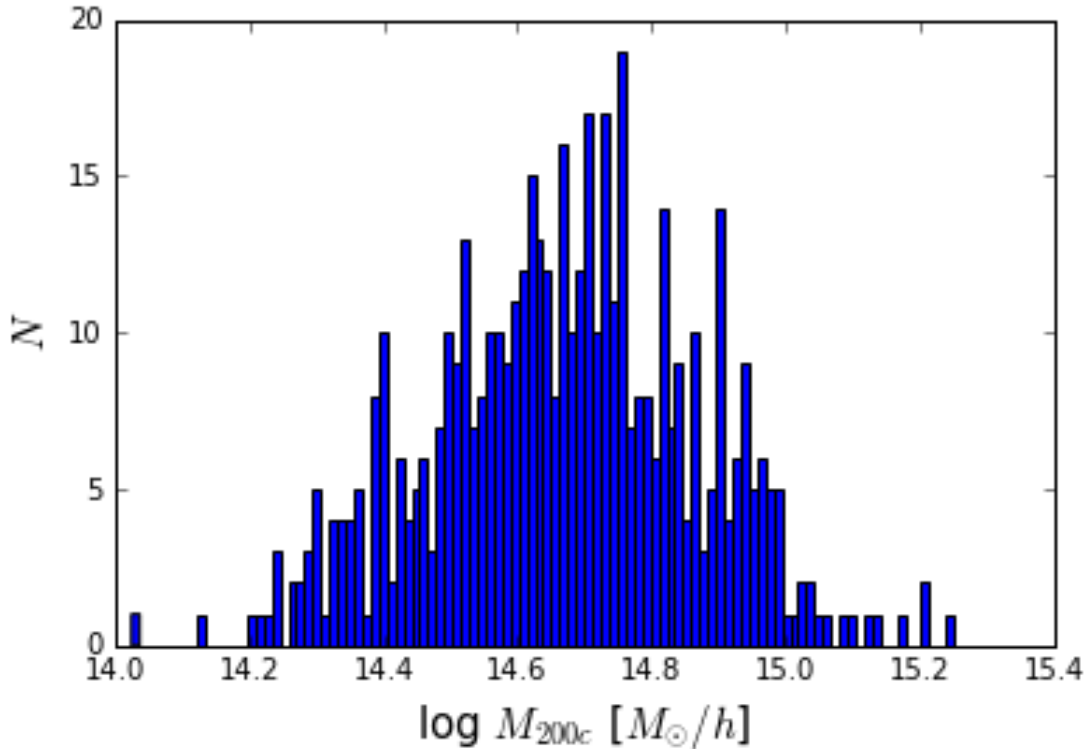
Figure 3.1: Mass distribution for a mock observation computed by the function **mass_range_gauss**. The figure indicates the number of the selected clusters for each mass bin. The distribution is realized between $10^{14}h^{-1}M_\odot$ and $2\cdot10^{15}h^{-1}M_\odot$ cluster mass and 500 objects have been extracted in this range.

(sections 3.3 and 3.3.1). In the appendix A are reported the several functions that we wrote.

3.2.1   Creating mock data

Our code is able to simulate a mock observation, via the function **generate_obs**. With this function, the code assigns a concentration value, predicted by a model, to a cluster mass value, including systematic and statistical errors.

Firstly, to create a mock data, the number of the "observed" clusters, N_{obs} and their observed redshifts, z_{obs} are set at the beginning by the user. The code assigns the same redshift to all objects. As regards the masses, M_{obs} in $h^{-1}M_\odot$ units, to create a mock data it is only necessary that the user sets the minimum and the maximum mass value. The code, via the function **mass_range_gauss**, produces a log-normal distribution, where the mean value of the distribution is the mean

of the extreme values $\log_{10}(M_{min})$ and $\log_{10}(M_{max})$ and wide 0.15 dex. The code randomly selects N_{obj} objects from this distribution.

The log-normal distribution has been chosen since the mass distribution of an observationally selected sample of galaxy clusters is limited at large and small masses. At large masses, the distribution is limited by the steepness of the mass function. Instead, at small masses, the distribution is limited by some observational thresholds that the clusters have to pass to be detected. As a result, the distribution of masses is approximately log-normal, see Sereno & Ettori [2015]. An example, a mass distribution realized by the function **mass_range_gauss** is shown in figure 3.1. In this case, M_{min} has been set to $10^{14}h^{-1}M_\odot$, $M_{max} = 2 \cdot 10^{15}h^{-1}M_\odot$ and $N_{obj} = 500$.

Using the function **generate_obs**, the code assigns an observational mass error to each cluster, $\delta M_{obs} = M_{obs} \cdot \varepsilon_M$, where ε_M is the relative error. The error is redshift dependent, $\varepsilon_M = \varepsilon_M(z)$. We will describe below how the function $\varepsilon_M(z)$ has been determined,

The final step of the function **generate_obs** is the computation of the observed concentration for each object and its error. For this reason, the code evaluates the concentration using the `Colossus` function **concentration**. To use this function, the cosmological model has to be defined, through the parameters Ω_M and σ_8, and a c-M relation has to be adopted. We will indicate as c_{model} the concentration value evaluated by `Colossus` at fixed cosmology, c-M relation, mass, and redshift. The observed concentration differs from the input concentration by two contributions. One is the intrinsic scatter, σ_{int} (see section 2.5), defined in the $\log_{10}$-space. The other one is relative "statistical" uncertainty, ε_c. The parameter ε_c indicates the relative uncertainty associated to the concentration, $\varepsilon_c = \delta c/c$. To take into account these two types of error, we have developed the code as follows:

i) the code calculates the value of $\log_{10} c_{model}$ for each M_{obs}, with the relative z_{obs}, at fixed cosmology and c-M relation model with the `Colossus` function **concentration**;

ii) the code extracts the value $\log_{10} c_{real}$ randomly from a log-normal distribution with the mean value equal to $\log_{10} c_{model}$ and standard deviation σ_{int};

iii) the code extracts the value $\log_{10} c_{obs}$ randomly from a log-normal distribution with the mean value equal to $\log_{10} c_{real}$ and standard deviation $\varepsilon_c/\ln 10$;

iv) the code calculates the observed concentration as $c_{obs} = 10^{\log_{10} c_{obs}}$[2] and its error as $\delta c_{obs} = c_{obs} \cdot \varepsilon_c$.

---

[2]This relation is exact for the median, and it approximately holds for the means of the distribution too.

Reference	z	ε_c	ε_M
Vikhlinin et al. [2006]	0.09	0.07	0.11
Ettori et a. [2010]	0.18	0.19	0.19
Amodeo et al. [2016] (z < 0.7)	0.541	0.45	0.47
Amodeo et al. [2016] (z > 0.7)	0.813	0.79	0.66

Table 3.1: Median values for z and the relative uncertainties ε_c and ε_M obtained from the papers listed in col. 1.

When a value of concentration c_{new} is randomly extracted from a log-normal distribution with a mean value c_{old} and standard deviation σ, we will indicate it as: $c_{new} = c_{old} \oplus \sigma$.

The value of σ_{int} it fixed at the value 0.11 dex (Neto et al [2007], Duffy et al. [2008]). The value of ε_c is assumed to be redshift dependent, $\varepsilon_c = \varepsilon_c(z)$, as for $\varepsilon_M(z)$. To find the redshift dependence of $\varepsilon_c(z)$ and $\varepsilon_M(z)$, we have used the data from Vikhlinin et al. [2006], Ettori et a. [2010] and Amodeo et al. [2016]. For each of these papers, we have computed the median value of ε_c and ε_M in redshift bins. These values are reported in table 3.1. The code builds the functions $\varepsilon_c(z)$ and $\varepsilon_M(z)$ as a first order interpolation between the measured points, see figure 3.2. This figure shows the functions $\varepsilon_c(z)$ and $\varepsilon_M(z)$, where the dots indicate the values computed from the papers, while the solid lines plot the interpolations.

Finally, the code writes into a text file the quantities M_{obs}, z_{obs}, c_{obs}, and their errors.

3.2.2 Expected concentrations

To probe the cosmological parameters, the code is able to compare the observed concentrations to the concentrations predicted under a given c-M relation. Since we are interested in investigating the cosmological parameters Ω_M and σ_8, their range must be set before the modelling. To set the cosmological parameter range, via the function **create_range**, the user sets the minimum and the maximum value of the parameter and the grid resolution.

The code determines the value of the c-M relation model, c_{model}, using the function **modelling_data**. For each observed object, M_{obs} and its redshift z_{obs}, this function calculates the expected concentration for a given model, c_{model}, and the relative dispersion, equal to the σ_{int} in the $\log_{10}$-space. The code calculates, at
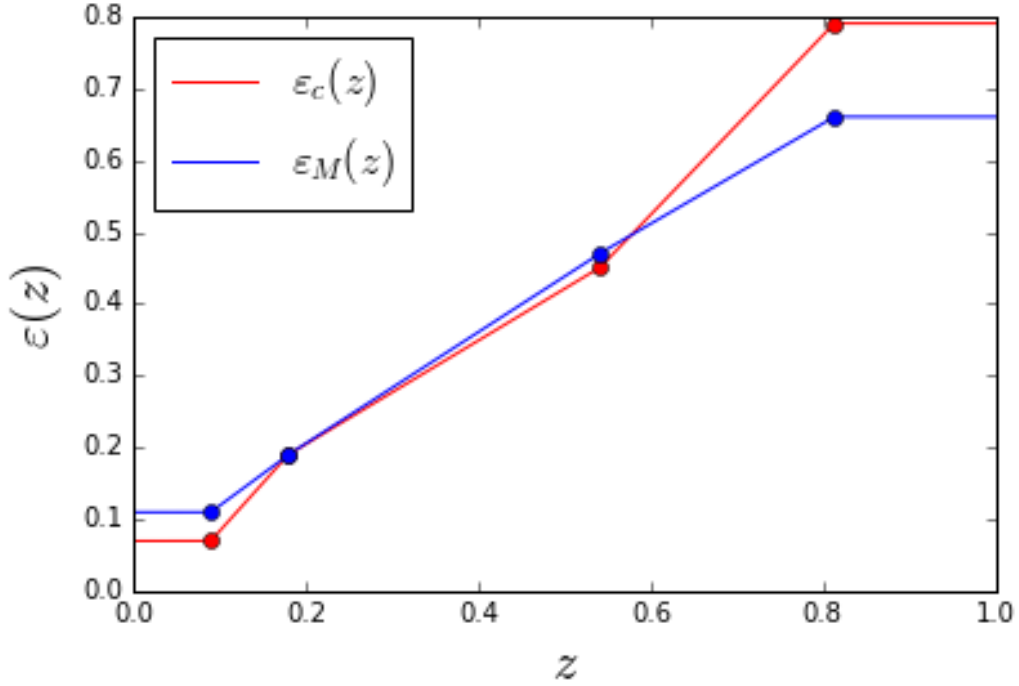
Figure 3.2: The redshift dependence of the relative errors ε_c and ε_M. The dots indicate the values listed in table 3.1. The solid lines show the functions $\varepsilon_c(z)$ and $\varepsilon_M(z)$ as detailed in section 3.2.1.

fixed mass, the c_{model} for each combination of Ω_M and σ_8. The estimated value of c_{model}, c_{model}^{ijk}, is stored in a 3-D matrix, where the index i refers to the i-th object, while j and k refer to the cosmological parameters, Ω_M and σ_8, respectively.

In the analysis, we have also considered the cosmological correction that propagates through the observed quantities. For instance, the measurement of the mass depends on the assumed cosmological parameters (Sereno & Ettori [2015b]) through the relation:

$$M^{new} = M^{old} \cdot \frac{d_A^{new}}{d_A^{old}}, \tag{3.1}$$

where M^{old} indicates the mass computed with the old cosmological parameters, d_A^{new} and d_A^{old} are the angular diameter distances to the cluster, calculated at the redshift z of the object with the new and the old cosmological parameters, respectively. The angular diameter distance is defined as follows:

$$d_A = \frac{d_{lum}}{1+z} = \frac{c}{H_0(1+z)} \frac{S(\omega)}{|\Omega_K|^{1/2}}, \tag{3.2}$$

where

$$\omega = |\Omega_K|^{1/2} \int_0^z \frac{dz'}{E(z')}, \tag{3.3}$$

d_{lum} is the luminosity distance, $S(\omega)$ is equal to $\sinh(\omega)$, ω or $\sin(\omega)$ for Ω_K greater than, equal to or less than 0, respectively. Moreover, $\Omega_M = 1 - \Omega_M - \Omega_\Lambda$ accounts the curvature of the space and $E(z)$ refers to the $(1 + z)[...]$ part of eq. (1.15). The two angular diameter distances are calculated using the `Colossus` function **angularDiameterDistance**.

3.2.3 Extrapolations in the Bullock model

For several combinations of the cosmological parameters Ω_M^* and σ_8^*, the B01 model is not able to evaluate the concentration for large mass values, M^*, at fixed redshift z^*. This is due to the fact that a cluster with mass M^*, with a cosmological model defined with the parameters Ω_M^* and σ_8^*, is not able to collapse on time into a halo at redshift z^*. Consequently, the B01 model cannot determine the concentration. To bypass this problem, we have implemented a method, via the function **correction_data**, to find the concentration value when the B01 model cannot.

Firstly, the code searches the larger value of mass $M' < M^*$ such that the B01 model, with the cosmological parameters Ω_M^* and σ_8^* and redshift z^*, is able to evaluate a concentration value. At this point, the code determines the concentration, always for the B01 model, in ten bins between $M'/2$ and M'. Since we know that the B01 model predicts a power-law relation for the c-M relation, and then a straight line in the $\log_{10}$ space, the code calculates a linear fit, for the ten points previously calculated, in the $\log_{10}$ space. Lastly, the code extrapolates the concentration value for the mass M^* through this linear fit.

Figure 3.3 shows how the **correction_data** works. For this test, we have simulated 40 objects between $10^{12} h^{-1} M_\odot$ and $10^{16} h^{-1} M_\odot$ mass values equally spaced in the $\log_{10}$-space. We have adopted a cosmology with $\Omega_M = 0.3$ and $\sigma_8 = 0.8$. With this mass range and cosmology, we have run the `Colossus` tool to calculate the concentration value expected for the B01 model. The red points in figure 3.3 are the concentration values calculated via `Colossus`. With these initial conditions, the model is not able to calculate the concentration for masses over $10^{15.4} h^{-1} M_\odot$, that is the right part of the vertical blue line. The blue points indicate the concentration value obtained with the **correction_data** function.
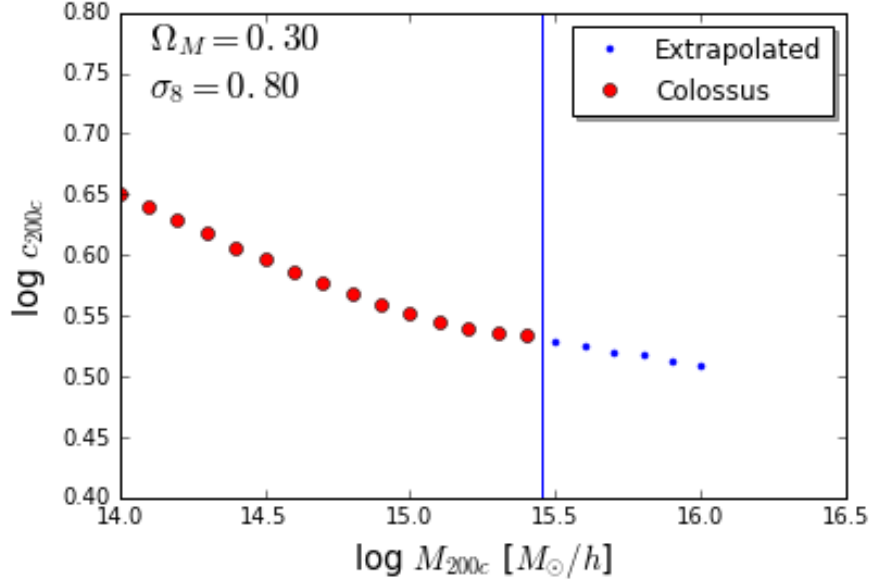
Figure 3.3: c-M relation for the B01. The red points indicate the concentration value calculated via the `Colossus` tools, while the blues points via the **correction_data** function. The vertical blue line indicates the limit at which the B01 model is able to calculate a concentration value. In figure are shown the cosmological parameters adopted for this test.

3.3 Fitting procedure

The code is able to fit the data with a model, finding the best cosmological parameters to describe the data. A number of techniques exists to fit a model to data with errors, and we have assumed the maximum likelihood approach (Weiner et al. [2006]). For a model f with parameters $\mathbf{a}$, the predicted values are $y_k = f(x_k; \mathbf{a})$. The uncertainties in x_k and y_k are given by $\varepsilon_{x,k}$ and $\varepsilon_{y,k}$. If the intrinsic scatter σ_q in the y coordinate is Gaussian, the likelihood Γ is given by

$$\Gamma = \prod_{k=1}^{N} \frac{1}{w_k \sqrt{2\pi}} \exp\left[-\frac{[y_k - f(x_k; \mathbf{a})]^2}{2w_k^2}\right], \tag{3.4}$$

where w_k indicates:

$$w_k^2 = \left[\frac{df}{dx}(x_k)\right]^2 \varepsilon_{x,k}^2 + \varepsilon_{y,k}^2 + \sigma_q^2. \tag{3.5}$$

If we consider the logarithm of the likelihood, we obtain:

$$-2\ln\Gamma = \sum_{k=1}^{N} \left[\frac{[y_k - f(x_k; a)]^2}{w_k^2} + \ln w_k^2\right]. \tag{3.6}$$

We will indicate the quantity $-2\ln\Gamma$ as χ^2.

The code sets the parameters Ω_M and σ_8 as free parameters to fit the data, and the code is able to calculate the value of the χ^2 for each combination of cosmological parameters via the function **chi_square**. We compute the χ^2 in a grid as $\chi^2_{i,j}$, where i and j indicates the i-th and the j-th value of Ω_M and σ_8, respectively. As in equation (3.6), the code calculates the value of $\chi^2_{i,j}$ as follows:

$$\chi^2_{i,j} = \sum_{k=1}^{N_{obs}} \left[\frac{[\log_{10} c_{obs,k}(M_k, z_k) - \log_{10} c_{model,ijk}(M_k, z_k)]^2}{\sigma^2_{ijk}} + \ln(\sigma^2_{ijk}) \right] + 2\ln\sqrt{2\pi},$$
(3.7)

where the sum is done over the N_{obs} objects of the sample; σ^2_{ijk} accounts for the scatters and it is implemented as follows:

$$\sigma^2_{ijk} = (\delta\log_{10} c_{obs,k}(M_k, z_k))^2 + (\delta\log_{10} c_{model,ijk}(M_k, z_k))^2 + B^2(\delta\log_{10} M_{obs,k})^2,$$
(3.8)

where $c_{obs,k}(M_k, z_k)$ indicates the concentration measured for the object k with mass M_k and redshift z_k, $c_{model,ijk}(M_k, z_k)$ is the expected concentration for the model $model$, at the M_k and z_k, for the cosmological parameters $\Omega_{M,i}$ and $\sigma_{8,j}$, $B = \Delta\log_{10} c/\Delta\log_{10} M$ is the local slope of the c-M relation between $M_{obs,k} + \delta M_{obs,k}$ and $M_{obs,k} - \delta M_{obs,k}$.

3.3.1   Best parameters

We have implemented two methods to find the best-fit parameters and the statistical uncertainties.

Method 1: the first method uses the function **find_parameter _error**. This function determines the best-fit parameters finding the minimum of the $\chi^2_{i,j;min}$. The best-fit cosmological parameters are computed at the grid position of the minimum. To determinate the errors associated to the two cosmological parameters from the two-dimensional χ^2, the code finds the parameters at which $\chi^2_{i,j,err} = \chi^2_{i,j,min} + 2.3$ and these parameters will be the superior and inferior uncertainty limit. The quantity $\Delta\chi^2 = 2.3$ indicates the confidence level of the 68.3% with two degrees of freedom

Method 2: the second method uses the functions **probability _density_fuction** and **best_parameter_from_probability**. The code builds the probability density function of the single parameters, $P(\Omega_M)$ and $P(\sigma_8)$. Firstly, the code converts the values of $\chi^2_{i,j}$ in probability values $P_{i,j}$ as $P_{i,j} \propto e^{-\chi^2/2}$. Successively, the code calculates the $P(\Omega_M)$ and $P(\sigma_8)$ by marginalizing $P_{i,j}$, that is $P(\Omega_{M,i}) = \sum_j P_{i,j}$ and $P(\sigma_{8,j}) = \sum_i P_{i,j}$. Finally, the two distributions $P(\Omega_M)$ and $P(\sigma_8)$ are normalized as $P^{norm} = P/\int Pdx$, so that $\int_{-\infty}^{+\infty} P^{norm}dx = 1.0$. P is integrated numerically with the Simpson's rule.

The Simpson's rule calculates the integral of a function f in the interval $[a, b]$ with a quadratic approximation in a sub-interval $[x_i, x_{i+1}]$, and the integral becomes:

$$\int_a^b f(x)dx \simeq \frac{\Delta x}{3h} \left[f(a) + 4 \sum_{\substack{i=1 \\ i=odd}}^{n-1} f(x_i) + 2 \sum_{\substack{i=2 \\ i=even}}^{n-2} f(x_i) + f(b) \right], \qquad (3.9)$$

where $h = b - a$ and $\Delta x = x_{i+1} - x_i = (b - a)/n$.

The function **best_parameter_from_probability** finds the best-fit parameters in the standard way, calculating the mean ($\overline{\Omega}_M$ and $\overline{\sigma}_8$) and the variance ($\sigma^2_{\Omega_M}$ and $\sigma^2_{\sigma_8}$) weighted by their probability density function. These quantities are calculated as follows:

$$\overline{\Omega}_M = \frac{\sum_i P(\Omega_{M,i}) \cdot \Omega_{M,i}}{\sum_i P(\Omega_{M,i})} \qquad\qquad \overline{\sigma}_8 = \frac{\sum_j P(\sigma_{8,j}) \cdot \sigma_{8,j}}{\sum_j P(\sigma_{8,j})}, \qquad (3.10)$$

$$\sigma^2_{\Omega_M} = \frac{\sum_i P(\Omega_{M,i}) \cdot (\Omega_{M,i} - \overline{\Omega}_M)^2}{\sum_i P(\Omega_{M,i})} \qquad \sigma^2_{\sigma_8} = \frac{\sum_j P(\sigma_{8,j}) \cdot (\sigma_{8,j} - \overline{\sigma}_8)^2}{\sum_j P(\sigma_{8,j})}. \qquad (3.11)$$

We wont to point out that the only results of method 1 are the best-fit parameters; the values of the method 2 are the mean parameters.

3.4 Performance testing

To verify the `Colossus` performances and the efficiency of our code, we have performed several tests, that we describe below.

3.4.1 Colossus

We have tested the `Colossus` tools by reproducing the c-M relations expected for the several models. To carry out these tests, we have proceeded as follows: firstly, we have retrieved the relations from the papers through the WebPlotDigitizer tool[3]. This online tool is able to automatically mark, or manually mark by the user, a pattern in an image and extract the data to rebuild the pattern itself. With this online tool, we could reproduce the c-M relation of interest. Subsequently, for each paper, we have identified which cosmological model was used by the authors to plot their relations. Finally, we have tried to reproduce the data through the `Colossus` tool, in the same mass range, redshift and cosmological model.
The figures 3.4 and 3.5 show the results. For the models D15, B13 and P12 we were

---

[3]http://arohatgi.info/WebPlotDigitizer/
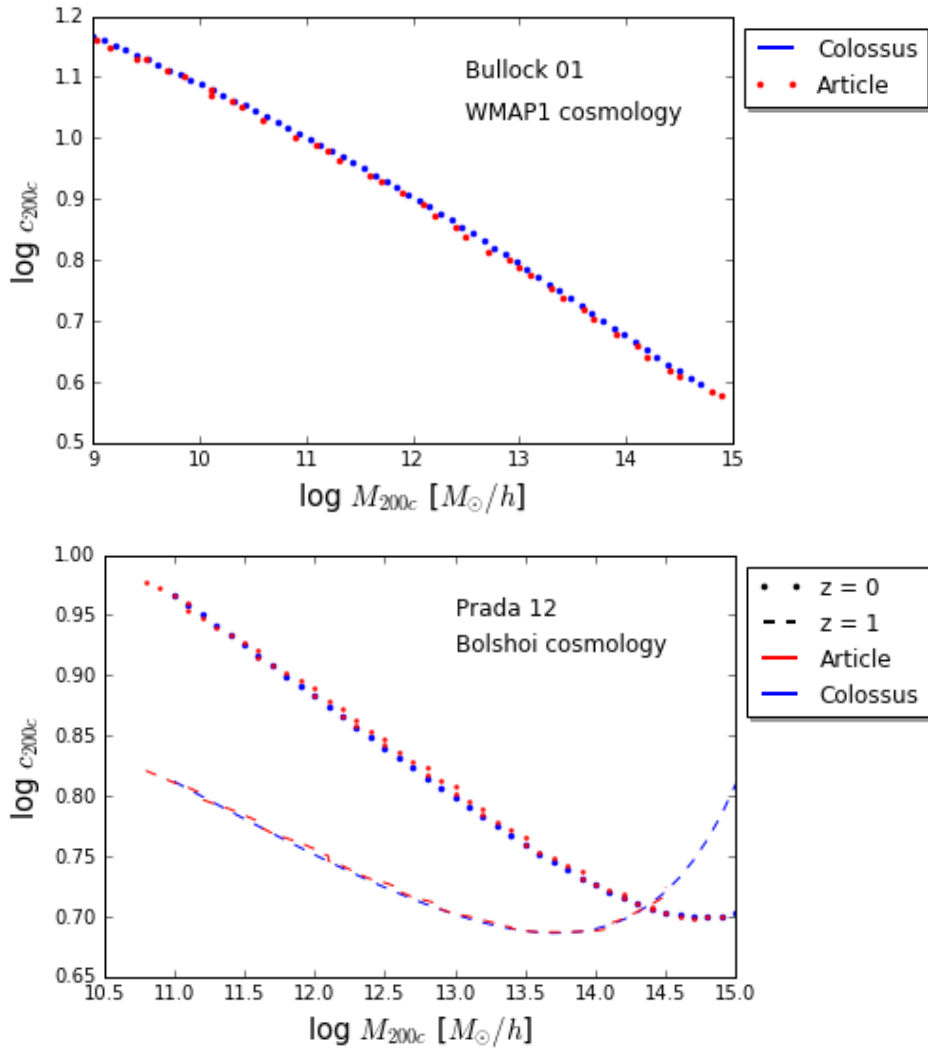
Figure 3.4: Comparison between the c-M relations shown in the original papers (red lines) and the same relations calculated with the `Colossus` tool (blue lines). The upper figure shows the results for the B01 model with WMAP1 cosmology, while the lower figure show the results for the P12 model with Bolshoi cosmology. The solid lines indicate the results at $z = 0.0$, while the dashed line at $z = 1.0$. For the B01 model, only data at $z = 0.0$ were available.

able to recover data both at $z = 0.0$ and $z = 1.0$, whereas, for the B01 model, the data came from $z = 0.0$. The models P12 and D15 use the Bolshoi cosmological model, whereas B13 and B01 use the WMAP7 and WMAP1 cosmological model, respectively. We point out that B13 is the only one that it does not show the c-M relation, but the c-ν relation. For this reason, we reproduced the c-ν relation. All
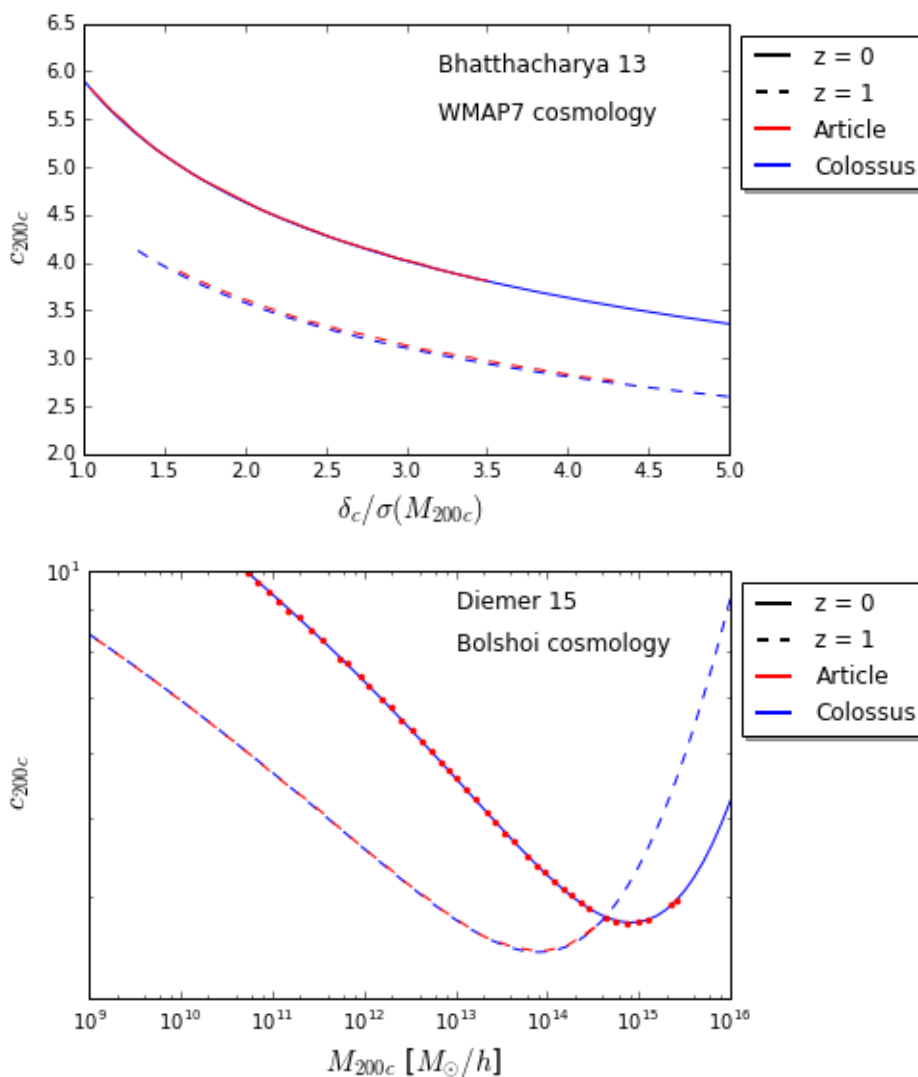
Figure 3.5:   As described in fig. 3.4 but for the B13 model with the WMAP7 cosmology, upper panel, and for the D15 model with Bolshoi cosmology, bottom panel.

the quantities, c, M and ν, are referred to the r_{200} radius.

As we can see, the data from the `Colossus` tools reproduce exactly the data for all models. `Colossus` is able to reproduce the theoretical models proposed and then we can use this tool to calculate the concentration expected for different cosmological models and redshift and mass values.

Number test	Concentration to fit	σ_{int}	ε_c	ε_M
0	c_{model}	$\sigma_{int} \cdot 0.1$	$\varepsilon_c(z) \cdot 0.1$	$\varepsilon_M(z) \cdot 0.1$
1	c_{model}	$\sigma_{int} \cdot 0.1$	$\varepsilon_c(z) \cdot 0.1$	$\varepsilon_M(z)$
2	c_{model}	$\sigma_{int} \cdot 0.1$	$\varepsilon_c(z)$	$\varepsilon_M(z)$
3	c_{model}	σ_{int}	$\varepsilon_c(z) \cdot 0.1$	$\varepsilon_M(z)$
4	c_{model}	σ_{int}	$\varepsilon_c(z)$	$\varepsilon_M(z)$
5	$c_{obs} = c_{model} \oplus \varepsilon_c$	$\sigma_{int} \cdot 0.1$	$\varepsilon_c(z)$	$\varepsilon_M(z)$
6	$c_{real} = c_{model} \oplus \sigma_{int}$	σ_{int}	$\varepsilon_c(z) \cdot 0.1$	$\varepsilon_M(z)$
7	$c_{obs} = [c_{model} \oplus \sigma_{int}] \oplus \varepsilon_c$	σ_{int}	$\varepsilon_c(z)$	$\varepsilon_M(z)$
8	$c_{obs} = [c_{model} \oplus \sigma_{int}] \oplus \varepsilon_c$	$\sigma_{int} \cdot h$	$\varepsilon_c(z) \cdot h$	$\varepsilon_M(z) \cdot h$

Table 3.2: Values of σ_{int}, ε_c and ε_M used to create the mock data and which concentration value has been used during the fit. The functions $\varepsilon_c(z)$ and $\varepsilon_M(z)$ have been obtained as described in section 3.2.1. The parameter σ_{int} is equal to 0.11 (Duffy et al. [2008]). The value 0.1, in table, has been used to test the code with a very small values of σ_{int}, ε_c and ε_M. The parameter h is equal to $0.8, 0.6, 0.4, 0.2$.

3.4.2 Our code

The goal of the following tests is to understand the efficiency of the code and whether it can recover from the mocks, realized with a fixed c-M relation model, the same c-M relation model. For this reason, we have simulated several observations and we have used the code to fit them, looking for the best values of Ω_M and σ_8 that describe the same data. We have investigated the cosmological parameters in the range $\Omega_M \in [0.10, 0.90]$ and $\sigma_8 \in [0.5, 1.5]$. We have created several mocks varying the values of σ_{int}, ε_c, ε_M, the c-M relation and concentration values to fit (c_{model}, c_{real}, or c_{obs}). The number of objects, the mass range and the cosmological model used to create the data are the same for all the simulations. In particular, we have set $N_{obs} = 250$, the masses span the range between $M_{min} = 10^{14}\text{h}^{-1}\text{M}_\odot$ and $M_{max} = 2 \cdot 10^{15}\text{h}^{-1}\text{M}_\odot$ and the Planck 2015 cosmological model is used. The data have been simulated at redshift 0.0 and 1.0.

A summary of the simulations is given in table 3.2. In this table, the values of σ_{int}, ε_c, ε_M and which concentration has been fitted are listed. The parameter c_{model} indicates the value of concentration calculated by the `Colossus` tools, and
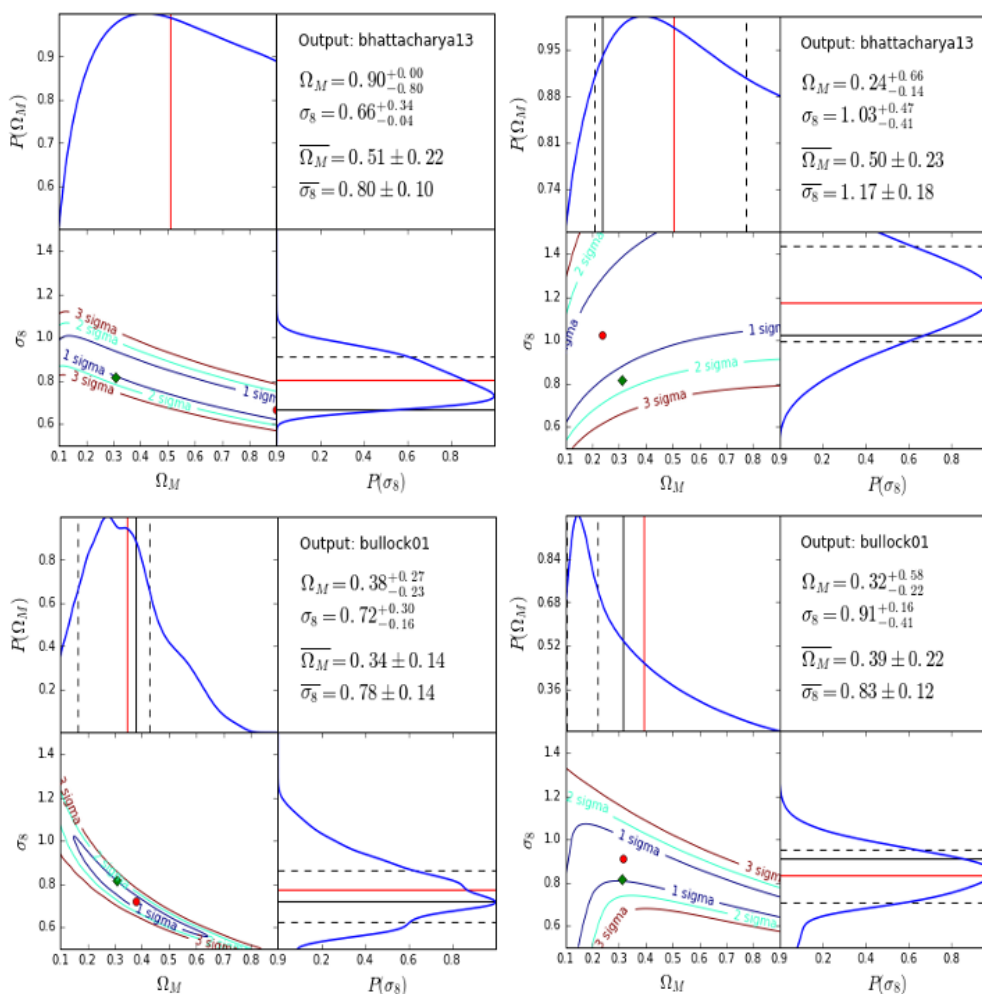
Figure 3.6: Results for the 7 test (see table 3.2). *Bottom-left panel*: the χ^2 distribution in the parameter space, with the contours at 1,2 and 3-σ in 2-D. The green dot indicates the combination of cosmological parameters at which χ^2 is minimum, while the red dot indicates the input Planck15 cosmology. *The upper-left and bottom-right*: the probability distribution functions for the single parameter. *Upper-right panel*: the first two lines report the best-fit values calculated with method 1, while the other two values are the mean values as calculated with method 2 (see section 3.3.1). The left-figures indicate the results at $z = 0.0$, whereas the right-figures at $z = 1.0$. The input c-M relation is reported in the top-left panel.

the formulas such as $c \oplus \sigma$ indicate the procedure explained in section 3.2.1. The parameters $\varepsilon_c(z)$ and $\varepsilon_M(z)$ are the relative errors on the concentration and mass,
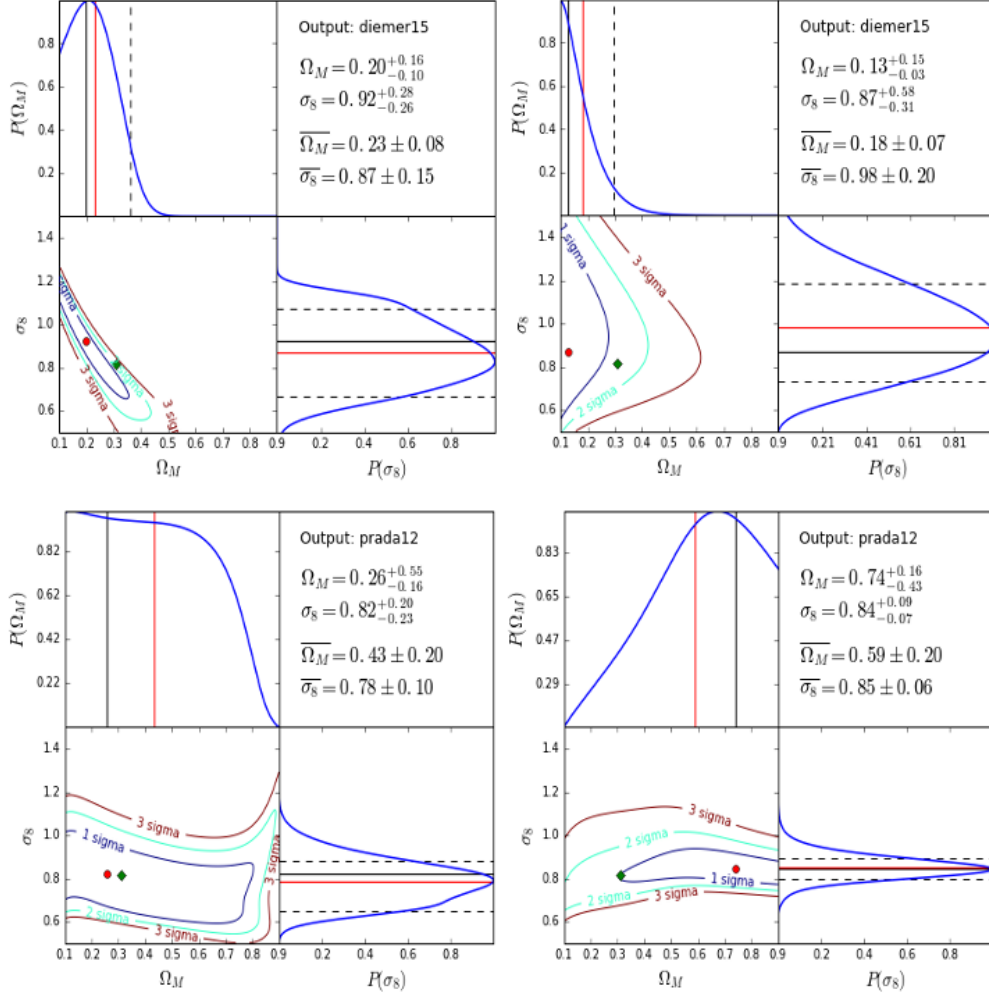
Figure 3.7: As described in figure 3.6. The upper figures are referred to the D15 model, while the bottom figures to the P12 model.

respectively, see section 3.2.1. The value 0.1 in table has been used to test the code with the very small values of σ_{int}, ε_c and ε_M. The parameter h is equal to $0.8, 0.6, 0.4, 0.2$. For this reason, the simulation number 8 have been run four times. These last simulations have been used to better understand the differences between models, see section 3.4.3.

In figures 3.6 and 3.7, we show the results of the simulation number 7. The figures are arranged as follows: For each image, the bottom-left panel shows the χ^2 distribution in the parameter space. The red dot indicates the best-fit values, i.e. the combination of the Ω_M and σ_8 at which χ^2 is minimum, while the green dot indicates the input cosmological parameters. The lines corresponding to the 2-D χ^2
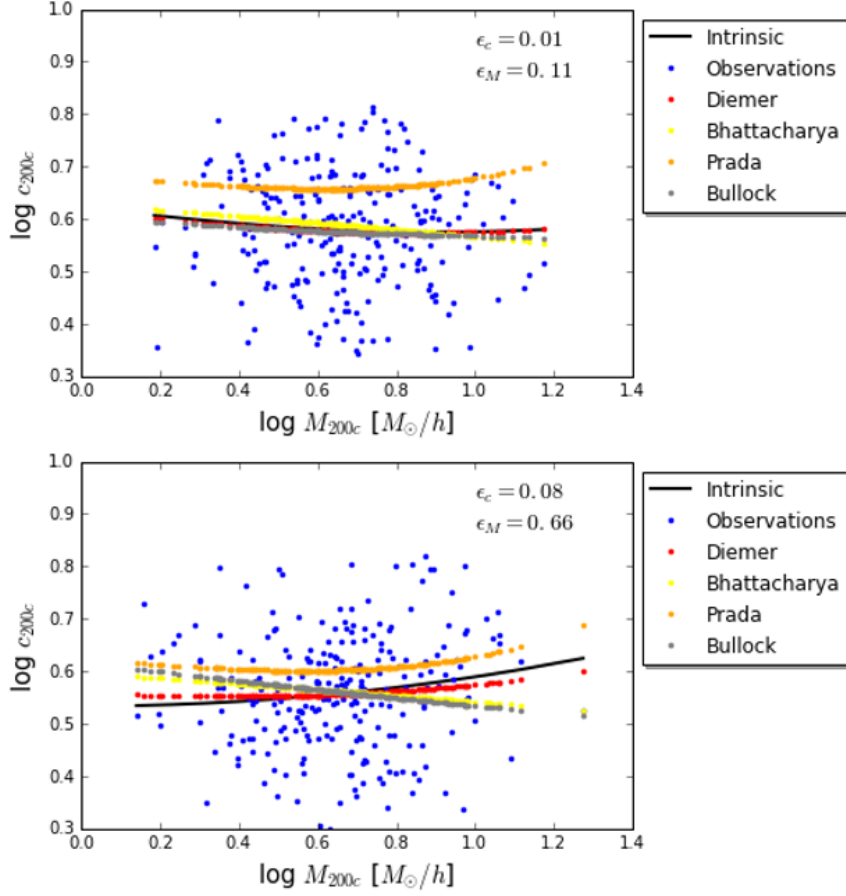
Figure 3.8: c-M relations obtained from the 6 test. The black line shows the input relation with the Planck15 cosmology and the D15 model. The blue points indicate the mock observation (section 3.2.1). The red, yellow, orange and grey dots indicate the D15, B13, P12 and B01 c-M relation models, respectively, with the cosmological parameters at which the χ^2 is minimum (see tables 1.4, 1.5, 1.6 and 1.7). The upper panel is for $z = 0.0$, whereas the bottom panel for $z = 1.0$.

distribution at 1,2 and 3-σ ($\Delta\chi^2 = \chi^2 - \chi^2_{min} = 2.3, 6.17, 11.8$, respectively). The bottom-right and upper-left panels show the probability distribution function for the σ_8 and Ω_M cosmological parameters, respectively. For clarity, the probability distribution functions are here normalized in correspondence of the maximum of the functions itself; the solid black line indicates the value of the cosmological parameter at which the χ^2 is minimum, the dashed black lines indicate the regions
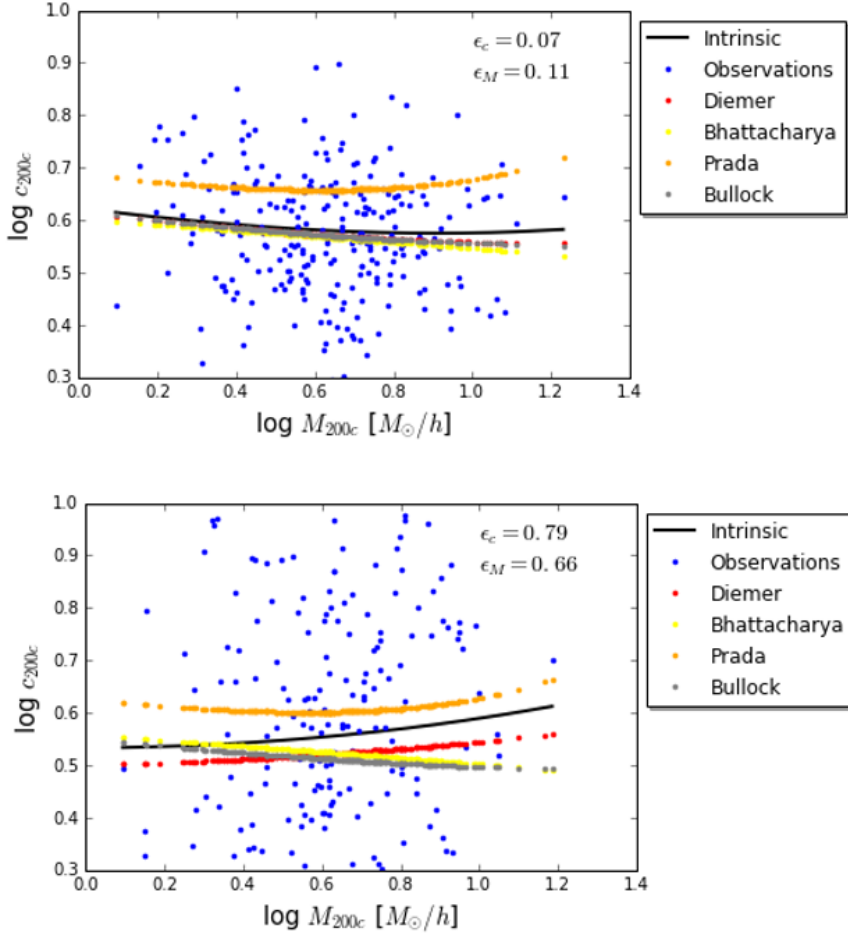
Figure 3.9: As in figure 3.8 but for the test number 7.

at which the $\Delta\chi^2_{reduced} = 1.0$, where the $\chi^2_{reduced}$ is calculated from the probability distribution function, $\chi^2_{reduced} = -2 * \ln P$. The red line indicates the mean value for the cosmological parameter calculated via method 2 (see section 3.3.1). We report in the upper-right panel of the figures 3.6 and 3.7 the parameter estimations. The first two values are referred to the first method where the error are referred to the 2-D χ^2 distribution (i.e. $\Delta\chi^2 = 2.3$ because we have two degrees of freedom), while the second two values are referred to the second method. Moreover, for each figure, the two left images correspond to redshift $z = 0.0$, whereas the two right images are for $z = 1.0$. The upper images in figure 3.6 are referred to the B13 model, while the bottom images to the B01 model. In figure 3.7, the upper images are referred to the D15 model, while the bottom images are referred to the P12
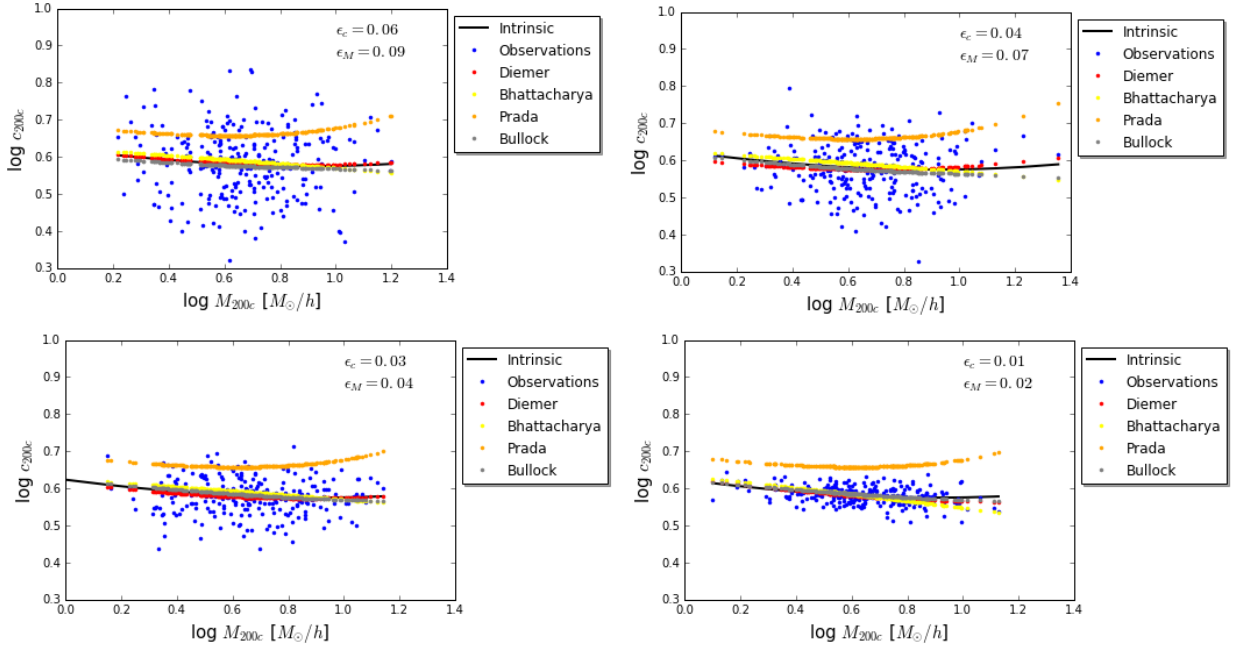
Figure 3.10: As in figure 3.8 but for the tests number 8. The upper-left panel shows the result with $h = 0.8$, upper-right figure for $h = 0.6$, bottom-left for $h = 0.4$ and bottom-right for $h = 0.2$. These figures refer to $z = 0.0$.

model.

Based on the results reported in figures 3.6 and 3.7 we can conclude that the code is able to recover the input cosmological parameters. At $z = 0.0$, the code finds the Planck15 cosmological parameters within 1-σ with both methods. At $z = 1.0$, the Planck15 cosmological parameters are found within 1 or 2-σ.

3.4.3 Comparison between models

In this section, we discuss how well could recover the c-M relations for the 6,7 and 8 tests (see table 3.2). We have used the best-fit parameters found with method 1 for reproduce the c-M relation expected for the several models. We have used the same initial characteristics to create the mock data as in section 3.4.2, but we have used only D15 as the c-M relation. We fitted these mock data with all four c-M models.

The figures 3.8 and 3.9 show the result for the 6 and 7 test, respectively, while the figures 3.10 and 3.11 show the results for the 8 test at $z = 0.0$ and $z = 1.0$, respectively. The black lines indicate the intrinsic concentration value at fixed mass,
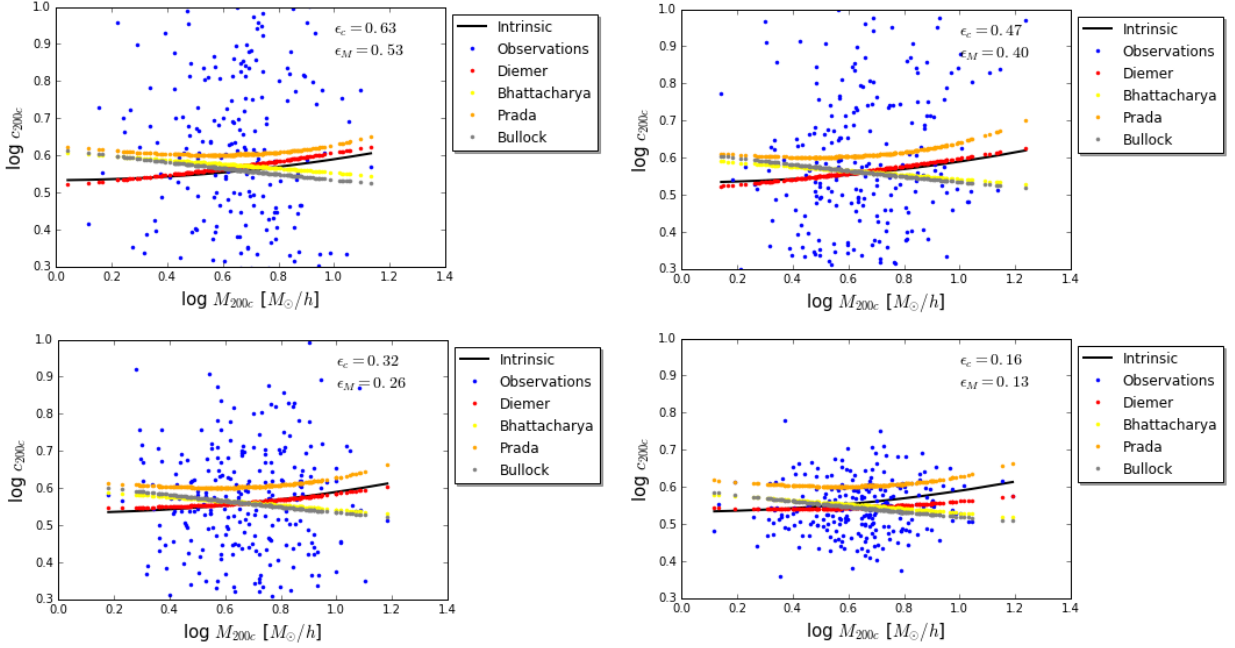
Figure 3.11: As in figure 3.10 but for $z = 1.0$.

i.e. the value calculated from the `Colossus` tools with the Planck15 cosmology and the D15 c-M relation. The blue points indicate the scattered concentration values used for the fit (see section 3.2.1). The red, yellow, orange and grey lines indicate the concentration values for the D15, B13, P12, B01 models, respectively. The models are built up with the cosmological parameters Ω_M and σ_8 at which the χ^2 is minimum. The values of these cosmological parameters are listed in tables 1.4 and 1.5 for the parameter Ω_M at redshift $z = 0.0, 1.0$, respectively, and in tables 1.6 and 1.7 for the parameter σ_8 at redshift $z = 0.0, 1.0$, respectively. In figures 3.8 and 3.9, the upper panels shows the results for $z = 0.0$, while the bottom panel for $z = 1.0$. In figures 3.10 and 3.11, the upper-left panel shows the results for the 8 test with $h = 0.8$, the upper-right panel with $h = 0.6$, bottom-left panel with $h = 0.4$ and bottom-right with $h = 0.2$.

The code is able to find a combination of cosmological parameters at which the c-M relation expected is very close to the intrinsic relation at $z = 0.0$. At $z = 1.0$, the relations found are not so close as in the other case, due to the fact that ε_c and ε_M are much larger.

From the several values in tables, 3.3, 3.4, 3.5 and 3.6, we see that the cosmological parameters found by the code, at which the χ^2 is minimum, are very different from the input cosmological parameters. The cosmological parameters

Ω_M, $z = 0.0$		Models			
$\Omega_{M,Planck15} = 0.31$		**D15**	B13	P12	B01
Number test	6	$\mathbf{0.26^{+0.17}_{-0.16}}$	$0.10^{+0.22}_{-0.00}$	$0.90^{+0.00}_{-0.00}$	$0.10^{+0.16}_{-0.00}$
	7	$\mathbf{0.20^{+0.16}_{-0.00}}$	$0.10^{+0.43}_{-0.00}$	$0.90^{+0.00}_{-0.00}$	$0.17^{+0.21}_{-0.07}$
	8 with h=0.8	$\mathbf{0.30^{+0.14}_{-0.20}}$	$0.10^{+0.11}_{-0.00}$	$0.90^{+0.00}_{-0.00}$	$0.10^{+0.08}_{-0.00}$
	8 with h=0.6	$\mathbf{0.31^{+0.09}_{-0.11}}$	$0.10^{+0.04}_{-0.00}$	$0.90^{+0.00}_{-0.00}$	$0.13^{+0.04}_{-0.03}$
	8 with h=0.4	$\mathbf{0.30^{+0.07}_{-0.07}}$	$0.10^{+0.01}_{-0.00}$	$0.90^{+0.00}_{-0.00}$	$0.17^{+0.02}_{-0.07}$
	8 with h=0.2	$\mathbf{0.24^{+0.05}_{-0.06}}$	$0.10^{+0.01}_{-0.00}$	$0.90^{+0.00}_{-0.00}$	$0.13^{+0.00}_{-0.03}$

Table 3.3: Recovered values of the Ω_M cosmological parameter at $z = 0.0$ found by the code (see section 3.3.1) via method 1. The errors refer to the two-dimensional χ^2.

Ω_M, $z = 1.0$		Models			
$\Omega_{M,Planck15} = 0.31$		**D15**	B13	P12	B01
Number test	6	$\mathbf{0.28^{+0.07}_{-0.08}}$	$0.10^{+0.05}_{-0.00}$	$0.90^{+0.00}_{-0.01}$	$0.10^{+0.02}_{-0.00}$
	7	$\mathbf{0.13^{+0.15}_{-0.03}}$	$0.10^{+0.80}_{-0.00}$	$0.90^{+0.00}_{-0.06}$	$0.10^{+0.21}_{-0.00}$
	8 with h=0.8	$\mathbf{0.20^{+0.34}_{-0.10}}$	$0.10^{+0.10}_{-0.00}$	$0.90^{+0.08}_{-0.00}$	$0.10^{+0.10}_{-0.00}$
	8 with h=0.6	$\mathbf{0.18^{+0.20}_{-0.08}}$	$0.10^{+0.07}_{-0.00}$	$0.90^{+0.00}_{-0.04}$	$0.10^{+0.03}_{-0.00}$
	8 with h=0.4	$\mathbf{0.30^{+0.09}_{-0.20}}$	$0.10^{+0.7}_{-0.00}$	$0.90^{+0.00}_{-0.02}$	$0.10^{+0.04}_{-0.00}$
	8 with h=0.2	$\mathbf{0.22^{+0.03}_{-0.10}}$	$0.10^{+0.02}_{-0.00}$	$0.90^{+0.00}_{-0.00}$	$0.10^{+0.01}_{-0.00}$

Table 3.4: As in table 3.3 but for $z = 1.0$.

are recovered within 1,2-σ distribution at $z = 0.0$ and within 3-σ distribution at $z = 1.0$.

These results suggest that the choice of the c-M relation used to fit the data is crucial to recover the cosmological parameters. These results can be seen also in figure 3.12. This figure shows the different c-M relations predicted for the several models at fixed cosmology, that is $\Omega_M = 0.3$ and $\sigma_8 = 0.8$, between $10^{14}h^{-1}M_\odot$ and $2 \cdot 10^{15}h^{-1}M_\odot$, at $z = 0.0$, solid lines, and $z = 1.0$, dashed lines.

For the P12 model, the problem is slightly different. The cosmological parameters found by this model are very different from the input cosmological parameters

σ_8, $z = 0.0$		Models			
$\sigma_{8,Planck15} = 0.89$		**D15**	B13	P12	B01
Number test	6	**$0.85^{+0.40}_{-0.25}$**	$0.66^{+0.05}_{-0.06}$	$0.75^{+0.04}_{-0.04}$	$1.14^{+0.08}_{-0.31}$
	7	**$0.92^{+0.28}_{-0.26}$**	$0.62^{+0.05}_{-0.12}$	$0.73^{+0.04}_{-0.04}$	$0.91^{+0.24}_{-0.22}$
	8 with h=0.8	**$0.79^{+0.43}_{-0.19}$**	$0.67^{+0.04}_{-0.04}$	$0.75^{+0.04}_{-0.04}$	$1.14^{+0.06}_{-0.21}$
	8 with h=0.6	**$0.74^{+0.20}_{-0.13}$**	$0.65^{+0.03}_{-0.03}$	$0.74^{+0.03}_{-0.03}$	$1.04^{+0.12}_{-0.11}$
	8 with h=0.4	**$0.76^{+0.12}_{-0.11}$**	$0.65^{+0.02}_{-0.02}$	$0.74^{+0.02}_{-0.02}$	$0.95^{+0.22}_{-0.04}$
	8 with h=0.2	**$0.88^{+0.11}_{-0.08}$**	$0.66^{+0.01}_{-0.01}$	$0.73^{+0.11}_{-0.01}$	$1.06^{+0.09}_{-0.01}$

Table 3.5: As in table 3.3 but for σ_8 at $z = 0.0$.

σ_8, $z = 1.0$		Models			
$\sigma_{8,Planck15} = 0.80$		**D15**	B13	P12	B01
Number test	6	**$0.97^{+0.24}_{-0.23}$**	$1.27^{+0.22}_{-0.09}$	$1.50^{+0.00}_{-0.05}$	$1.47^{+0.03}_{-0.06}$
	7	**$0.87^{+0.58}_{-0.31}$**	$0.99^{+0.51}_{-0.20}$	$1.50^{+0.00}_{-0.16}$	$1.24^{+0.21}_{-0.37}$
	8 with h=0.8	**$0.64^{+0.51}_{-0.14}$**	$1.35^{+0.15}_{-0.22}$	$1.47^{+0.03}_{-0.23}$	$1.50^{+0.00}_{-0.16}$
	8 with h=0.6	**$0.64^{+0.24}_{-0.14}$**	$1.28^{+0.22}_{-0.16}$	$1.43^{+0.07}_{-0.15}$	$1.46^{+0.04}_{-0.12}$
	8 with h=0.4	**$0.93^{+0.38}_{-0.42}$**	$1.30^{+0.20}_{-0.11}$	$1.50^{+0.00}_{-0.06}$	$1.50^{+0.00}_{-0.08}$
	8 with h=0.2	**$0.97^{+0.20}_{-0.32}$**	$1.17^{+0.11}_{-0.05}$	$1.50^{+0.00}_{-0.02}$	$1.40^{+0.04}_{-0.04}$

Table 3.6: As in table 3.5 but at $z = 1.0$

and the relation found is very different from the input one. The P12 model predicts relations always above the input one.

This result depends on how the P12 model is built up. The P12 modelling has been already discussed in the literature (see e.g. Bhattacharya et al. [2013] and Diemer & Kravtsov [2015]). In particular, Meneghetti & Rasia [2013] demonstrated that there are two principal effects that can explain the discrepancy between P12 and the other models. Firstly, they demonstrated that the if the c-M relation is constructed using halos binned by their maximum circular velocity, as in P12, higher concentrations are expected on the same mass scale than for mass selected halos, independently of the method used to measure the halo concentrations. The halo selection can change the concentration measured by about 15-20%
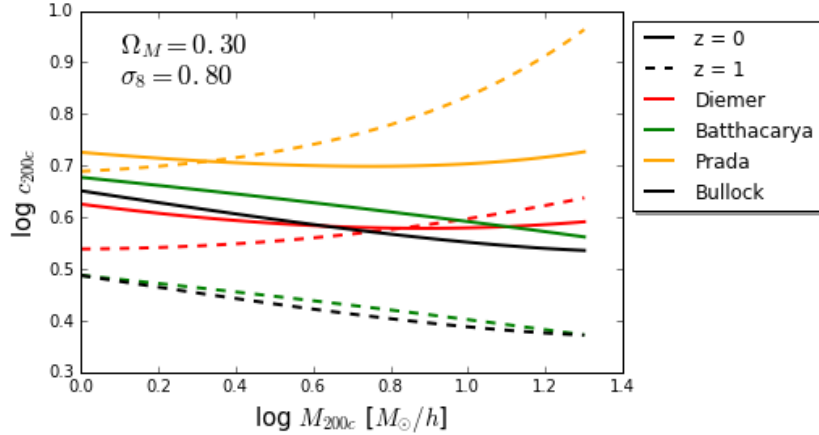
Figure 3.12: The c-M relations predicted by different models at a fixed cosmology, with $\Omega_M = 0.3$ and $\sigma_8 = 0.8$. The solid lines refer to $z = 0.0$, while the dashed lines to $z = 1.0$.

and it is mass dependent; higher masses are more affected by the binning method. This fact is also in part responsible for the upturn observed in the P12 model. Secondarily, there are differences between the concentration obtained by fitting the halo density profile with NFW and the concentration derived with the V-ratio. These two methods can give the same results if the NFW fit is performed over the radial range $r_{max} \leq r \leq r_{200}$ (r_{max} is the radius at which the circular velocity is maximum), which corresponds to the scales where the V-ratio is evaluated. Moreover, the agreement between the concentration measurements is good only for the halos with the smallest best-fit χ^2, and this χ^2 increases with the halo mass. More massive halos can show a poor fit because they are far from equilibrium, and this can exacerbate the upturn of the c-M relation in the P12 model. Meneghetti & Rasia [2013] demonstrated that the method to measure the concentration using the V-ratio, as in P12, impacts for another 20% more on the amplitude of the c-M relation for halos at $z \sim 0.25$.

4

Cosmological constraints from X-ray data

We have used our code to get the cosmological constraints from X-ray data. In this chapter, we give a brief presentation of the high-redshift Chandra data sample of Amodeo et al. [2016]. We give a brief presentation of their data reduction and the several assumptions that they have done. We present the cosmological constraints that we have obtained with this sample. Moreover, we present how the cosmological constraints change by adding the low-redshift $XMM - Newton$ cluster sample of Ettori et al. [2010]. Finally, we compare our results with previous works.

4.1   The Amodeo et al. [2016] cluster sample

Amodeo et al. [2016] (A16 hereafter) selected 47 galaxy clusters spanning a redshift range $0.4 < z < 1.2$, with an exposure time larger than 20ks from the *Chandra* public archive. They adopted the NFW as a functional form of the cluster gravitational profile and a flat ΛCDM cosmology with $\Omega_M = 0.3$ and $\Omega_\Lambda = 0.7$.

Surface brightness and gas temperature profiles are needed to recover the total mass distribution through the hydrostatic equilibrium equation. The azimuthally averaged surface brightness profile was extracted from the exposure-corrected background-subtracted Chandra images in the $[0.7 - 2]$ keV band, in a set of circular annuli centred in the X-ray emission peak They estimated the background counts from regions of the same exposure but free from the source emission.

For the spectral analysis, they used the `CIAO` software to extract the source and background spectra. The background spectra was extracted from the same regions used for the spatial analysis. The source spectra were extracted from at least three concentric annuli centred on the X-ray surface brightness centroid,

Name	z	c_{200}	M_{200} $[10^{14}\mathrm{M}_\odot]$
MACS-J0159.8-084	0.405	4.3 ± 0.8	17.80 ± 5.40
MACS-J2228.5+20	0.412	2.7 ± 1.1	15.6 ± 5.1
MS1621.5+264	0.426	2.4 ± 0.9	13.0 ± 4.1
MACS-J1206.2-08	0.440	2.5 ± 0.5	38.1 ± 10.3
MACS-J2243.3-0	0.447	2.7 ± 1.2	14.5 ± 4.4
MACS-0329.7-021	0.450	3.5 ± 0.7	15.9 ± 5.6
RXJ1347.5-1145	0.451	4.5 ± 0.6	40.1 ± 11.2
V1701+6414	0.453	2.2 ± 1.0	7.8 ± 3.4
MACS-J1621.6+381	0.465	3.4 ± 1.0	21.7 ± 10.9
CL0522-3624	0.472	6.3 ± 4.9	6.1 ± 4.6
CL0522-3624	0.494	2.6 ± 0.8	18.6 ± 7.8
MACS-J2214.9-1	0.503	4.4 ± 2.9	17.9 ± 9.0
MACS-J911.2+1746	0.505	2.5 ± 1.0	15.5 ± 5.1
MACS-J0257.1-23	0.505	3.9 ± 2.3	17.3 ± 8.7
V1525+0958	0.516	2.5 ± 1.3	11.1 ± 5.5
MS0015.9+1609	0.541	2.3 ± 0.6	19.9 ± 5.1
CL0848.6+4453	0.543	5.2 ± 4.3	9.4 ± 8.6
MACS-J1423.8+240	0.543	6.2 ± 0.4	7.8 ± 0.8
MACS-J1149.5+22	0.544	3.3 ± 2.0	13.3 ± 4.5
MACS-J0717.5+37	0.546	3.6 ± 0.9	21.7 ± 4.0
CL1117+1744	0.548	4.8 ± 4.5	2.2 ± 1.6
MS0451.6-0305	0.550	3.2 ± 1.4	28.5 ± 11.3
MS2053.7-0449	0.583	4.3 ± 3.7	8.1 ± 6.0
MACS-J2129.4-0	0.589	6.5 ± 4.4	16.0 ± 9.6
MACS-J0647.7+7	0.591	3.7 ± 2.4	25.6 ± 15.2

Table 4.1: Galaxy cluster masses and concentrations estimated by A16. The measurement are relative to $\Delta = 200$.

where the signal-to-noise is larger than 0.3 in the $[0.6 - 7]$ keV band. For each annulus, they analyzed the spectrum using the fitting software XSPEC. They assumed a collisionally-ionized diffuse gas emission model, multiplied by an absorption component, accounting for the hydrogen Galactic column density N_H.

4.2 Mass and concentration estimates

The mass of the X-ray galaxy clusters can be obtained through the hydrostatic equilibrium from the gas density, ρ_{gas}, and the temperature profile, T_{gas}. For a spherical-symmetric distribution of gas with pressure P_{gas} and density ρ_{gas}, in

CL1120+4318	0.600	4.7 ± 4.0	7.0 ± 4.2
CLJ0542.8-4100	0.640	7.0 ± 5.2	6.5 ± 3.6
LCDCS954	0.670	4.8 ± 4.5	2.2 ± 1.7
MACS-J0744.9+392	0.698	6.2 ± 2.8	9.7 ± 4.9
V1221+4918	0.700	6.1 ± 4.8	6.6 ± 4.3
SPT-CL0001-5748	0.700	5.1 ± 3.3	13.3 ± 11.4
RCS2327.4-0204	0.704	2.2 ± 0.4	31.3 ± 7.7
SPT-CLJ2043-5035	0.720	2.6 ± 1.3	15.1 ± 8.1
ClJ1113.1-2615	0.730	6.0 ± 4.4	8.1 ± 6.8
CLJ2302.8+0844	0.734	3.2 ± 2.9	7.9 ± 5.0
SPT-CL2337-5942	0.775	4.8 ± 3.8	21.2 ± 14.1
RCS2318+0034	0.780	4.8 ± 3.7	22.9 ± 17.3
MS1137.5+6625	0.782	3.6 ± 1.9	15.2 ± 8.8
RXJ1350.0+6007	0.810	5.0 ± 4.5	2.8 ± 1.5
RXJ1716.9+6708	0.813	6.6 ± 5.3	6.5 ± 4.9
EMSS1054.5-0321	0.831	3.8 ± 3.2	16.3 ± 8.8
CLJ1226.9+3332	0.888	4.2 ± 2.9	33.7 ± 21.2
XMMUJ1230+1339	0.975	4.2 ± 3.7	8.7 ± 7.1
J1415.1+3612	1.030	3.3 ± 2.5	10.0 ± 6.9
SPT-CL0547-5345	1.067	6.0 ± 4.7	11.9 ± 8.8
SPT-CLJ2106-584	1.132	4.9 ± 4.5	9.0 ± 5.4
RDCS1252-29	1.235	4.6 ± 3.9	5.6 ± 4.5

Table 4.2: Continued from table 4.1.

hydrostatic equilibrium in the gravitational potential ϕ, the Euler's equation can be written as:

$$\frac{1}{\rho_{gas}} \frac{dP_{gas}}{dr} = -\frac{d\phi}{dr} = -\frac{GM(<r)}{r^2}. \tag{4.1}$$

Solving this equation and exploiting the perfect gas equation, one can obtain:

$$M(<r) = -\frac{k_B T_{gas}(r) r}{\mu m_p G} \left(\frac{d \ln n_{gas}}{d \ln r} + \frac{d \ln T_{gas}}{d \ln r} \right), \tag{4.2}$$

where k_B is the Boltzmann's constant, $\mu = 0.6$ is the mean molecular weight of the gas, m_p is the proton mass, G is the gravitational constant and $n_{gas} = \rho_{gas}/\mu m_p$.

A16 measured the cluster mass within the spherical region of radius r_Δ, where they assumed $\Delta = 200$ (see section 2.1). With this assumption and to resolve equation (4.2), Amodeo et al [2016] adopted the NFW functional form to describe the total mass profile, see equations (2.1), (2.3) and (2.4) in section 2.1. They found the best-fit parameters of the NFW mass profile (i.e. concentration and r_s)

by minimizing the χ^2 statistic as follows:

$$\chi^2 = \sum_i \frac{(T_{data,i} - T_{model,i})^2}{\epsilon_{T,i}^2}, \tag{4.3}$$

where the sum is done over the annuli of the spectral analysis, $T_{data,i}$ is the temperature measurement obtained via the spectral analysis, T_{model} is the value obtained by projecting the gas temperature predicted by the model over the annulus, used in the spectral analysis, and ϵ_T is the error on the spectral measurements.

With the parameters c and r_s found via the minimum of the equation (4.3), A16 were able to measure the galaxy clusters mass M_{200} enclosed in the radius r_{200}. In table 4.1 and 4.2, we list their results. The sample cover a mass range from $M = 2.2 \times 10^{14} M_\odot$ to $M = 4.0 \times 10^{15} M_\odot$, with a median value equal to $M = 1.3 \times 10^{15} M_\odot$. The median redshift is equal to $z = 0.59$. This sample permitted the first constraint on the c-M relation at $z > 0.7$ from X-ray data only.

4.3 Cosmological constraints

In this section, we show the constraints on the cosmological parameters that we have obtained using the A16 sample. We have used the B01, B13 and D15 concentration models. We have not used the P12 model due to its shortcomings discussed in section 3.4.3. Figure 4.1 shows the measurements obtained by A16, blue points, with errors. The upper panel shows the c-M relation, while the bottom panel shows the c-z relation. Red, green and black lines are the relations predicted for the D15, B13 and B01 models, respectively, in a cosmological model with $\Omega_M = 0.3$ and $\sigma_8 = 0.8$. For the c-M relation, the models are plotted at the median redshift of the sample, $z_{median} = 0.59$. The D15 model is the only one to show an upturn.

For the c-z relation, the models are showed at the median mass of the sample, $13.3 \cdot 10^{14} M_\odot$. Due to the too large error bars, we cannot say which model is better than the others. We point out that the B01 model is not able to predict a concentration value for $M > 10^{15.4} M_\odot$ at redshift $z = 0.59$, see figure 4.1.

In figures 4.2, 4.3 and 4.4, our cosmological constraint are shown assuming the B01, B13 and D15 model, respectively. These plots are built up alike figure 3.6, i.e.: the bottom-left panel shows the 2D χ^2 distribution in the parameter space. We want to point out that for the parameter χ^2 we intend the quantity $-2\ln\Gamma$ (see equation (3.6) in section 3.3). The red dot indicates the best-fit values, i.e. the combination of the Ω_M and σ_8 at which χ^2 is minimum. The lines correspond to the χ^2 at 1,2 and 3-σ levels ($\Delta\chi^2 = 2.3, 6.17, 11.8$, respectively). The bottom-right and upper-left panels show the probability density function for the σ_8 and Ω_M cosmological parameters, respectively. The solid black line indicates the value of the cosmological parameter at which the χ^2 is minimum and the dashed black
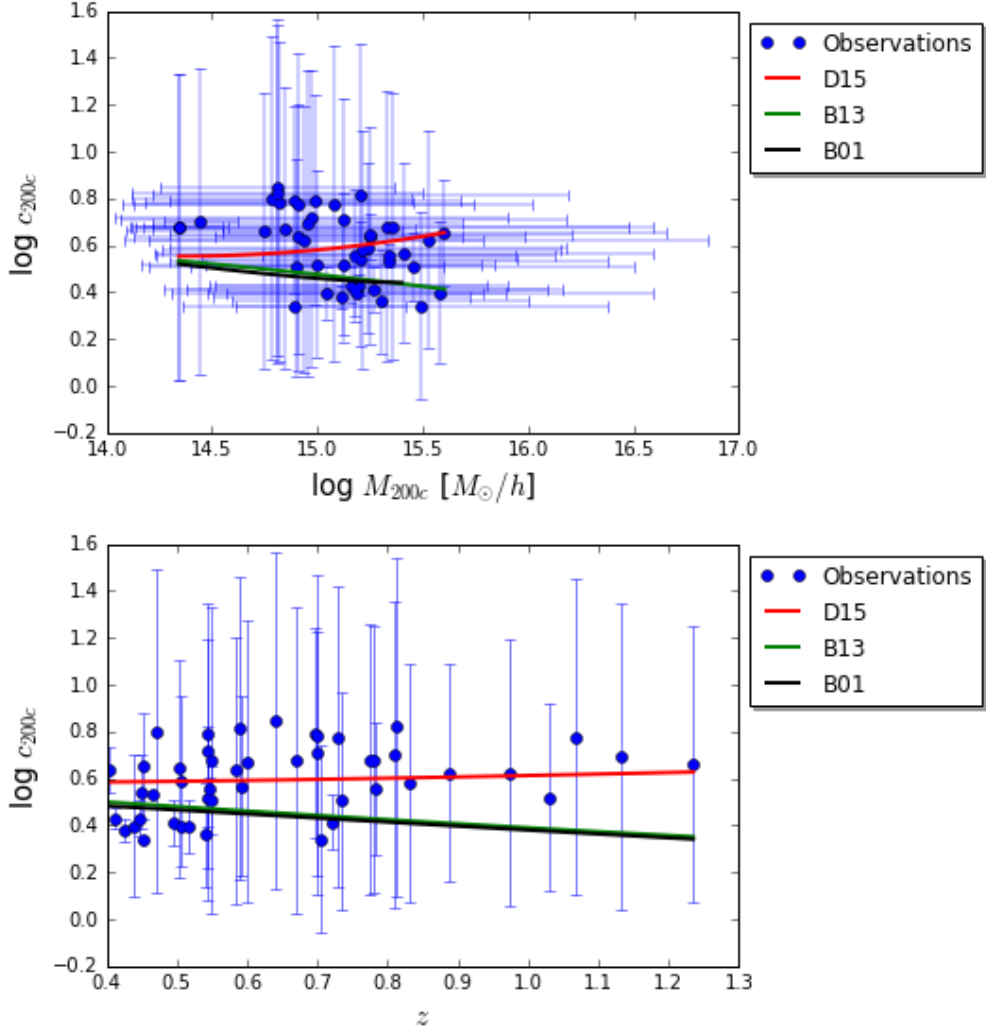
Figure 4.1: The c-M, upper panel, and c-z, bottom panel, relations for the A16
sample, blue points with errors. Red, green and black lines are the relations
predicted by the D15, B13 and B01 models. For the c-M relations, the models are
evaluated at the median redshift of the sample, $z = 0.59$. For the c-z relation, the
models are showed at the median mass, $13.3 \times 10^{14} M_\odot$. All models are computed
in a cosmological model with $\Omega_M = 0.3$ and $\sigma_8 = 0.8$.

lines indicate the levels where the $\Delta\chi^2_{reduced} = 1.0$ for the single parameter. The
red line indicates the mean value for the cosmological parameter calculated via
method 2 (see section 3.3.1). In the upper-right panel, the estimates are shown.
The first two values refer to the first method where the error refer to the 1-σ levels
in the 2-D χ^2, while the second two values refer to the second method. The figures
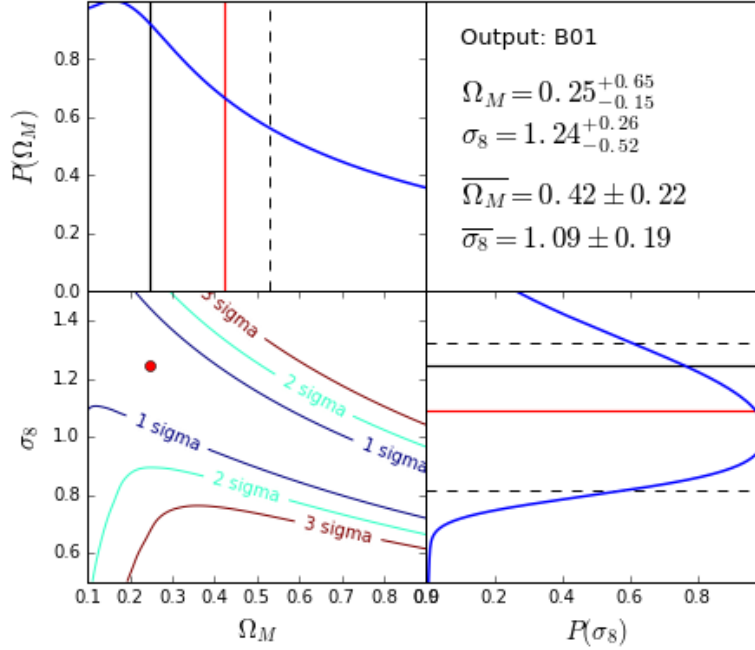
Figure 4.2: Results obtained from the A16 for the B01 model. Each figure is organized as follow. *Bottom-left panel*: is shown the χ^2 distribution in the parameter space, with the contours at 1,2 and 3-σ distribution. The red dot indicates the combination of cosmological parameters at which χ^2 is minimum. *The upper-left and bottom-right*: are shown the probability density functions for the single parameter. *Upper-right panel*: the first two parameter are the results refer to method 1, while the other two parameter to method 2 (see section 3.3.1).

4.2, 4.3 and 4.4 refer to the B01, B13 and D15 models, respectively.

From the 2-D χ^2 distribution for the B01 model, figure 4.2, we can see that there is a strong degeneracy between the two cosmological parameters; there are several combinations of Ω_M and σ_8 at which the χ^2 is within the 1-σ region. With regards to Ω_M, we can see that the region under the 1-σ levels is extended over the entire range of the parameter. Each value of the parameter Ω_M is statistically compatible with the sample. Moreover, the probability density function $P(\Omega_M)$ is quite flat, much more than $P(\sigma_8)$. If we assume a flat prior distribution for the probability density function, $P(\Omega_M) =$const $\forall \Omega_M \in [0.1, 0.9]$, we expect a mean value equal to $\overline{\Omega}_M = 0.5 \pm 0.3$. The mean value obtained with the probability density function obtained, method 2 in section 3.3.1, is equal to $\overline{\Omega}_M = 0.42 \pm 0.22$, not much different respect 0.5. Therefore, we can say that the constraint on the Ω_M cosmological parameter is weak. The parameter σ_8 is better constrained because not the entirety dominion of this parameter is within the 1-σ level and
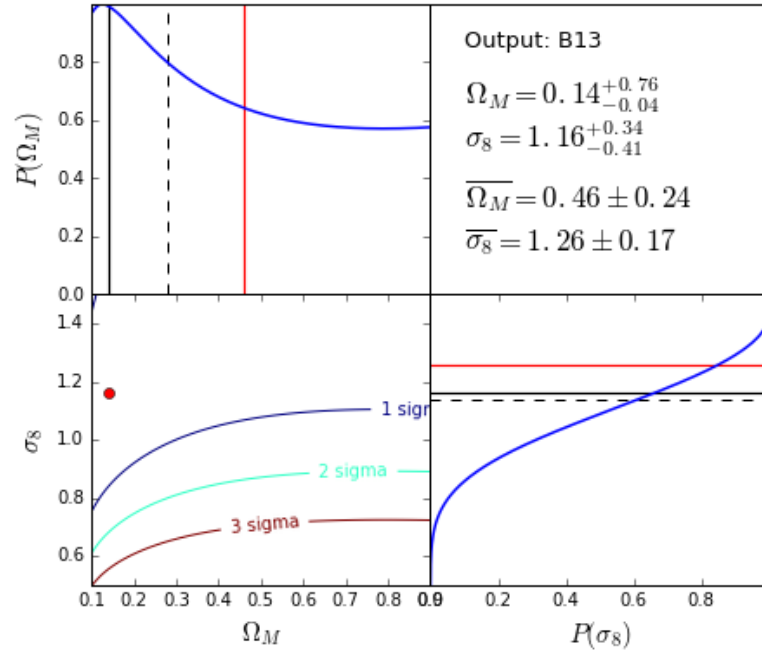
Figure 4.3: As in figure 4.2 but for the B13 model.

the probability density function is zero for $\sigma_8 < 0.6$. In this case, the presence of a peak is evident, even if the distribution remains broad.

With regard to the B13 model, figure 4.3, we want to point out that the probability density function for the parameter Ω_M is flatter than in the B01 case. Moreover, the mean value obtained from the method 2 is out of the 1-σ region (dashed black line in the upper-left panel) for the parameter, whereas, in the B01 case, we do not see this discrepancy.

The situation is different for the D15 model, figure 4.4, where there is evidence of a peak for the probability density functions of both cosmological parameters. In this case, the 2-D region χ^2 under the 1-σ level is constrained for both parameters. Therefore, the constraints on the cosmological parameters are stronger than the other two models.

The fact that the probability functions are well behaved may suggest that the D15 model provide a better fit to the data than the B01 or B13. However, a model comparison analysis should be run to make quantitative assessment. Figure 4.5 shows the overlapping of the 2-D χ^2 distribution at 1 and 2-σ for the three models. The red and black lines refer to the B01 and B13 models, respectively, while the blue region to the D15 model. The D15 model provides the main contribution to the region a 1-σ level, that means to determinate the extension of this region, while the B13 and B01 models contribute very little.

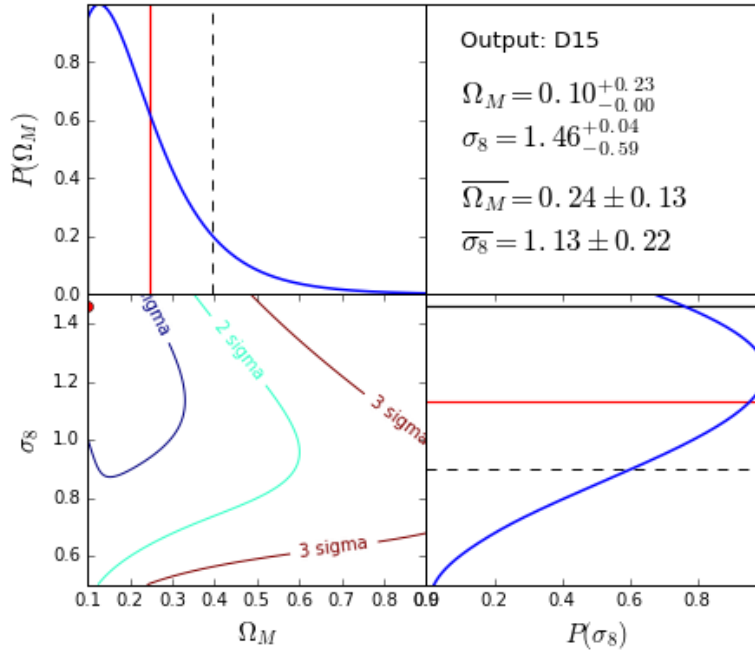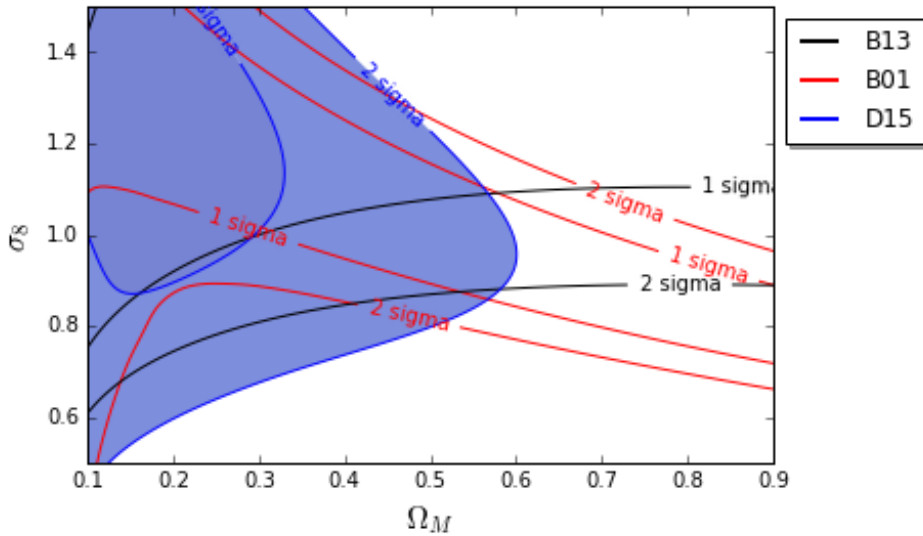Figure 4.4: As in figure 4.2 but for the D15 model.

Figure 4.5: Overlapping of the three 2-D χ^2 distribution for the A16 sample. The blue, black and red lines are referred to the D15, B13 and B01 models, respectively.

In table 4.3 the cosmological parameter obtained by our code for the A16 sample are listed. The errors refer to the $\Delta\chi^2_{reduced} = 1.0$ for the single parameter.

Parameter	D15	B13	B01
A16			
Ω_M	$0.10^{+0.30}_{-0.00}$	$0.14^{+0.14}_{-0.04}$	$0.25^{+0.28}_{-0.15}$
σ_8	$1.46^{+0.04}_{-0.59}$	$1.16^{+0.34}_{-0.02}$	$1.24^{+0.08}_{-0.42}$
$\widetilde{\chi}^2$	20.60	20.65	19.01
E10			
Ω_M	$0.14^{+0.14}_{-0.04}$	$0.90^{+0.00}_{-0.17}$	$0.90^{+0.00}_{-0.03}$
σ_8	$1.28^{+0.07}_{-0.19}$	$0.67^{+0.14}_{-0.06}$	$0.55^{+0.08}_{-0.00}$
$\widetilde{\chi}^2$	66.55	57.33	47.45
A16 + E10			
Ω_M	$0.13^{+0.12}_{-0.03}$	$0.32^{+0.58}_{-0.22}$	$0.42^{+0.11}_{-0.19}$
σ_8	$1.31^{+0.06}_{-0.19}$	$0.91^{+0.08}_{-0.12}$	$0.86^{+0.12}_{-0.19}$
$\widetilde{\chi}^2$	87.50	87.81	81.80

Table 4.3: Cosmological parameters derived with our code, for the different models, for the Amodeo et al [2016] sample, the E10 sample, and using the two samples together. The parameter $\widetilde{\chi}^2$ correspond to the first term into the summation in equation (3.6) in section 3.3.

The parameter $\widetilde{\chi}^2$ is referred to first term into the summation in equation (3.6) in section 3.3. The differences between the values of $\widetilde{\chi}^2$, for the different models, is small and therefore is hard to determinate which model is better than the others.

4.4 The Ettori et al. [2010] sample

We have run our code with another sample, the Ettori et al. [2010] sample (E10 hereafter). The E10 sample considers 44 galaxy clusters observed with *XMM-Newton* in the redshift range $0.1 < z < 0.3$, with a median redshift $z_{median} = 0.17$. They extracted the surface brightness profiles from MOS images in the energy band $[0.7 - 1.2]$ keV. They estimated the background contribution fitting a spectral model in the external ring, with diameter $10 - 12$ arcmin around the source. To measure the mass and the concentration of the galaxy clusters, E10 used the method later employed by A16. The masses obtained by E10 cover a range between

Name	z	c_{200}	M_{200} [10^{14}M$_\odot$]
Abell2700	0.092	$8.6^{+1.52}_{-1.30}$	1.90 ± 0.23
Abell3911	0.097	$5.59^{+1.33}_{-1.39}$	3.88 ± 0.50
Abell3827	0.098	$4.47^{+0.67}_{-0.64}$	6.61 ± 0.731
AbellS0084	0.108	$12.77^{+3.80}_{-3.18}$	0.94 ± 0.16
Abell2034	0.113	$2.46^{+0.81}_{-0.06}$	17.64 ± 2.17
Abell2051	0.115	$2.75^{+0.49}_{-0.06}$	4.73 ± 0.42
Abell3814	0.118	$4.79^{+0.43}_{-0.49}$	2.21 ± 0.21
Abell2050	0.118	$7.06^{+1.64}_{-1.54}$	2.84 ± 0.41
Abell1348	0.119	$3.15^{+0.19}_{-0.24}$	4.88 ± 0.37
Abell1084	0.132	$4.56^{+0.34}_{-0.25}$	2.86 ± 0.18
Abell1068	0.138	$3.02^{+0.20}_{-0.22}$	6.40 ± 0.48
Abell3856	0.138	$3.16^{+0.85}_{-0.55}$	8.76 ± 1.62
Abell3378	0.141	$4.10^{+0.34}_{-0.34}$	4.51 ± 0.36
Abell22	0.142	$4.17^{+1.41}_{-1.07}$	10.03 ± 2.67
Abell1413	0.143	$5.83^{+0.57}_{-0.35}$	6.12 ± 0.32
Abell2328	0.147	$2.23^{+1.63}_{-0.21}$	5.96 ± 1.12
Abell3364	0.148	$4.10^{+0.59}_{-1.17}$	7.89 ± 1.51
Abell2204	0.152	$2.81^{+0.02}_{-0.28}$	15.93 ± 1.19
Abell907	0.153	$2.39^{+0.42}_{-0.39}$	11.94 ± 2.02
Abell3888	0.153	$4.28^{+2.31}_{-1.16}$	13.42 ± 4.15
RXCJ2014.8-2430	0.161	$3.86^{+0.15}_{-0.30}$	7.56 ± 0.53
Abell3404	0.167	$4.58^{+1.06}_{-0.96}$	7.08 ± 1.12
Abell2218	0.176	$6.26^{+2.46}_{-1.48}$	4.76 ± 0.74
Abell1689	0.183	$8.31^{+0.64}_{-0.63}$	7.36 ± 0.44
Abell383	0.187	$3.40^{+0.03}_{-0.42}$	4.43 ± 0.37

Table 4.4: Galaxy cluster masses and concentrations estimated by E10. The measurement are relative to $\Delta = 200$.

0.9×10^{14}M$_\odot$ and 1.8×10^{15}M$_\odot$. In table 4.4 and 4.5, we list their results.

Figure 4.6 shows the measurements obtained by E10, as in fig. 4.1. With regards to the c-M relation, upper panel, the models are plotted at the median redshift, $z_{median} = 0.17$. Also in this case, the D15 model is the only to show an upturn at large mass values. For the c-z relation, bottom panel, the models are showed at the median mass, $6.98 \cdot 10^{14}$M$_\odot$. We cannot say which model is better

Abell209	0.206	$3.09^{+0.67}_{-0.77}$	8.60 ± 1.23
Abell963	0.206	$4.35^{+0.94}_{-0.76}$	6.17 ± 0.83
Abell773	0.217	$3.27^{+1.49}_{-1.05}$	10.94 ± 3.12
Abell1763	0.223	$7.50^{+2.30}_{-3.41}$	4.25 ± 0.74
Abell2390	0.228	$2.06^{+0.12}_{-0.04}$	24.71 ± 1.16
Abell2667	0.230	$2.24^{+0.08}_{-0.02}$	15.88 ± 0.45
RXCJ2129.6+0005	0.235	$3.71^{+0.27}_{-0.38}$	5.40 ± 0.44
Abell1835	0.253	$2.64^{+0.34}_{-0.09}$	17.53 ± 1.41
Abell3088	0.253	$3.15^{+0.88}_{-0.78}$	10.44 ± 2.39
Abell68	0.255	$2.64^{+0.82}_{-0.06}$	15.96 ± 1.97
E1455+2232	0.258	$6.32^{+0.53}_{-0.51}$	3.66 ± 0.29
RXCJ2337.6+0016	0.273	$4.99^{+3.52}_{-2.18}$	6.81 ± 1.91
RXCJ0303.8-7752	0.274	$1.85^{+3.52}_{-0.09}$	13.21 ± 2.33
RXCJ0532.9-3701	0.275	$5.97^{+2.43}_{-1.82}$	6.88 ± 1.83
RXCJ0232.2-4420	0.284	$1.80^{+0.66}_{-0.04}$	14.28 ± 1.90
ZW3146	0.291	$3.37^{+0.15}_{-0.26}$	7.79 ± 0.49
RXCJ0043.4-2037	0.292	$7.80^{+5.05}_{-3.51}$	4.70 ± 1.24
RXCJ0516.7-5430	0.295	$2.41^{+2.82}_{-0.85}$	10.44 ± 2.88
RXCJ1131.9-1955	0.307	$2.43^{+1.16}_{-0.76}$	11.31 ± 2.50

Table 4.5: Continued from table 4.4.

than the others because the error bars are too large.

The three left panels in figure 4.7 show the cosmological constraints for the E10 sample. The upper, middle and bottom panels refer to the D15, B13 and B01 models, respectively. In table 4.3 we list the best-fit cosmological parameters obtained, where the error bands refer to the $\Delta\chi^2_{reduced} = 1.0$ for the single parameter.

With regards to the D15 model, upper left-panel in fig. 4.7, we can see that this model provides good constraints for each parameter, the probability density functions have a narrow quasi-Gaussian distribution for each parameter. The $P(\Omega_M) \simeq 0$ for $\Omega_M < 0.6$ and $P(\sigma_8) \simeq 0$ for $\sigma < 0.7$.

The B13 model, middle left-panel, provides good constraints only for the σ_8 parameter. For the parameter Ω_M, the 1,2 and 3-σ contours are very wide, over
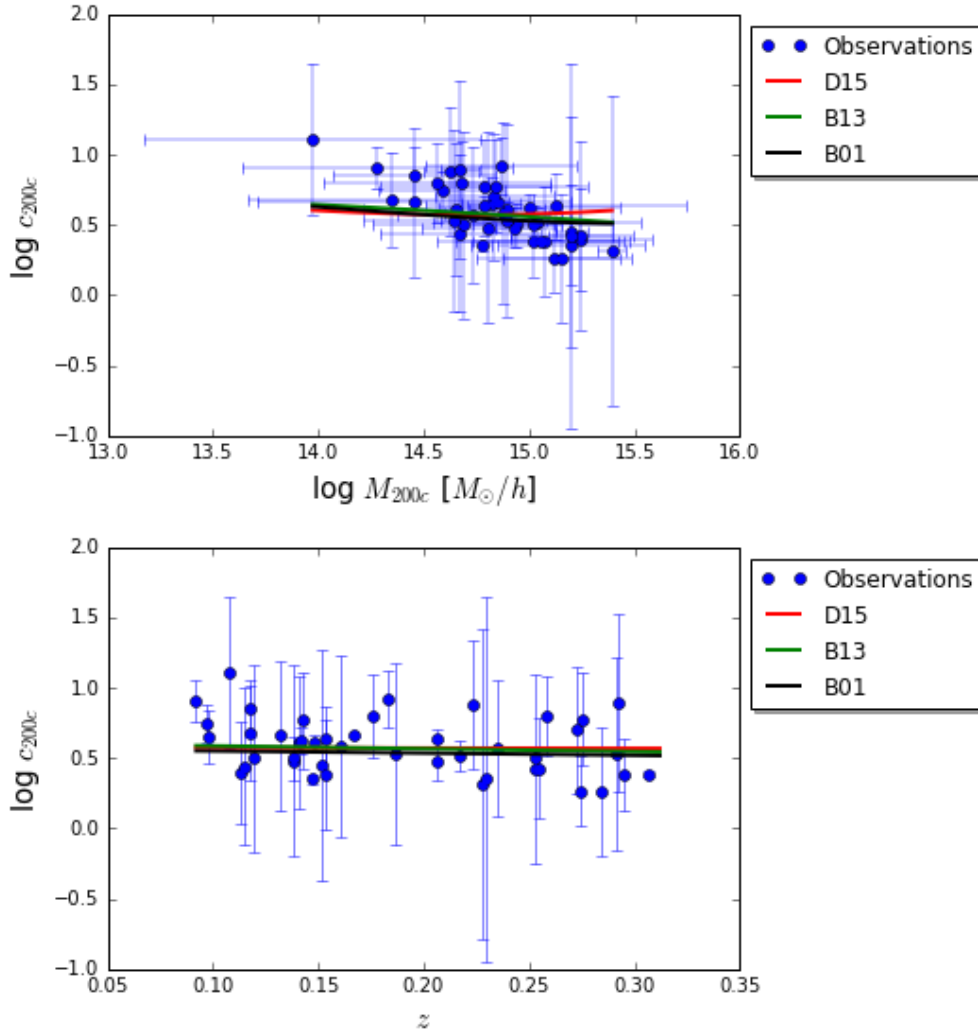
Figure 4.6: As in fig. 4.1 but for the E10 sample. For the c-M relations, the models are evaluated at the median redshift of the sample, $z = 0.17$. For the c-z relation, the models are showed at the median mass, $6.98 \times 10^{14} M_{\odot}$.

the entire range of the parameter; the peak of $P(\Omega_M)$ is at $\Omega_M = 0.90$.

The results for the B01 model, bottom-left panel, are similar to the D15 model. The $P(\sigma_8)$ distribution has a very narrow peak at low values of the parameter; the distribution $P(\Omega_M)$ is broader with a peak at large values.

For all the three models, the 1,2 and 3-σ contours cover a more constrained region than the regions obtained with the A16 sample. This is due to the statistical uncertainties on mass and concentration of the two samples. The E10 sample consists of galaxy clusters at lower redshift than the A16 sample. Therefore, E10
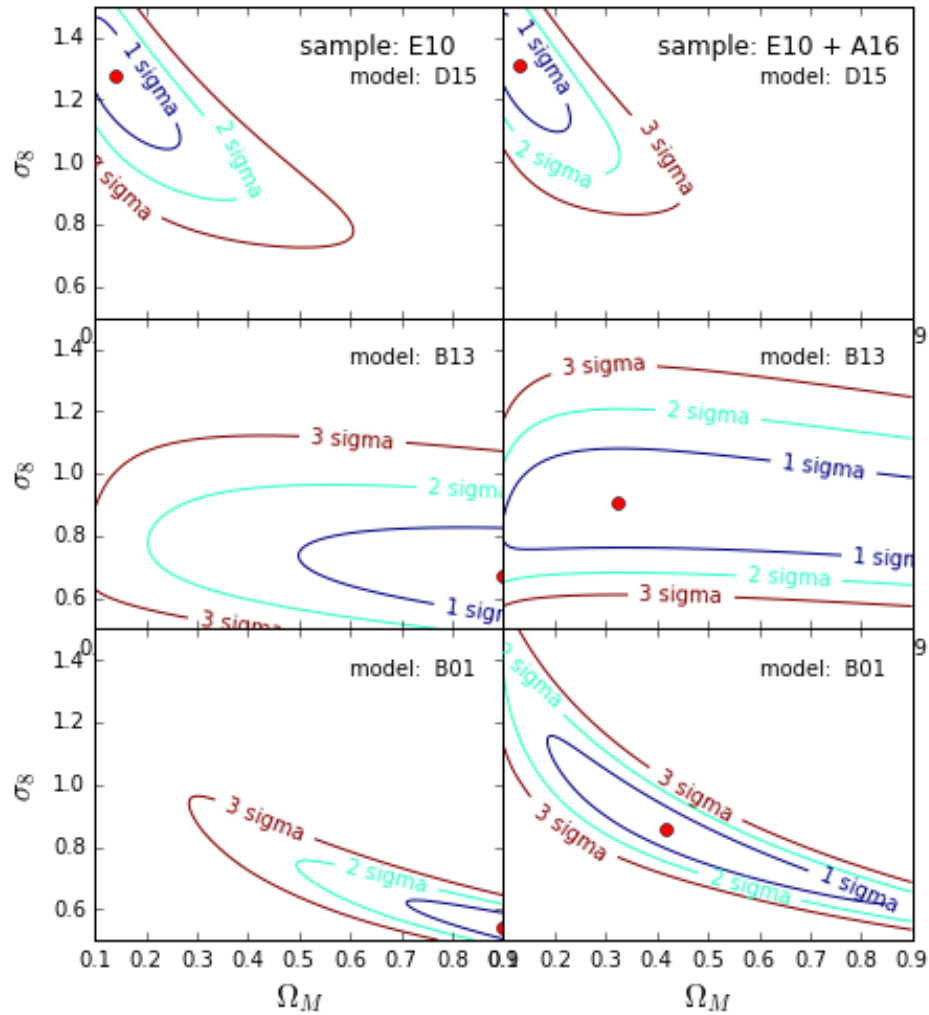
Figure 4.7: Cosmological constraints obtained with the E10 sample, left panels, and for the joint A16+E10 sample, right panels. The first, second an third panel refer to the D15, B13 and B1 models. Lines are as in bottom-left panel in fig. 4.2.

were able to do measurements with better precision. However, even if the values of $\widetilde{\chi}^2$ seem to prefer the B01 model as the better model, the B01 and B13 models predict too high value of the Ω_M cosmological parameter with respect to the D15 model. All models are in agreement if we consider the 3-σ distribution.

4.5 Joint analysis of the samples

We have run our code using the two samples, the A16 and E10 samples, together. Thanks to the joints analysis, we can obtain better results adding the information at lower redshift from E10 to the high redshift of A16. The three right panels in figure 4.7 show the cosmological results for the combined sample. In table 4.3 the cosmological constraints are shown.

   With regards to the D15 model, the regions at 1,2 and 3-σ levels are a little much more constrained using the two samples. With regards to the B13 model, $P(\Omega_M)$ is similar to the distribution obtained using the A16 sample only, but the minimum moves to higher values of the parameter. For σ_8, the constraints are significantly improved, the $P(\sigma_8)$ is quasi-Gaussian around the best-fit value. With regards to the B01 model, the elongation of the regions are very similar, but the area of the confidence regions is smaller than using a single sample.

4.6 Comparison with previous works

We have compared our results relative to the A16 sample with some previous works that measured cosmological parameters from the analysis of cluster in the X-ray band. Ettori et al [2009] and Mantz et al. [2014] used the cluster baryon fraction in clusters as a proxy for the ratio Ω_b/Ω_M assuming that the galaxy clusters are representative of the cosmic baryon budget. Ettori et al. [2009] and Mantz et al. [2014] studied 52 and 40 X-ray luminous galaxy clusters, respectively, observed with *Chandra* in the redshift range $0.3 < z < 1.273$ and $0.078 < z < 1.063$, respectively.

   Vikhlinin et al [2009] used the galaxy cluster mass function as a cosmological probe. They used two cluster samples, the first one with 37 galaxy cluster observed with *Chandra* at a mean redshift $\overline{z} = 0.55$, the other one including 49 clusters observed with *ROSAT* at $z \approx 0.05$.

   Mantz et al. [2015] used masses from weak lensing and scaling relations between X-ray observables, for 50 galaxy clusters observed with *ROSAT* in the redshift range $0.3 < z < 0.5$.

   The cosmological parameters obtained from the relative papers are listed in table 4.6. Even if the number of the objects observed is slightly different among the different studies, our cosmological parameters obtained for the A16 sample and for the joint samples A16+E10 are in agreement with the previous studies. The main difference between the results are in the error bands. Our results have larger error bars than the results obtained from the previous works, especially for the A16 sample. This is due to the fact that (i) the A16 sample provides estimates of concentration and mass with large statistical uncertainties because of the high

Paper	Ω_M	σ_8	Method
Ettori et al. [2009]	$0.32^{+0.04}_{-0.05}$	-	cluster baryon fraction
Vikhlinin et al. [2014]	0.30 ± 0.05	0.813 ± 0.037	galaxy cluster mass function
Mantz et al. [2014]	0.29 ± 0.04	-	weak gravitational lensing
Mantz et al. [2015]	0.26 ± 0.03	0.83 ± 0.04	cluster baryon fraction

Table 4.6: Cosmological parameters obtained from previous works.

redshift regime where these objects were studied (with a significant dimming of
the observed X-ray surface brightness), (ii) the large intrinsic scatter considered
in our analysis. With the two samples together, the error bars are smaller than
use the A16 sample only, but remain larger than the previous works.

<div style="text-align: right;">*5*</div>

Predictions for future investigations

In this chapter, we studied how the knowledge on the cosmological parameters inferred from the c-M relation can change depending on several quantities by analyzing mock samples. Our goal is to understand which features affect the precision and accuracy more in constraining the cosmological parameters. In this chapter we report how we have created the several mock data, how the precision and the accuracy evolve, and which future space missions will be able to efficiently constrain the cosmological parameters using the c-M relation.

5.1   Precision and accuracy

We have run several simulations to understand how our knowledge on the cosmological parameters change, varying several input parameters. These parameters are the number of the objects observed, N_{data}, the intrinsic scatter, σ_{int}, the observational uncertainties on the concentration and the mass, ε_c and ε_M, and the redshift of the observed clusters, z_{obs}. As far the observational uncertainties are concerned, we have defined the new variable f as follows:

$$\varepsilon_c(z) = \varepsilon_c^*(z) * f, \tag{5.1}$$

$$\varepsilon_M(z) = \varepsilon_M^*(z) * f, \tag{5.2}$$

where $\varepsilon_c^*(z)$ and $\varepsilon_M^*(z)$ are referred to the observational uncertainties of present day samples, section 3.2.1. Therefore, the variable f is a scale factor and represents the possibility of better future observations. E.g., $f = 0.5$ means that we are

Variable	Values
N_{data}	$50, 100, 200, 500, 10^3, 3 \times 10^3, 10^4$
σ_{int}	$0.11, 0.05, 0.01$
f	$1.0, 0.5, 0.2$
z	$0.0, 0.5, 1.0, 1.5$

Table 5.1: Values of the four variables that we have used to create the mocks data; σ_{int} is in $\log_{10}$-space.

considering measurements with a precisions 50% better than the values reported in section 3.2.1.

In table 5.1, we list the values of the four input parameters that we have used to create the simulations. We want to point out that the variable σ_{int} is in $\log_{10}$-scale, see sections 2.5 and 3.2.1. The mass range adopted to create the mock data is between $10^{14}h^{-1}M_\odot$ and $2 \times 10^{15}h^{-1}M_\odot$. The cosmological model adopted is Planck15, where $\Omega_M = 0.31$ and $\sigma_8 = 0.82$, see table 1.1. We considered only the D15 concentration model because it is the most recent model and it is based on the most accurate N-body numerical simulations.

Since we are interested in understanding how well the cosmological parameters can be measured with our method, we have studied the *precision* and the *accuracy*. Figure 5.1 shows what we mean by precision and accuracy. The middle red dot in each panel indicates the target that we would like to hit. The black dots indicate what we have found. The upper-left panel shows the case with low precision and low accuracy. The black points are not concentrated anywhere (low accuracy) and they are very scattered (low precision). The bottom-left panel shows the case with high accuracy, i.e. the black points around the center, but with low precision, i.e. the points are still scattered. The upper-right panel shows the opposite case, that is the case with high precision and low accuracy. The black points are very close, but they are very far from the center of the target. The bottom-right panel shows the best case with high precision and high accuracy. The points are concentrated in the middle of the target and they are very close to each other.

To understand how the precision and the accuracy on the cosmological parameters changes in our simulations, we have studied how the contour plot of the χ^2 in the space parameters, at 1-σ confidence level ($\Delta\chi^2 = 2.3$) changes. For this reason, we have defined the statistical precision, S, and the accuracy, or systematic
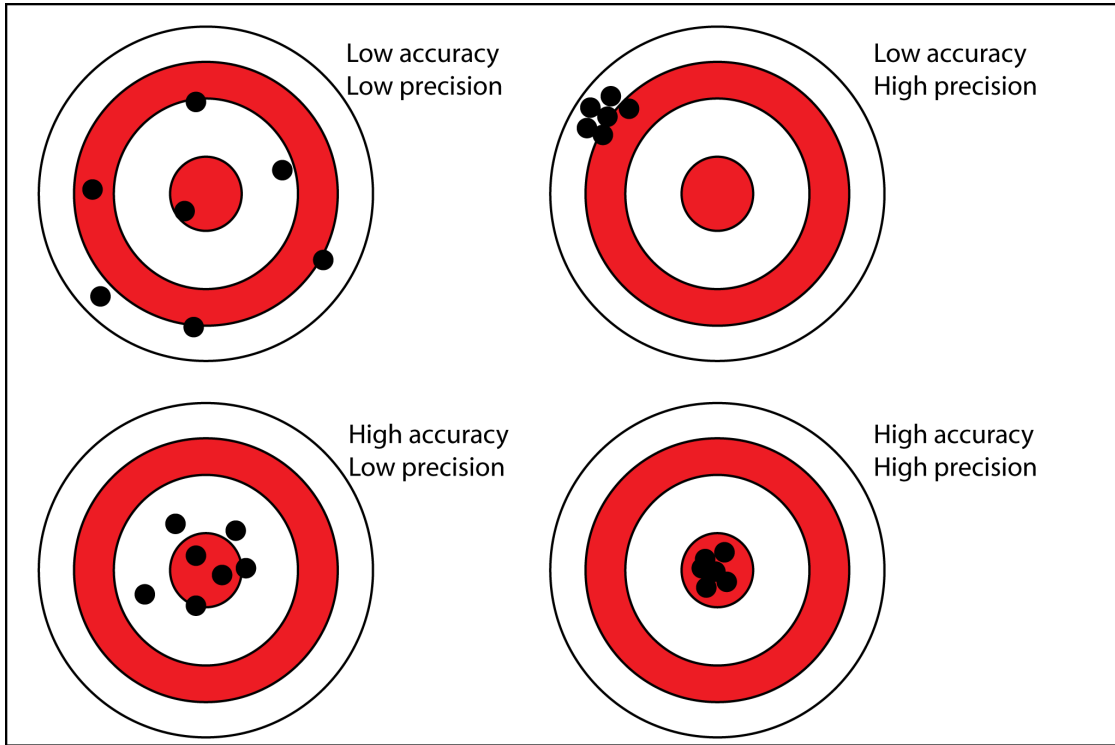
Figure 5.1: Examples to understand the meaning of precision and accuracy. The upper-left panel shows data with low precision and accuracy. The bottom-left panel shows data with low precision but with high accuracy. The upper-right panel shows data with high precision and low accuracy. The bottom-right panel shows the best case, with high precision and high accuracy.

bias, B, as follows:

$$S = \frac{1}{\delta_{\Omega_M} * \delta_{\sigma_8}}, \tag{5.3}$$

$$B = \frac{1}{\Delta_{\Omega_M} * \Delta_{\sigma_8}}, \tag{5.4}$$

where the quantities δ_{Ω_M} and δ_{σ_8} indicate the absolute statistical uncertainties of the cosmological parameters obtained from the 2-D χ^2 at 1-σ confidence level. The quantities Δ_{Ω_M} and Δ_{σ_8} indicate the difference between the best-fit cosmological parameters, found via our code, and the cosmological parameters of the input cosmology.

With the definition (5.3), a high value of the statistical precision indicates that we have found the best fitting cosmological parameters with high precision, that means low values of δ_{Ω_M}, δ_{σ_8}. For instance, if we constrain the cosmological parameters at 1% level, e.g. $\Omega_M = 0.300 \pm 0.003$ and $\sigma_8 = 0.800 \pm 0.008$, the

value of S is $= 1/(0.003 * 0.008) \approx 4 \times 10^4$. For cosmological parameters with asymmetric error bars, we have considered the mean value of the two errors. E.g., if we obtained a cosmological parameter as $\Omega_M = 0.28^{+0.14}_{-0.06}$, the value of δ_{Ω_M} used to measure S is $\delta_{\Omega_M} = 0.10$. With the definition (5.4), a high value of the systematic bias indicates that the best-fit cosmological parameters are very close to the input parameters. E.g., if the cosmological parameters found via the code are $\Omega_M = 0.30$ and $\sigma_8 = 0.80$, using the Planck15 cosmology, the value of B is $= 1/(0.01 * 0.02) \approx 5 \times 10^3$.

We want to find the region of the parameter space where systematic errors are negligible with respect to statistical uncertainties and we want statistical uncertainties to be small. If we obtain cosmological parameters with precision larger than accuracy, this means that we are likely dominated by systematics, as explained before and as showed in fig. 5.1. Therefore, we are interested to find the combination of the several parameters at which $S \lesssim B$.

5.2 Results

To obtain statistically more significant results, we have run the code ten times for each combination of the parameters in table 5.1, and we have analyzed the median values of S and B. We set the cosmological parameters range in $\Omega_M \in [0.10, 0.90]$ and $\sigma_8 \in [0.5, 1.5]$. We set the mass distribution between $M_{min} = 10^{14} \mathrm{h}^{-1} \mathrm{M}_\odot$ and $M_{max} = 2 \cdot 10^{15} \mathrm{h}^{-1} \mathrm{M}_\odot$.

5.2.1 The statistical precision S

Figure 5.2 shows the evolution of the median values of precision S with N_{data} and f, at redshift $z = 0$ and at fixed σ_{int}. The upper, middle and bottom panels refer to the different values of σ_{int}, that are $\sigma_{int} =0.11$, 0.05 and 0.01, respectively. The green, red and blue points refer to $f =1.0$, 0.5 and 0.2, respectively. As we can see, the parameter S increases monotonically with the number of the objects observed, as expected. For $\sigma_{int} =0.11$ and 0.05, the parameter f does not influence significantly the results. In this cases, S grows from ≈ 10 to $\approx 600 \div 900$ with $\sigma_{int} = 0.11$, and grows from ≈ 20 to $\approx 2 - 3 \times 10^3$ with $\sigma_{int} = 0.05$, over the entire range of N_{data}, i.e. from $N = 50$ to $N = 10^4$. The effect of the parameter parameter f becomes dominant at the lowest value of σ_{int}, i.e. the differences for the three values of f are very large, up to an order of magnitude. The parameter S changes from ≈ 30 for $f = 1.0$ to ≈ 200 for $f = 0.2$ at $N_{data} = 50$, and changes from $\approx 10^4$ for $f = 1.0$ to $\approx 3 \times 10^5$ for $f = 0.2$ at $N_{data} = 10^4$.

Figure 5.3 shows the same results of 5.2 but for $z = 1.0$. Also in this case, the parameter S increases with N_{data} but less steeply than in the case with $z = 0$. This
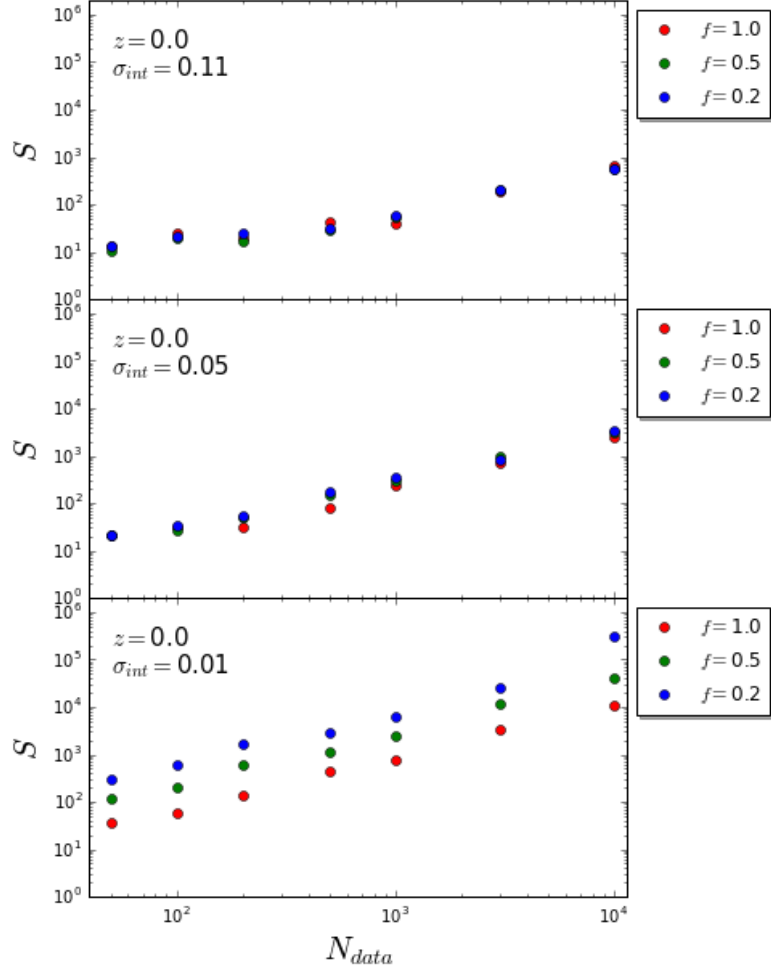
Figure 5.2:   The dependence of the median values of S on N_{data} and f, at fixed σ_{int} and at fixed redshift $z = 0$. The upper, middle and bottom panel refer to $\sigma_{int} = 0.11, 0.05$ and 0.01, respectively. The green, red and blue points refer to $f = 1.0, 0.05$ and 0.2, respectively. The mean uncertainties of the data, in $\log_{10}$-space, are $0.19, 0.15$ and 0.16 dex for the upper, middle and bottom panel, respectively.

fact is due to the larger values of ε_c and ε_M at $z = 1$ (section 3.2.1). Moreover, the parameter S is strongly influenced by f for all the three values of σ_{int}, and the effect is more significant for larger values of N_{data}. The parameter σ_{int} has a weak influence on the results at lower values of N_{data} and at fixed f.

With $\sigma_{int} = 0.11$, S changes from ≈ 5 for $f = 1.0$ to $\approx 10 \div 11$ for $f = 0.2$ at $N_{data} = 50$, and it is ≈ 100 at $N_{data} = 10^4$. At $\sigma_{int} = 0.01$ and $N_{data} = 50$, S changes from ≈ 6 for $f = 1.0$ to $\approx 10 \div 20$ with $f = 0.2$. At $\sigma_{int} = 0.01$ and
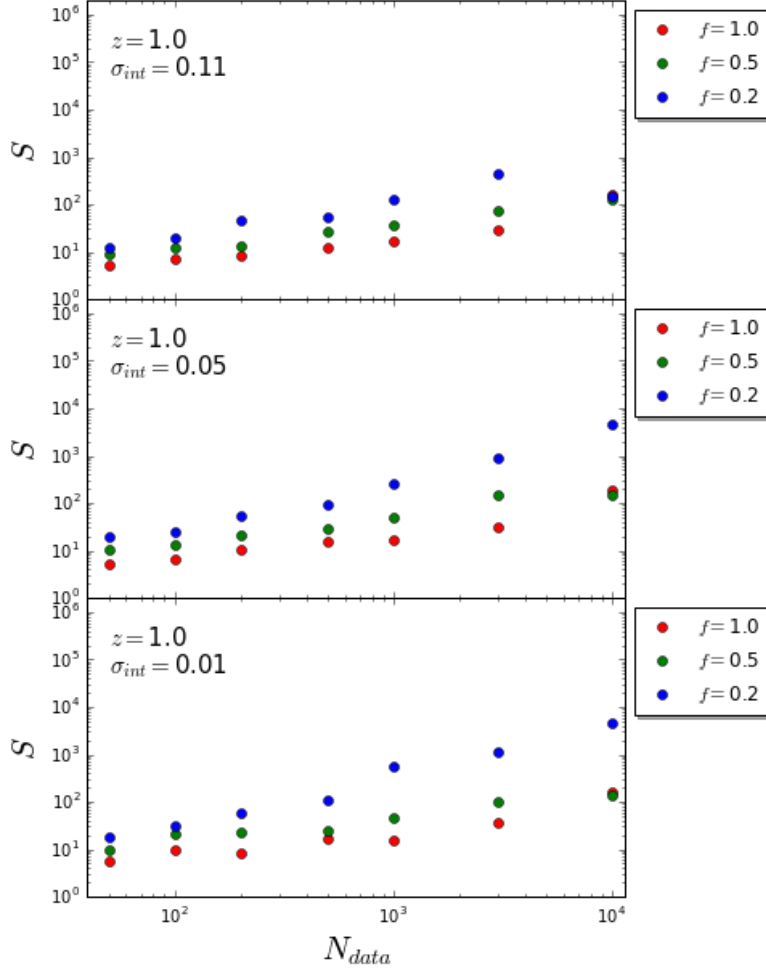
Figure 5.3: As in fig. 5.2 but for $z = 1.0$. The mean uncertainties of the data, in $\log_{10}$-space, are $0.24, 0.23$ and 0.24 dex for the upper, middle and bottom panel, respectively.

$N_{data} = 10^4$, S changes from $\approx 100 \div 200$ for $f = 1.0$ to $\approx 5 \times 10^3$ for $f = 0.2$.

Figure 5.4 shows the evolution of the median values of S with N_{data} and z, at fixed f and at fixed $\sigma_{int} = 0.11$. The upper, middle and bottom panels refer to $f = 1.0, 0.5$ and 0.2, respectively, while the red, green, blue and yellow points refer to $z = 0.0, 0.5, 1.0$ and 1.5, respectively. With $f = 1.0$, the parameter S grows very little with N_{data}; it is approximately constant at higher redshift.

For lower redshifts, S grows faster after $N_{data} = 1 - 3 \times 10^3$. Moreover, the maximum value reached by S is $\approx 800 \div 900$. At $f = 0.5$, S grows slowly with N_{data}. In this case, the maximum value of S is $\approx 2 \times 10^3$. At $f = 0.2$, S increases faster than in the other two cases, until a maximum value $\approx 9 \times 10^3$. However, in
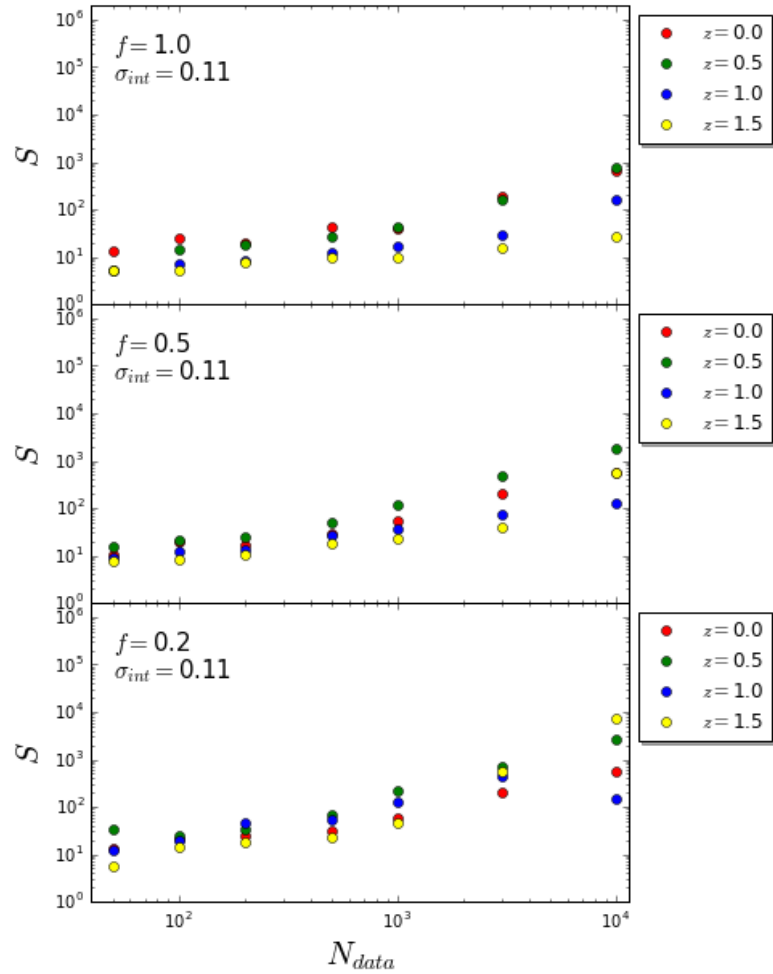
Figure 5.4: The dependence of the median values of S on N_{data} and z, at fixed values of f and at $\sigma_{int} = 0.11$. The upper, middle and bottom panels refer to $f = 1.0, 0.5$ and 0.02, respectively. The red, green, blue and yellow points refer to $z = 0.0, 0.5, 1.0$ and 1.5, respectively. The mean uncertainties of the data, in $\log_{10}$-space, are $0.17, 0.20$ and 0.21 dex for the upper, middle and bottom panel, respectively.

all the cases, the dispersion of the points increase with the N_{data}.

Figure 5.5 shows the same results of 5.4 but at fixed $f = 1.0$ and the upper, middle and bottom figures refer to $\sigma_{int} = 0.11, 0.05$ and 0.01, respectively. From the plots with $\sigma_{int} = 0.05$ and 0.01 we can see that the dispersion of the points for different redshift values is larger than in fig. 5.4. The dependence on the redshift is clearer. Moreover, the values of S cover a larger and smaller range than the values obtained in fig. 5.4, in the entire range of N_{data}. With $\sigma_{int} = 0.05$, the parameter
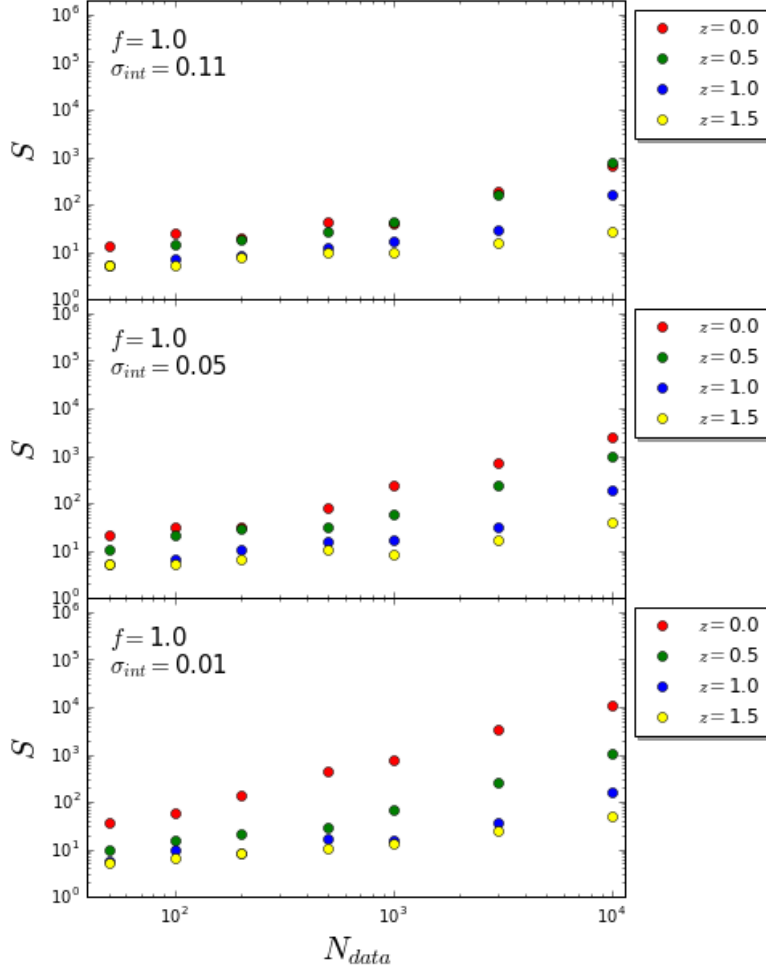
Figure 5.5:   As in 5.4 but at fixed $f = 1.0$ and the upper, middle and bottom figures refer to $\sigma_{int} = 0.11, 0.05$ and 0.01, respectively. The mean uncertainties of the data, in $\log_{10}$-space, are $0.17, 0.17$ and 0.19 dex for the upper, middle and bottom panel, respectively.

S increases from ≈ 30 at $z = 1.5$ to $\approx 2 \times 10^3$ at $z = 0.0$. With $\sigma_{int} = 0.01$, the parameter increases from ≈ 50 at $z = 1.5$ to $\approx 10^4$ at $z = 0.0$.

Finally, we have fitted our results of S, in the $\log_{10}$-space, with respect to one of the three parameters (N_{data}, f, and σ_{int}), at fixed redshift. In table 5.2 are shown the results for the $\log_{10} S - \log_{10} N_{data}$ relation, at fixed f and σ_{int}; in table 5.3 the $\log_{10} S - \log_{10} f$ relation at fixed σ_{int} and N_{data}; in table 5.4 the $\log_{10} S - \log_{10} \sigma_{int}$ relation at fixed N_{data} and f. From the results in table 5.2 we can see that the slope of the relation is steep with lower values of σ_{int} and f and it is steeper at $z = 0$ than at $z = 1$, as just showed in figure 5.2 and 5.3. Comparing the tables 5.3

$\log_{10} S = a \log_{10} N_{data} + b$				
σ_{int}	f	z	a	b
0.11	1.0	0.0	0.70 ± 0.10	-0.19 ± 0.29
0.01	0.2	0.0	1.24 ± 0.09	0.26 ± 0.26
0.11	1.0	1.0	0.59 ± 0.09	-0.41 ± 0.25
0.01	0.2	1.0	1.07 ± 0.06	-0.65 ± 0.18

Table 5.2: Linear fit between S and N_{data}, at fixed values of σ_{int}, f, and z, in $\log_{10}$-space.

$\log_{10} S = a \log_{10} f + b$				
σ_{int}	N_{data}	z	a	b
0.11	50	0.0	-0.02 ± 0.17	1.08 ± 0.07
0.01	10^4	0.0	-2.11 ± 0.06	4.01 ± 0.03
0.11	50	1.0	-0.49 ± 0.13	0.76 ± 0.05
0.01	10^4	1.0	-2.22 ± 1.16	1.91 ± 0.52

Table 5.3: Linear fit between S and f, at fixed values of σ_{int}, N_{data}, and z, in $\log_{10}$-space.

$\log_{10} S = a \log_{10} \sigma_{int} + b$				
f	N_{data}	z	a	b
1.0	50	0.0	-0.42 ± 0.07	0.74 ± 0.11
0.2	10^4	0.0	-2.67 ± 0.14	0.12 ± 0.21
1.0	50	1.0	-0.03 ± 0.03	0.69 ± 0.05
0.2	10^4	1.0	-1.24 ± 1.06	1.40 ± 1.57

Table 5.4: Linear fit between S and σ_{int}, at fixed values of f, N_{data}, and z, in $\log_{10}$-space.

and 5.4 we can see that the dependence on σ_{int} is larger than f at $z = 0$, and for a sample with few objects and large relative errors, both for a sample with many objects and small relative errors. On the other hand, at $z = 1$, the dependence on

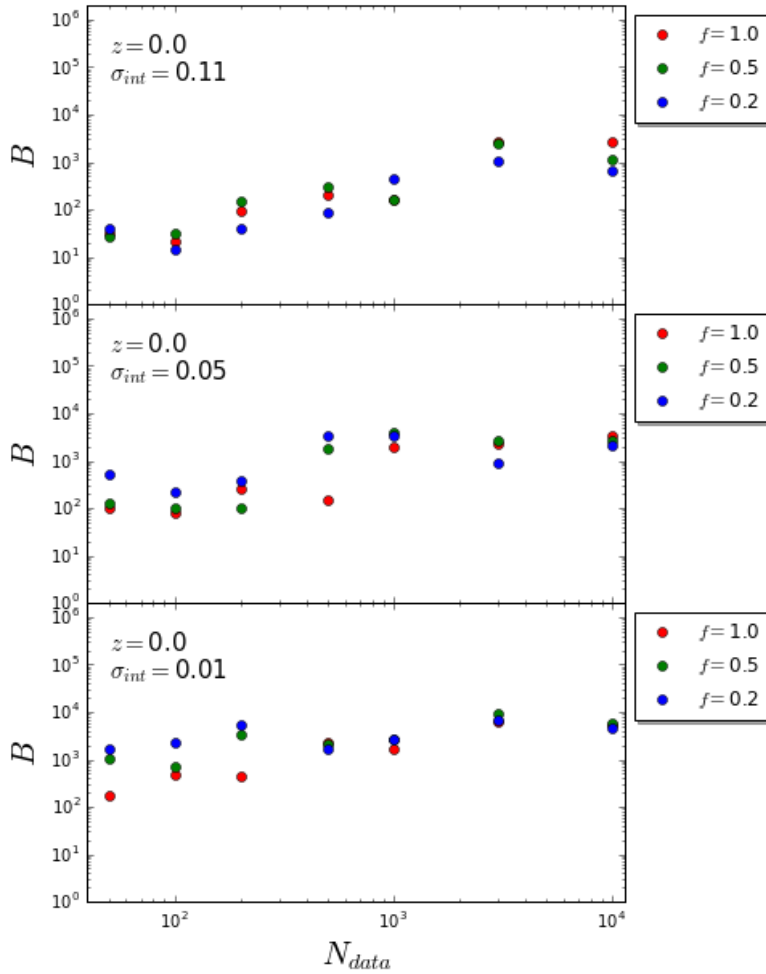Figure 5.6: The dependence of the median values of B on N_{data} and f, at fixed σ_{int} and at fixed redshift $z = 0$. The upper, middle and bottom panel refer to $\sigma_{int} = 0.11, 0.05$ and 0.01, respectively. The green, red and blue points refer to $f = 1.0, 0.05$ and 0.2, respectively. The mean uncertainties of the data, in $\log_{10}$-space, are $0.73, 0.76$ and 0.55 dex for the upper, middle and bottom panel, respectively.

parameter f is larger than σ_{int}.

5.2.2 The systematic bias B

Figure 5.6 shows the evolution of the median values of the bias B with N_{data} and f, at redshift $z = 0$ and at fixed σ_{int}. The upper, middle and bottom panels refer to the different values of σ_{int}, that are $\sigma_{int} = 0.11, 0.05$ and 0.01, respectively. The
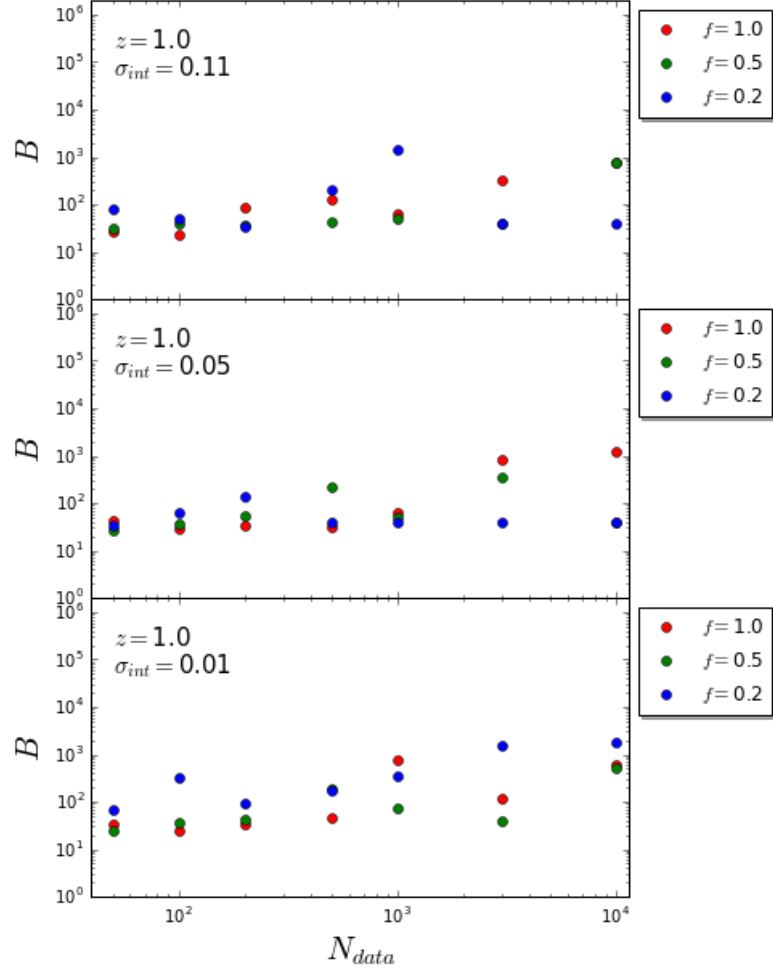
Figure 5.7: As in fig. 5.6 but for $z = 1.0$. The mean uncertainties of the data, in $\log_{10}$-space, are $0.62, 0.68$ and 0.67 dex for the upper, middle and bottom panel, respectively.

green, red and blue points refer to $f = 1.0$, 0.5 and 0.2, respectively. From the plot with $\sigma_{int} = 0.11$, we can see that the parameter tends to increase up reaching a maximum value, at $N_{data} = 3 \times 10^3$, and after it remains apparently constant. For $\sigma_{int} = 0.05$ the maximum is reached before than with $\sigma_{int} = 0.11$, i.e. the maximum is reached for $N_{data} = 5 \times 10^2 \div 10^3$. For $\sigma_{int} = 0.01$, this effect is more highlighted, the parameter B appears independent on N_{data}. Moreover, there is not a clear difference among the values of B for different f.

Figure 5.7 shows the same results of 5.6 but for $z = 1.0$. Also in this case B appears to be independent of N_{data} for all values of σ_{int}. Moreover, the dependence on f is not clear. The difference between the results of B at $z = 0$ and $z = 1$
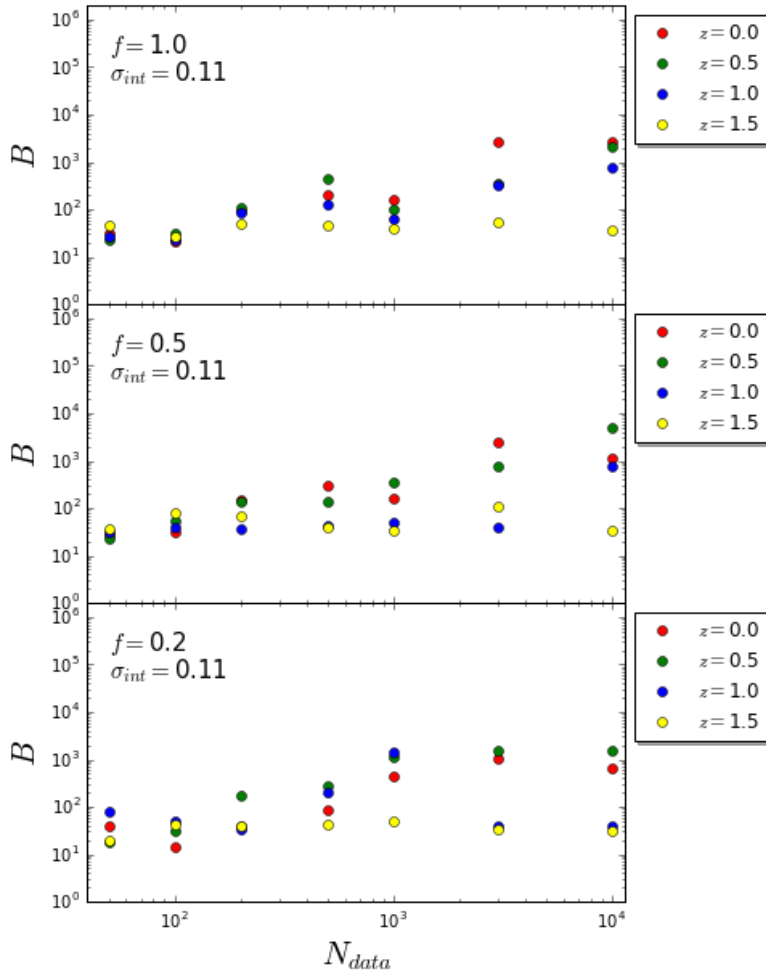
Figure 5.8: As in fig. 5.4 but for the parameter B. The mean uncertainties of the data, in $\log_{10}$-space, are $0.64, 0.64$ and 0.58 dex for the upper, middle and bottom panel, respectively.

is that the mean value of the maximum. The mean results at $z = 1$ have lower values than the $z = 0$ case.

Figure 5.8 shows the evolution of the median values of B with N_{data} and z, at fixed f and at fixed $\sigma_{int} = 0.11$. The upper, middle and bottom panels refer to $f = 1.0, 0.5$ and 0.2, respectively, while the red, green, blue and yellow points refer to $z = 0.0, 0.5, 1.0$ and 1.5, respectively. The behaviour of B is very similar in the three panels. At low redshift, the parameter B increases with N_{data} until a maximum, and it remains apparently constant thereafter. At high redshift, the bias appears independent on N_{data}. Moreover, there are not significant differences for the thee values of f.
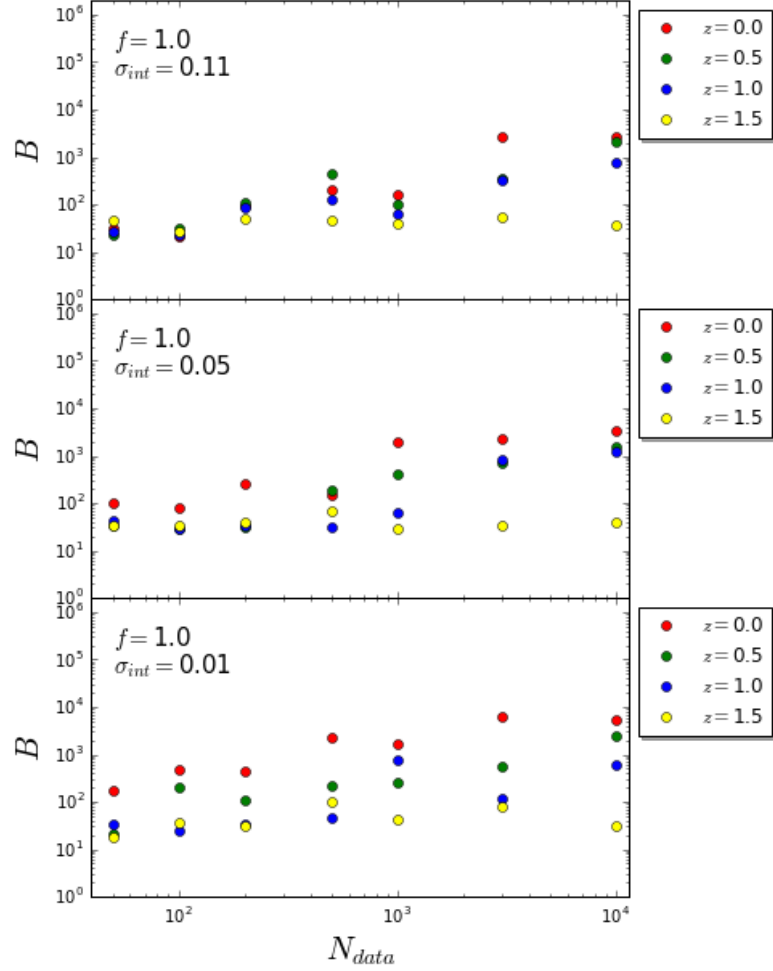
Figure 5.9:   As in fig. 5.8 but for $f = 1.0$; the upper, middle and bottom panels refer to $\sigma_{int} = 0.11, 0.05$ and 0.01, respectively. The mean uncertainties of the data, in $\log_{10}$-space, are $0.64, 0.66$ and 0.66 dex for the upper, middle and bottom panel, respectively.

Figure 5.9 shows the same results of 5.8 but at fixed $f = 1.0$ and the upper, middle and bottom figures refer to $\sigma_{int} = 0.11, 0.05$ and 0.01, respectively. In this case, at low redshifts and at low N_{data}, the parameter B increases for decreasing σ_{int}, by about a order of magnitude. Moreover, the parameter B increases with N_{data} reaching a maximum, after which it becomes constant. For larger values of N_{data}, the growth of B with the decreasing of σ_{int} is much weaker. At higher redshifts, the parameter B is apparently independent on the N_{data} and on σ_{int}.
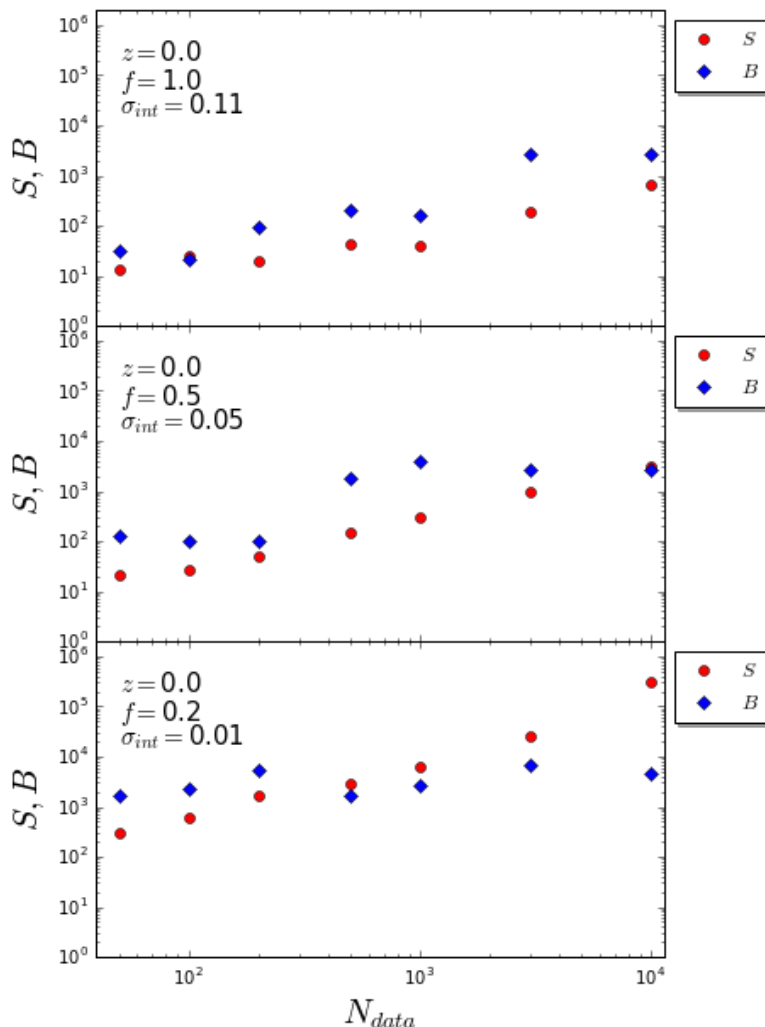
Figure 5.10: The dependence of the median values of S and B on N_{data} at redshift $z = 0$. The upper panel refers to $f = 1.0$ and $\sigma_{int} = 0.11$; $f = 0.5$ and $\sigma_{int} = 0.05$ for the middle panel; $f = 0.2$ and $\sigma_{int} = 0.01$ for the bottom panel.

5.3 Comparison between S and B

Figures 5.10 and 5.11 show the evolution of the median values of S and B of N_{data}. The figure 5.10 is for redshift $z = 0$, while the figure 5.11 is for redshift 1. For each figure, the upper panel shows the results for $f = 1.0$ and $\sigma_{int} = 0.11$, the middle panel for $f = 0.5$ and $\sigma_{int} = 0.05$ and the bottom panel for $f = 0.2$ and $\sigma_{int} = 0.01$. From the top panel of fig. 5.10, we can see that the accuracy B is always larger the precision S. Even at $N_{data} = 10^4$, B exceeds S, however, given the large
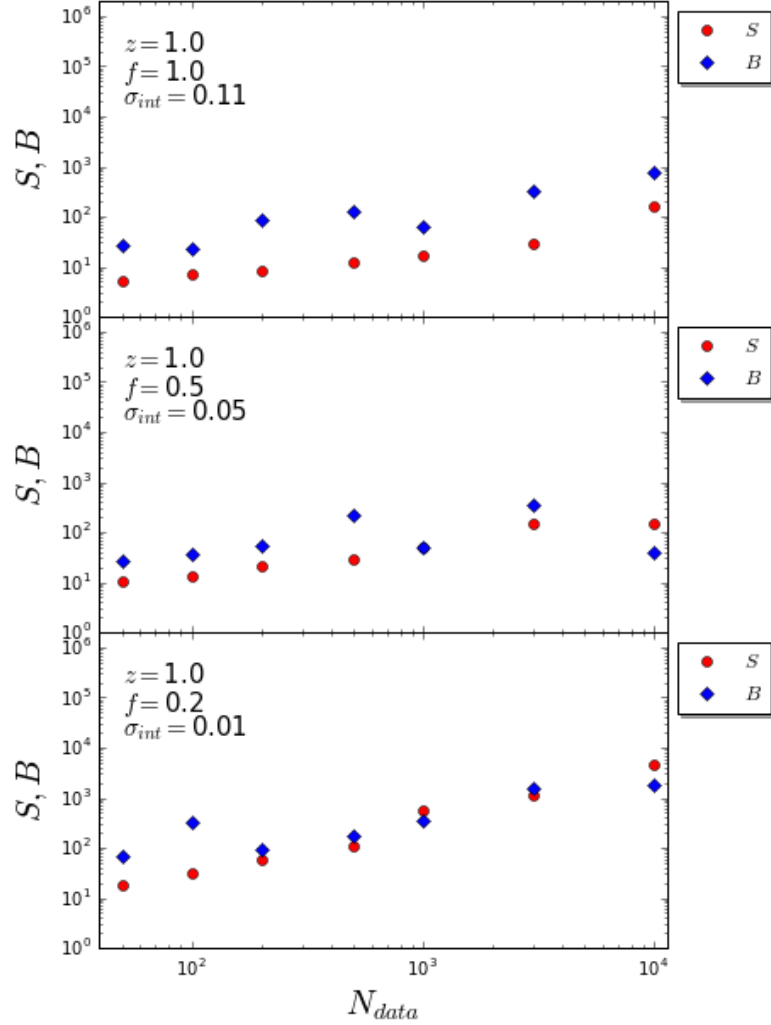
Figure 5.11: As in figure 5.10, but for redshift $z = 1$.

number of observed clusters, both B and S are very large. In the middle panel, we can see that the parameter S slightly exceeds B for $N_{data} = 10^4$. Therefore, to constrain the best cosmological parameters we need to observe $N_{data} = 3 \times 10^3$ clusters. From the bottom panel, we can see that S exceeds B between $N_{data} = 200$ and 500. The number of galaxy clusters to be observed, to reliably constrain the cosmological parameters, decrease with decreasing of f and σ_{int}. Moreover, the maximum accessible precision at $z = 0$, limited by B, is $S \simeq 2 \times 10^3$, with $f = 0.2$ and $\sigma_{int} = 0.01$. If we assume an equal absolute uncertain δ for Ω_M and σ_8, i.e. $\delta = \delta_{\Omega_M} = \delta_{\sigma_8}$ and $S = 1/\delta^2$, this uncertainty appears to be $\delta \approx 0.02$. Assuming the cosmological parameters obtained from Planck15, the relative uncertainties are

6.5% for Ω_M and 2.5% for σ_8.

From the top panel in figure 5.11, the accuracy is always over the precision, as for the first panel in 5.10. Therefore, to find the best cosmological parameters it is necessary observe 10^4 objects. From the middle panel, the parameter S exceeds B in the range $N_{data} \sim 10^3 \div 3 \times 10^3$. Therefore, it is useless to observe a number of clusters larger than these values to constrain the cosmological parameters. From the bottom panel, S exceeds B between $N_{data} \sim 200 \div 500$. In this case, the maximum achievable precision is $S \sim 100$. If we assume an equal absolute uncertain δ for Ω_M and σ_8, this uncertainty appears to be $\delta = \delta_{\Omega_M} = \delta_{\sigma_8} \approx 0.1$. Assuming the cosmological parameters obtained from Planck15, the relative uncertainties are 31% for Ω_M and 12% for σ_8.

Overall, we conclude that to constrain the cosmological parameters at high accuracy (i.e. values of $B > 100$) and high precision ($S > 100$) we require values of f and σ_{int} lower than the present estimates of 1 and 0.11, respectively, and a number of objects in the order of $\sim 10^3$.

5.4 Future surveys of galaxy clusters

We have analyzed some of the planned surveys of galaxy clusters to understand which missions will be able to constrain the cosmological parameters Ω_M and σ_8 using the c-M relation. We have mainly focused on the number of galaxy clusters that the future surveys will observe.

One of the main future missions will be the European Space Agency (ESA) Cosmic Vision mission *Euclid*. Its launch is planned for 2020. Euclid will observe in the visible and near-infrared wavelength range, from 550nm to 2000nm, see Laureijs et al. [2011]. Euclid will study the evolution of the cosmic web up to redshift $z \sim 2$ through the study of the cosmological weak lensing and the galaxy clustering. The detection of the galaxy clusters will be possible in three different ways, using photometric and spectroscopic data and using the gravitational lensing. Sartoris et al. [2016] studied the characteristics of the galaxy cluster samples observable by the Euclid mission; they predicted the number of the expected observed clusters. They defined the ratio N_{500}/σ_{field} as the threshold value that a cluster has to pass to be detected, where N_{500} indicates the number of cluster galaxies contained within a sphere of radius r_{500}, and σ_{field} is the root mean square of the field galaxy counts, i.e. the contamination by field galaxies in the cluster area. Using the detection threshold $N_{500}/\sigma_{field} > 5$, they found that Euclid will detect $\sim 2 \times 10^5$ objects in the redshift range $0.2 \div 2.0$, with about $\sim 4 \times 10^4$ of them at $z \geq 1.0$. By lowering the detection threshold down to $N_{500}/\sigma_{field} > 3$, they found that the number of the cluster that will be detected rises up to $\sim 2 \times 10^6$, with $\sim 4 \times 10^5$ of them at $z \geq 1.0$. To obtain the mass profiles, necessary to

measure the concentration, the Euclid observations will not be enough. The mass profiles will be available stacking the clusters for given mass bin. For this reason, the number of the "observed" clusters decreases by about one or two orders of the magnitude dependent on the mass bin and redshift.

Another important space mission will be the X-ray $eROSITA$ telescope (extended ROentgen Survey with an Imaging Telescope Array). Its launch is planned for 2017. eROSITA will observe in the soft band $[0.5-2]$keV and in the hard band $[2-10]$keV through 7 modules with 54 shells per module, Merloni et al. [2012]. The main goal of eROSITA is the study of the large scale structure in the Universe, to test and characterize the cosmological model. It will be able to discover massive galaxy clusters to probe the statistics of the very large scale matter density distribution. It is expected that eROSITA will be able to detect more than 10^5 galaxy clusters, in the soft band, more massive than $5 \times 10^{13} \mathrm{h}^{-1} \mathrm{M}_\odot$ and with a median redshift $z \simeq 0.35$, see Pillepich et al. [2012]. Also in this case, the concentration parameter will be not achieved with eROSITA observations only. This mission will measure only a single value of temperature for each cluster, and it is expected that the temperature measurements will be with high precision, $\Delta T/T \lesssim 10\%$ for $\simeq 1600$ new galaxy clusters (Borm et al. [2014]). Without a temperature profile, it will be impossible to use the hydrostatic equilibrium accurately recover the mass profile and get the concentration, as it has been done for the A16 and E10 samples. To obtain the concentration measurements, a stack of several observations in the X-ray band and lensing measure will be necessary.

Another important cluster survey will be obtained by the ground-based telescope $LSST$ (Large Synoptic Survey Telescope). LSST is designed to image a substantial fraction of the sky in optical bands, covering the wavelength range $320 \div 1050$nm, see LSST Dark Energy Science Collaboration [2012]. The telescope will be operative from 2021. Its science goals are the study of the nature of dark energy and dark matter, how the Milky Way formed, the nature of the outer regions of the Solar system and much more. LSST will analyze the weak and strong gravitational lensing effect, the large-scale structures, the type Ia Supernovae and the galaxy clusters. On the latter item, it is expected that the LSST telescope will be able to discover over 3×10^5 galaxy clusters over a redshift range $0.1-1$. To obtain the concentration measurements, a stack of the observations of LSST will be necessary, as for the Euclid mission.

We can make very rough estimates of S and B expected for these survey. We can roughly estimate that $Euclid$ will provide measurements of concentration for $\sim 2 \times 10^3$ clusters using the stacked signal for a detection threshold $N_{500}/\sigma_{field} > 5$. If we fix the median redshift of the observations at $z = 1$, and if we assume that $f = 0.2$, due to the high precision measurements expected, and a homogeneous sample with $\sigma_{int} = 0.01$, S and B will be $\simeq 100$. Moreover, with a high precision

measurements and a homogeneous sample, it will be not necessary to use the entire sample to determine the cosmological parameters with higher precision and accuracy, but a sub-sample of 500 objects will be enough, because we want to make our estimates under the condition that we are only limited from the systematic errors, not from the statistical ones (i.e. $S \lesssim B$). eROSITA will measure the concentration for $\sim 10^3$ different clusters, stacking observations in the X-ray band. The median redshift of the observations will be $z \sim 0.3$. If we assume that $f = 0.2$ and for a well behaved sub-sample with low intrinsic scatter $\sigma_{int} = 0.01$, S and B will be $\simeq 600 \div 800$ and $\simeq 900$ respectively, using only a sub-sample of 500 clusters. LSST will provide a values of the concentration for 3×10^3 stacked clusters. The median redshift of the observations will be $z \sim 0.5$. If $f = 0.02$ and $\sigma_{int} = 0.01$, S and B will be $\simeq 100 \div 200$ and $\simeq 400$ respectively.

All these surveys will provide global mass proxies. To measure the mass profile and the concentration of single clusters, it will be necessary to make dedicated, and intensive, follow-ups in the X-ray and optical/IR bands that will be possible only on a selected sub-sample of few hundreds (up to about a thousand) of objects. Alternatively, stacking of the lensing signal associated to the detected massive halos will permit to estimate a mean concentration in a few predefined mass bins. Furthermore, the stacking procedure will provide the mean c-M relation, whose intrinsic scatter decreases roughly as $1/N_{binned}^{0.5}$, where N_{binned} is the number of binned clusters.

6
Conclusions

In this Thesis, we have studied the efficiency of the c-M relation of galaxy clusters in constraining the cosmological parameters Ω_M and σ_8. For this reason, we have developed a Python code that it is able to simulate a mock data set and analyzed real or simulated samples. In the following, we summarize the results that we have obtained.

- We have verified that our code, which exploits the public `Colossus` libraries, implements correctly the c-M relations expected for the main models proposed in literature, as a function of mass, redshift, and cosmological parameters, section 3.4.1.

- We have run several tests to understand the efficiency of our code, section 3.4.2. We have created mock data using the Planck15 cosmological model. We considered four c-M relation, that are Bullock et al. [2001] in the improved version of Macció et al. [2008], Prada et al. [2012], Bhattacharya et al. [2013], and Diemer & Kravtsov [2015]. Subsequently, we have fitted the mock data with the same c-M relation used to create the sample. We have found that the results obtained are in agreement with the input cosmological parameters. We estimated how the redshift dependent uncertainties on mass and concentration affect the constraints on the cosmological parameters.

- We assessed the impact of a proper modelling of the c-M relation. We have fitted the sample created with the D15 concentration model with the other three models to understand the impact of the c-M modelling, section 3.4.3. We have found the best-fit cosmological parameters obtained with the B01, P12, and B13 concentration models are very different from the input parameters. But we have found that the c-M relations built up with these best-fit cosmological parameters are very close to the relation expected for the D15

model, expect for the P12 model. The P12 model predicts a c-M relation always above the other three model, due to known shortcomings (Meneghetti & Rasia [2013]) and we discarded it in the following.

- We have run our code to find the best fit cosmological parameters using the high-redshift *Chandra* data sample of Amodeo et al. [2016], section 4.3. We have obtained $\Omega_M = 0.25^{+0.28}_{-0.15}$ e $\sigma_8 = 1.24^{+0.08}_{-0.42}$ using the B01 model, $\Omega_M = 0.14^{+0.14}_{-0.04}$ e $\sigma_8 = 1.16^{+0.34}_{-0.02}$ with the B13 model, and finally $\Omega_M = 0.10^{+0.30}_{-0.00}$ e $\sigma_8 = 1.46^{+0.04}_{-0.59}$ with the D15 model. Moreover, we also considered the low-redshift *XMM-Newton* data sample of Ettori et al.[2010], section 4.4. From the joint analysis of the two samples, we have obtained $\Omega_M = 0.42^{+0.11}_{-0.19}$ e $\sigma_8 = 0.86^{+0.12}_{-0.19}$ using the B01 model, $\Omega_M = 0.32^{+0.58}_{-0.22}$ e $\sigma_8 = 0.91^{+0.08}_{-0.12}$ with the B13 model, and finally $\Omega_M = 0.13^{+0.12}_{-0.03}$ e $\sigma_8 = 1.31^{+0.06}_{-0.19}$ with the D15 model. We have verified that our results are in agreement with previous works and the current standard cosmological model, section 4.6.

- We have studied how the precision (S) and the accuracy (B) of the cosmological parameters obtained with the c-M relation change for different observational settings. We have defined the precision and the accuracy as $1/(\delta_{\Omega_M} * \delta_{\sigma_8})$ and $1/(\Delta_{\Omega_M} * \Delta_{\sigma_8})$, respectively, where δ_{Ω_M} and δ_{σ_8} indicate the statistical uncertainty of the cosmological parameters, while Δ_{Ω_M} and Δ_{σ_8} indicate the difference between the best-fit cosmological parameters and the cosmological parameters of the input cosmology. We have studied how S and B depend on the number of the objects observed, N_{data}, the intrinsic scatter of the c-M relation, σ_{int}, the relative statistical uncertainty on mass and concentration measurements f, in units of the uncertainties affecting present day samples ε_M and ε_c, and the redshift, z, chapter 5. We have used only the D15 concentration model to create and analyze the mock data. Furthermore, we have adopted the Planck15 cosmological model. As expected, we have found that the constraints on the cosmological parameters improve in precision with N_{data}. The precision is optimized when we consider the sample with lower values of σ_{int}, f, and z. At lower values of z, the effect of f is very weak for larger values of σ_{int}; its effect becomes significant at lower values of σ_{int}. At high z, the role of f is significant for each value of σ_{int}.

- The accuracy improves very weakly with N_{data}, until it finds a maximum value, after which it becomes constant. At $z = 0$ and $\sigma_{int} = 0.11$ the accuracy becomes constant after $N_{data} = 3 \times 10^3$; with $\sigma_{int} = 0.05$, it becomes constant in the range $N_{data} = 5 \times 10^2 \div 10^3$; with $\sigma_{int} = 0.01$ it seems to be independent of N_{data}. For higher values of z, the accuracy is independent of N_{data} for each value of σ_{int} and f. The mean values of the accuracy are larger at low redshift than at high redshift. Moreover, for lower values of

N_{data} and z, the accuracy grows with the decreasing of σ_{int}, and there is not a clear effect of the parameter f.

- Finally, we have compared the expected accuracy and precision under different observational settings to find the optimal conditions to constraint the cosmological parameters. The precision must not exceed the accuracy because, otherwise, one is measuring biased cosmological parameters. We have found that the accuracy is always above the precision when we consider large values of σ_{int} and f, both for $z = 0$ and $z = 1$. The precision exceeds the accuracy when we consider lower values of σ_{int} and f. At $z = 0$, we have found that the maximum precisions obtainable are 6.5% for Ω_M and 2.5% for σ_8, assuming an absolute uncertainties for the cosmological parameters. At $z = 1$. the maximum precisions are 31% for Ω_M and 12% for σ_8.

Our work can be improved to obtain more robust results and, in the following, we report some ways to do that.

- The simulation scheme can be improved by adding a dispersion around the relative errors ($\varepsilon_c(z)$ and $\varepsilon_M(z)$) and considering a redshift distribution of the investigated galaxy cluster population that follows e.g. the halo mass function convolved with some simple selection functions.

- We could add more external constraints on the physical properties of the galaxy clusters to break further the degeneracy between the investigated cosmological parameters and to improve the fitting procedures, section 3.3. E.g., one can consider the information about the gas mass fraction, f_{gas}. Ettori et al. [2010] demonstrated that using the information about f_{gas}, which depends only on Ω_M and does not depend on σ_8,can break the degeneracy.

- Forecasting can be improved by running the code with a larger number of the objects observed, up to 10^6. Instead of applying the parameter f on the ε_c and ε_M simultaneously, one can study the results about the accuracy and precision applying f separately.

- We could add some extra cosmological parameters like the relative amount of dark energy, by relaxing the assumption of a flat Universe, and characterizing its equation of state $p = w\rho c^2$ with $w = w_0 + w_a z/(1 + z)$, where w_0 is the present value of the dark energy equation of state parameter and w_a is the rate at which this parameter change as function of the redshift z.

Bibliography

Amodeo S., Ettori S., Capasso R., Sereno M., 2016, AAP, 590, A126

Bhattacharya S., Habib S., Heitmann K., & Vikhlinin A., 2013, ApJ, 766, 32

Borm K., Reiprich T. H., Mohammed I. & Lovisari L., 2014, AAP, 567, A65

Bryan G. L., Norman M. L., 1998, ApJ, 495, 80

Bullock J. S., Kolatt T. S., Sigad Y., et al.. 2001, MNRAS, 321, 559

Buote D. A., Gastaldello F., Humphrey P. J., et al., 2007, ApJ, 664, 123

Diemer B., 2015, Astrophysics Source Code Library, ascl:1501.016

Diemer B., & Kravtsov A. V., 2015, ApJ, 799, 108

Duffy A. R., Schaye J., Kay S. T., Dalla Vecchia C., 2008, MNRAS, 390, L64

Ettori S., Gastaldello F., Leccardi A. et al., 2010, AAP, 524, A68

Ettori S., Morandi A., Tozzi P. et al., 2009, AAP, 501, 61

Giocoli C., Tormen G., & Sheth R. K., 2012, MNRAS, 422, 185

Gunn, J. E., & Gott, J. R., III 1972, ApJ, 176, 1

Hinshaw G., Weiland J. L., Hill R. S., et al., 2009, ApJ, 180, 225

Jeans, J. H. 1902, Philosophical Transactions of the Royal Society of London
    Series A, 199, 1

Jing Y. P., 2000, ApJ, 535, 30

Klypin A., Trujillo-Gomez S., Primack J., 2011, ApJ, 740, 102

Laureijs R., Amiaux J., Arduini S., et al., 2011, arXiv:1110.3193

LSST Dark Energy Science Collaboration 2012, arXiv:1211.0310

Macciò A. V., Dutton A. A., & Van Den Bosch F. C., 2008, MNRAS, 391, 1940

Mantz A. B., Allen S. W., Morris R. G., et al., 2014, MNRAS, 440, 2077

Mantz A. B., von der Linden A., Allen S. W., et al., 2015, MNRAS, 446, 2205

Meneghetti M. & Rasia E., 2013, arXiv:1303.6158

Merloni A., Predehl P., Becker W., et al, 2012, arXiv:1209.3114

Muñoz-Cuartas J. C., Macciò A. V., Gottlöber S., & Dutton, A. A., 2011, MNRAS, 411, 584

Navarro J. F., Frenk C. S., & White S. D. M., 1997, ApJ, 490, 493

Neto A F., Gao L., Bett P., et al., 2007, MNRAS, 381, 1450

Pillepich A., Porciani C., & Reiprich T. H., 2012, MNRAS, 422, 44

Planck Collaboration, Ade, P. A. R., Aghanim, N., et al., 2016, AAP, 594, A13

Prada F., Klypin A. A., Cuesta A. J., Betancort-Rijo J. E., & Primack J., 2012, MNRAS, 423, 3018

Press, W. H., & Schechter, P. 1974, ApJ, 187, 425

Sartoris B., Biviano A., Fedeli C., et al., 2016, MNRAS, 459, 1764

Sereno M. & Ettori S., 2015, MNRAS, 450, 3675

Sereno M. & Ettori S., 2015, MNRAS, 450, 3633

Vikhlinin A., Kravtsov A., Forman W. et al., 2006, ApJ, 640, 691

Zhao D. H., Jing, Y. P., Mo H. J., Bnörner G., 2009, ApJ, 707, 354

Vikhlinin A., Kravtsov A. V., Burenin R. A., et al., 2009, ApJ, 692, 1060

Weiner B. J., Willmer C. N. A., Faber S. M. et al., 2006, ApJ, 653, 1049

A
Developed Code

A.1 create_range

```python
def create_range(a, b, c):
    array = np.array([a])
    k = 0
    while (k < b):
        k = array[-1]+c
        array = np.append(array,[k])

    return array
```

A.2 mass_range_gauss

```python
def mass_range_gauss(Log_M_min, Log_M_max, dev, number):
    mean = (Log_M_max + Log_M_min)/2
    sigma = (Log_M_max - Log_M_min)*dev

    return np.random.normal(mean,sigma,number)
```

A.3 generate_obs

```python
def generate_obs(file_name, Mass200c, redshift, cosmo, model):
    f = open( file_name , 'w')
    cosmo = cosmology.setCosmology(cosmo)
    line = '# Mass, concencentration and redshift with cosmology  '+
    cosmology.getCurrent().name + ' and c-M model '+model  +'\n'
    f.write(line)
    line = '#'+"Omega_m = %.2f, Omega_L = %.2f, Omega_b = %.2f, H_0 =
    %2.f, sigma_8 = %.2f, ns = %.2f" % (cosmo.Om0, cosmo.OL0, cosmo.
    Ob0, cosmo.H0, cosmo.sigma8, cosmo.ns) + '\n'
```

```
7       f.write(line)
8       line = '#'+'Mass200c   Mass200c_err   redshift   c200c_obs
    c200c_obs_err'+'\n'
9       f.write(line)
10      print 'Cosmology input: ' + 'Omega_m = %.2f,sigma_8 = %.2f ' % (
    cosmo.Om0,   cosmo.sigma8)
11
12      Mass200c_error = Mass200c * par.epsilon_m
13      log_c_model = np.log10(concentration.concentration(Mass200c*(10**
    14), '200c', par.z_obs, model = model, statistic = 'mean'))
14      log_c_real =  np.random.normal(log_c_model, par.sigma_int , len(
    log_c_model) )
15      log_c_obs =   np.random.normal(log_c_real, par.epsilon_c /math.
    log(10) ,len(log_c_model) )
16
17      c_obs = 10**(log_c_obs)
18      for i in range(len(Mass200c)):
19          if (c_obs[i] < 1.00):
20              c_obs[i] = 1.00
21      c_error = c_obs * par.epsilon_c
22
23      for i in range(len(Mass200c)):
24          line = ' %5.3f , %20.3f , %20.3f , %20.4f , %15.4f' % (
    Mass200c[i],Mass200c_error[i],redshift[i],c_obs[i],c_error[i]) + '
    \n'
25          f.write(line)
26      f.close()
27      del Mass200c, redshift, c_misurato, c_error, i
28      del line
29
30      return 0
```

A.4 modelling_data

```
1  def modelling_data( Sigma_8,Omega_M, Mass_obs,redshift_obs , model_out
    , correction):
2
3      c_model      = np.zeros( ( len(Mass_obs), len(Sigma_8), len(
    Omega_M) ) )
4      c_model_err = np.zeros( ( len(Mass_obs), len(Sigma_8), len(
    Omega_M) ) )
5
6      for i in range(len(Mass_obs)):
7          for j in range(len(Sigma_8)):
8              for k in range(len(Omega_M)):
9
10                 if correction:
11                     Mass_obs_new = correction_mass(Mass_obs[i],
```

```
                redshift_obs[i], 0.3,1.0, Omega_M[k],Sigma_8[j])
12             else:
13                  Mass_obs_new = Mass_obs[i]
14                  my_cosmo = {'flat': True, 'H0': 70.0, 'Om0':
    Omega_M[k], 'Ob0': 0.050, 'sigma8': Sigma_8[j], 'ns': 1}
15                  cosmology.setCosmology('my_cosmo', my_cosmo)
16
17             c_model[i,j,k] = concentration.concentration(
    Mass_obs_new*(10**14), '200c', redshift_obs[i], model = model_out,
     statistic = 'mean')
18             c_model_err[i,j,k]=c_model[i,j,k]*(par.sigma_int*math
    .log(10))
19
20          del Mass_obs_new,
21     del i,j,k, flat,Hubble_costant, spectral_index,  Omega_barionico
22
23     return c_model, c_model_err
```

A.5   correction_data

```
1 def correction_data( Sigma_8,Omega_M, Mass_obs,redshift_obs ,
    model_out, c_model, c_model_err, correction):
2
3    if correction:
4        Mass_obs_new = correction_mass(Mass_obs, redshift_obs,
    0.3,1.0, Omega_M,Sigma_8)
5    else:
6        Mass_obs_new = Mass_obs
7        my_cosmo = {'flat': True, 'H0': 70.0, 'Om0': Omega_M, 'Ob0':
    0.050, 'sigma8': Sigma_8, 'ns': 1}
8        cosmology.setCosmology('my_cosmo', my_cosmo)
9
10   m0 = Mass_obs_new*10**14
11   c_prova = c_model
12
13   while (c_prova == -1):
14       m0 = m0 * 0.95
15       c_prova = concentration.concentration( m0, '200c',
    redshift_obs, model = model_out, statistic = 'mean')
16
17   m1 = m0 / 2.0
18
19   mass_interpolated =  np.linspace(m1, m0 , 10)
20   c_interpolated = np.zeros( len(mass_interpolated)  )
21
22   for w in range(len(mass_interpolated)):
23       c_interpolated[w] = concentration.concentration(
    mass_interpolated[w], '200c', redshift_obs, model = model_out,
```

```
24
25    m = np.log10(mass_interpolated)
26    c = np.log10(c_interpolated)
27
28    def line(x,a,b):
29        return a*x+b
30
31    popt, pcov = curve_fit(line, m, c)
32
33    c_model = 10**( line( math.log10(Mass_obs_new*10**14) , popt[0]
      , popt[1] ) )
34    c_model_err = c_model*(0.11*math.log(10))
35
36    del line,popt,pcov, Mass_obs_new, m0,m1,c_prova,m,c,
      c_interpolated,mass_interpolated,w
37
38    return c_model, c_model_err
```

A.6   chi_square

```
1  def chi_square(model_out, Sigma_8,Omega_M,Mass_obs, Mass_obs_err,
      redshift_obs,c_obs,c_obs_err, c_model,c_model_err, correction):
2
3      chi_model = np.zeros((len(Sigma_8),len(Omega_M)))
4
5      for i in range(len(Sigma_8)):
6          for j in range(len(Omega_M)):
7              for k in range(len(Mass_obs)):
8
9                  if correction:
10                     Mass_obs_new = correction_mass(Mass_obs[k],
      redshift_obs[k], 0.3,1.0, Omega_M[j],Sigma_8[i])
11                 else:
12                     Mass_obs_new = Mass_obs[k]
13                 my_cosmo = {'flat': True, 'H0': 70.0, 'Om0':
      Omega_M[j], 'Ob0': 0.050, 'sigma8': Sigma_8[i], 'ns': 1}
14                 cosmology.setCosmology('my_cosmo', my_cosmo)
15
16                 Mass_obs_err_new = ( Mass_obs_err[k] / Mass_obs[k] )
      * Mass_obs_new
17
18                 m1 = Mass_obs_new-Mass_obs_err_new
19                 m2 = Mass_obs_new+Mass_obs_err_new
20                 c1 = concentration.concentration( m1*(10**14), '200c'
      , redshift_obs[k], model = model_out, statistic = 'mean')
21                 c2 = concentration.concentration( m2*(10**14), '200c'
      , redshift_obs[k], model = model_out, statistic = 'mean')
```

```
22
23                    c_temporaneo = 0.0
24
25                    if (c1 == -1):
26                         c1,c_temporaneo  = correction_data(Sigma_8[i],
      Omega_M[j], m1, redshift_obs[k], model_out, c1,c_temporaneo,
      correction)
27
28                    if (c2 == -1):
29                         c2,c_temporaneo = correction_data(Sigma_8[i],
      Omega_M[j], m2, redshift_obs[k], model_out, c2,c_temporaneo,
      correction)
30
31                    del c_temporaneo
32                    c1 = math.log10(c1)
33                    m1 = math.log10(m1*(10**14))
34                    c2 = math.log10(c2)
35                    m2 = math.log10(m2*(10**14))
36
37                    B = (c2-c1)/(m2-m1)
38
39                    sigma_k_quadro = ( c_obs_err[k]/(c_obs[k]*math.log
      (10)) )**2 + ( c_model_err[k,i,j]/(c_model[k,i,j]*math.log(10)) )*
      *2 + (B**2) * ( (Mass_obs_err[k]/(Mass_obs[k]*math.log(10)))**2 )
40                    chi_2_model += (( math.log10(c_obs[k]) - math.log10(
      c_model[k,i,j]) )**2)  / (  sigma_k_quadro )    + math.log(
      sigma_k_quadro)  + 2*math.log( math.sqrt( 2*math.pi    ) )
41                    del Mass_obs_new, Mass_obs_err_new, c1,m1,c2,m2
42
43            chi_model[i,j]=chi_2_model
44
45     del chi_2_model,i,j,k
46
47     return chi_model, chi_temporaneo
```

A.7 find_parameter_error

```
1 def find_parameter_error(Omega_M, Sigma_8, chi_model):
2
3     chi_one_sigma = chi_model.min() + 2.3
4
5     idx = np.where(chi_model < chi_one_sigma)
6
7     sigma_best = np.zeros(3)
8     omega_best = np.zeros(3)
9     x,y = np.unravel_index(np.argmin(chi_model),chi_model.shape)
10
11     omega_best[0] = Omega_M[y]
```

```
12      omega_best[1] = Omega_M[idx[1].max()] − Omega_M[y]
13      omega_best[2] = Omega_M[y] − Omega_M[idx[1].min()]
14
15      sigma_best[0] = Sigma_8[x]
16      sigma_best[1] = Sigma_8[idx[0].max()] − Sigma_8[x]
17      sigma_best[2] = Sigma_8[x] − Sigma_8[idx[0].min()]
18
19      return  omega_best, sigma_best
```

A.8   probability_density_function

```
1  def probability_density_function(sigma_8, omega_m, chi_quadro, method
       ):
2
3      chi_prob = np.zeros((len(sigma_8),len(omega_m)))
4      chi_quadro = chi_quadro − chi_quadro.min()
5      for i in range(len(sigma_8)):
6          for j in range(len(omega_m)):
7              chi_prob[i,j] = math.exp(−chi_quadro[i,j]/2.0)
8
9      prob_sigma = np.zeros(len(sigma_8))
10     prob_omega = np.zeros(len(omega_m))
11
12     somma = 0
13     for i in range(len(sigma_8)):
14         for j in range(len(omega_m)):
15             somma += chi_prob[i,j]
16         prob_sigma[i] = somma
17         somma = 0
18
19     somma = 0
20     for j in range(len(omega_m)):
21         for i in range(len(sigma_8)):
22             somma += chi_prob[i,j]
23         prob_omega[j] = somma
24         somma = 0
25
26     if (method == 'integrate'):
27         prob_sigma = prob_sigma / integrate.simps(prob_sigma,sigma_8)
28         prob_omega = prob_omega / integrate.simps(prob_omega, omega_m
       )
29     elif (method == 'max'):
30         prob_sigma = prob_sigma/prob_sigma.max()
31         prob_omega = prob_omega/prob_omega.max()
32
33     return prob_sigma, prob_omega
```

A.9   best_parameter_from_probability

```python
def best_parameter_from_probability(sigma_8, omega_m, prob_sigma,
    prob_omega):

    x = np.sum( np.multiply(sigma_8, prob_sigma) )
    y = np.sum(prob_sigma)
    sigma_mean = x / y
    z = (sigma_8 - sigma_mean)**2
    x = np.sum( np.multiply(z, prob_sigma) )
    sigma_std = np.sqrt( x / y )
    del x,y,z

    x = np.sum( np.multiply(omega_m, prob_omega) )
    y = np.sum(prob_omega)
    omega_mean = x / y
    z = (omega_m - omega_mean)**2
    x = np.sum( np.multiply(z, prob_omega) )
    omega_std = np.sqrt( x / y )
    del x,y,z

    sigma_best = np.array([sigma_mean, sigma_std])
    omega_best = np.array([omega_mean, omega_std])

    return omega_best,sigma_best
```